THESIS FOR THE DEGREE OF LICENTIATE OF ENGINEERING

Methods for the Evaluation of Wingsails with a Crescent-Shaped Profile

HENG ZHU

Department of Mechanics and Maritime Sciences
CHALMERS UNIVERSITY OF TECHNOLOGY
Gothenburg, Sweden, 2023

Methods for the Evaluation of Wingsails with a Crescent-Shaped Profile

HENG ZHU

Report No 2023:09

Chalmers University of Technology

Department of Mechanics and Maritime Sciences

Division of Marine Technology

SE-412 96, Gothenburg

Sweden

Telephone: + 46 (0)31-772 1000

Printed by Chalmers Reproservice

Gothenburg, Sweden, 2023

Methods for the Evaluation of Wingsails with a Crescent-Shaped Profile

HENG ZHU

Chalmers University of Technology

Department of Mechanics and Maritime Sciences

Division of Marine Technology

Abstract

Seaborne transportation accounts for a large proportion of greenhouse gas (GHG) emissions. The International Maritime Organization (IMO) has stipulated that GHG emissions should be reduced by 50% before 2050 compared to 2018. The use of wind-assisted ship propulsion (WASP) is considered one of the most effective ways to reduce GHG emissions. Therefore, the present study aims to establish multidisciplinary numerical models for predicting and evaluating the propulsive performance and structural response of WASP systems.

Conceptual designs of a set of telescopic wingsail rigs are generated. Numerical simulations, including computational fluid dynamics (CFD) simulations and finite element analysis, are performed for dimensioning and optimizing wingsail structures for ships to understand the fluid–structural interaction (FSI). Since the deformation of the wingsail structure that the surrounding flow excites is so large, the interaction between the flow and structure creates a coupled problem. Analysis of a crescent-shaped wingsail using an in-house software ShipCLEAN, which is based on a generic ship energy model, is conducted to evaluate this wingsail's propulsive performance in comparison with other WASP concepts.

It is concluded that wingsails with a sectional profile and significant camber have much better propulsive performance than those with conventional airfoil profiles because the potential thrust force coefficient is approximately 30% higher. It is also found that the external loads on the crescent-shaped wingsail show notable periodic oscillations due to strong flow separation, so it can be inferred that wingsails can suffer from remarkable vortex-induced vibration. This raises higher requirements on the strength and rigidity of the wingsail structure. Tip vortices are found to have negative impacts on thrust, and the sail can strongly influence the wake flow. It is also concluded from the structural analysis that the strength, especially the von Mises yield and compressive normal stress, is most critical among the assessment criteria that are considered when evaluating the wingsail structure. Using a strong frame to bear global bending and introducing a cubic-shaped mast prevents stress concentration and reduces the weight of the structures.

Keywords: crescent-shaped profile, light weight structure, rigid wingsail, wind-assisted ship propulsion.

Preface

I am deeply grateful for the support and contributions of so many individuals, institutions, and organizations that have helped me to complete this thesis over the past two years.

First and foremost, I want to express my sincere appreciation to my supervisors, Carl-Erik Janson, Hua-Dong Yao, Jonas W. Ringsberg, and Bengt Ramne, for their invaluable support and guidance throughout my licentiate journey. Their expertise, insights, and encouragement have been essential to my success, and I could not have completed this work without their contributions.

To Carl-Erik Janson, I want to express my appreciation for his extensive knowledge and expertise in the field of fluid dynamics. His insights and advice have been invaluable in shaping my research and helping me to develop a deep understanding of the fundamental principles of fluid mechanics

To Hua-Dong Yao, I would like to extend my gratitude for his comprehensive knowledge and proficiency in the realm of fluid dynamics. His guidance has helped me to tackle some of the more challenging aspects of my research. I am deeply appreciative of his unwavering patience and continuous encouragement throughout this intellectual journey, which has significantly contributed to my growth and success.

To Jonas W. Ringsberg, I want to express my appreciation for his guidance and support throughout the development of my PhD study, his remarkable proficiency and vast knowledge in the field of structural engineering, and his management as my line manager. His insights and feedback have been instrumental in helping me to establish the structural analysis. I have learned so much from his expertise and am grateful for his willingness to share his knowledge and experience with me.

To Bengt Ramne, I want to express my appreciation for his invaluable support and guidance throughout this project. His broad understanding, insights, and feedback have been instrumental in shaping my research and helping me to develop practical solutions that can be applied in real-world situations.

I would like to thank Melisa Nikmanesh, Sreeharsha Bikkireddy, and Fabian Thies who helped me with performing numerical simulations and carrying out case studies.

I am deeply grateful for the love and support of my parents and grandparents, who have always been there for me and provided a constant source of inspiration. Without their encouragement, I could not have made it this far in my academic journey.

I want to extend my love and congratulations to my girlfriend, Jingnan Zhang, who will be defending her PhD in June. Her dedication, perseverance, and intelligence have been an inspiration to me throughout my academic journey, and I am incredibly proud of her achievements. I am deeply grateful for her presence in my life. I know that she will go on to

achieve great things, and I am honored to be able to share in her journey as we pursue our academic careers together.

I also want to extend my gratitude to my beloved cat, Bubu. Though he is often naughty and mischievous, he has brought so much laughter and happiness to my life.

Finally, I want to acknowledge the contribution with resources from ScandiNAOS AB and Stena Rederi, financial support from Swedish Energy Agency, as well as computational support from Swedish National Infrastructure for Computing (SNIC), partially funded by the Swedish Research Council. These supports made this research possible.

To all those who have contributed to this work and to my education as a whole, thank you for being a part of my journey.

Heng Zhu
Gothenburg, March 2023

Contents

List of appended papers

This thesis consists of an extended summary and the following appended papers.

For Papers I and II, the author contributed to the ideas presented, planned the paper, did most of the modeling, simulation, and post-processing work, and wrote most of the manuscript.

For Paper III, the author contributed to the ideas presented, planned the paper, did some of the simulation work, did most of the modeling and post-processing work, and wrote most of the manuscript.

Paper I Zhu, H., Yao, H.-D., Thies, F., Ringsberg, J. W., & Ramne, B. (2023). Propulsive performance analysis of a rigid wingsail with crescent-shaped profiles based on unsteady RANS CFD. *Submitted to Ocean Engineering.*

Paper II Zhu, H., Yao, H.-D., & Ringsberg, J. W. (2023). Unsteady RANS and IDDES studies on a telescopic crescent-shaped wingsail. *Under review in Ships and Offshore Structures.*

Paper III Zhu, H., Bikkireddy, S., Ringsberg, J. W., Yao, H.-D., & Ramne, B. (2023). Structure analysis of lightweight sail structures for wind-assisted ship propulsion. In J. W. Ringsberg & C. Guedes Soares (Eds.), *Advances in the Analysis and Design of Marine Structures: Proceedings of 9th International Conference on Marine Structures (MARSTRUCT 2023, 3–5 April 2023, Gothenburg, Sweden)* (pp. 327–335). CRC Press. http://dx.doi.org/10.1201/9781003399759-36.

List of other papers by the author

In addition to the appended papers, the author of this thesis authored or co-authored the following publications and manuscripts.

Paper A Zhu, H., Nikmanesh, M. B., Yao, H. -D., Ramne, B., & Ringsberg, J. W. (2022). Propulsive performance of a novel crescent-shaped wind sail analyzed with unsteady RANS. *Proceedings of the ASME 2022 41st International Conference on Ocean, Offshore and Arctic Engineering (OMAE 2022), June 5–10, Hamburg, Germany* (Vol. 85925, p. V007T08A053). http://dx.doi.org/10.1115/OMAE2022-79867.

Paper B Zhu, H., Yao, H.-D., & Ringsberg, J. W. (2022). Unsteady RANS and IDDES study on a telescopic crescent-shaped windsail. *Proceedings of the 7th International Conference on Ships and Offshore Structures (ICSOS 2022), October 17–19, Ålesund, Norway.*

Paper C Zhu, H., Chernoray, V., Ringsberg, J. W., Yao, H.-D., & Ramne, B. (2023). Structure analysis of lightweight sail structures for wind-assisted ship propulsion. In J. W. Ringsberg & C. Guedes Soares (Eds.), *Advances in the Analysis and Design of Marine Structures: Proceedings of 9th International Conference on Marine Structures (MARSTRUCT 2023, 3–5 April 2023, Gothenburg, Sweden)* (pp. 781–787). CRC Press. http://dx.doi.org/10.1201/9781003399759-86.

Paper D Zhu, H., Thies, F., Ringsberg, J. W., & Ramne, B. (2023). Development and performance analysis of a crescent-type sail for WASP applications. *Proceedings of the International Academic Conference on Shipping, Sustainability & Solutions 2023 (SSS 2023), March 2–3, Hamburg, Germany.*

Paper E Pradhan, P., Yao, H.-D., Joshi, V., Zhu, H., Ringsberg, J. W., Zhao, X. (2023). Actively controlled propulsion of lined-up triple foils with flapping motions. *Manuscript to be submitted to Physics of Fluids.*

Nomenclature

A_S	Sail area [m^2]
C_D	Drag force coefficient [-]
C_L	Lift force coefficient [-]
C_M	Moment coefficient [-]
C_p	Pressure coefficient [-]
C_T	Thrust force coefficient [-]
E	Young's modulus [GPa]
F_D	Drag force [N]
F_L	Lift force [N]
F_S	Side force [N]
F_T	Thrust force [N]
H	Sail height (spanwise length) [m]
L_c	Chord length [m]
P	Pressure [Pa]
Q	Q-criterion [s^{-2}]
Re	Reynolds number [-]
V_{AW}	Apparent wind speed (inlet velocity) [$\mathrm{m/s}$]
V_S	Ship speed [$\mathrm{m/s}$]
V_{TW}	True wind speed [$\mathrm{m/s}$]
V_X	Streamwise velocity [$\mathrm{m/s}$]
V_Z	Spanwise velocity [$\mathrm{m/s}$]
y^+	Dimensionless wall–normal distance [-]
α	Angle of attack [°]
α_c	Critical angle of attack [°]
θ_{AW}	Apparent wind angle [°]
θ_{TW}	True wind angle [°]

μ	Dynamic viscosity [Pa · s]
ν	Poisson's ratio [-]
ρ	Material density [kg/m^3]
ρ_{air}	Air density [kg/m^3]
σ_{Mises}	Von Mises stress [MPa]
σ_{ij}	Stress [MPa]
σ_{yield}	Yield stress [MPa]
τ	Wall shear stress [MPa]
ω_X	Streamwise vorticity [s^{-1}]
ω_X^*	Non-dimensional streamwise vorticity [-]
ω_Z	Spanwise vorticity [s^{-1}]
ω_Z^*	Non-dimensional spanwise vorticity [-]

1 Introduction

This chapter provides the background for this thesis, as well as a literature review, the aims and motivations of the present research.

1.1 Background and motivation

1.1.1 The renascence of sailing

Sailing involves the wind acting on sails, wingsails, or kites to propel ships navigating on the surface of the water. This is an ancient method of transportation that dates back thousands of years. The history of sailing can be traced back to 6000 BC and onwards in Mesopotamia, where small boats were used for transportation and fishing (Carter, 2002). In the Near East, excavations have provided evidence for sailing boats having existed between 6000 and 4300 BC (Snell, 2008). The earliest pictorial representation of sailing in history is a sailboat made in ancient Egypt around 3100 BC (Casson, 1995). The Austronesians produced the first ocean-going sailing yacht in present southern China, which led to an expansion across the South Pacific between 3000 and 1500 BC (Mahdi, 1999). The Greeks and Phoenicians then boosted seaborne trade with the development of sailing and shipbuilding technology by around 1200 BC (Johnstone, 2013). In the Mediterranean, single-yarded lateen sails arose by around 100 BC (Campbell, 1995). During the early period of their use, sailing boats could only sail downwind, but at the start of the AD period, people from the Malay Archipelago crafted large ships and were able to sail against the wind (Ellis, 2005).

Over time, sailing technology evolved and became more advanced. By the 14th century, European sailors had developed a new type of ship, known as the caravel, which was faster and more maneuverable than previous designs. During the 15th–19th centuries, termed the Age of Sail (Gaynor, 2013), fore-and-aft sails were invented and developed in Europe, which improved the upwind sailing ability of European vessels (Castro et al., 2008). However, sailing relies on the weather, which is variable. Therefore, the use of wind power as the primary source of propulsion for ocean-going ships significantly declined after the invention of steamships during the Industrial Revolution.

By the 1920s, few sails were applied to ocean-going ships. However, the development of sails never ceased (Atkinson et al., 2018). In 1979, oil prices suddenly increased significantly, which is known as the "1979 oil crisis." This event led to an exploration of developments in potential alternative propulsion systems (Viola et al., 2015). Sail technology, an ancient means of propulsion, became popular again during this period (Satchwell, 1985).

Nowadays, transportation accounts for a large proportion of greenhouse gas (GHG) emissions. According to data from 2017, as shown in Figure 1, transportation accounted for 24% of the EU's GHG emission (EUROSTAT, 2019). Based on statistical data from 2014, approximately 90% of the world trade volume is transported by shipping fleets (International Chamber of

Shipping, 2014). Hence, thousands of ships that perform shipping tasks consume vast quantities of fuel for propulsion and discharge plenty of GHGs. For instance, a pure car and truck carrier (PCTC), may consume 30~60 tons of fossil fuel per day depending on how it is operated (Bialystocki & Konovessis, 2016). It is estimated that ocean-going ships globally consumed approximately 250~325 million tons of fuel per year from 2007–2012 on average, resulting in approximately 740~795 million tons of CO_2 emissions (Smith et al., 2015). A previous study forecasted that the current level of the world's transportation needs will probably double by 2050 (Gadonneix et al., 2011).

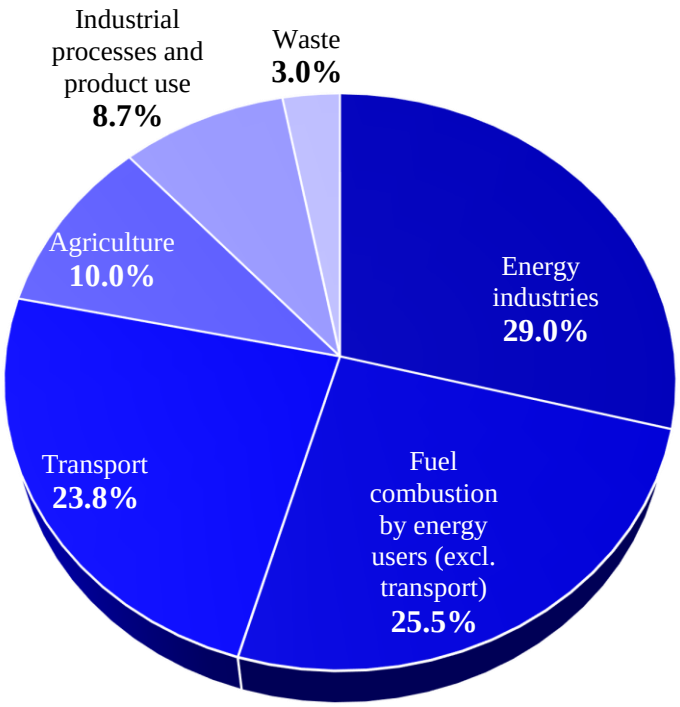

Figure 1. Share of EU greenhouse gas emission by source in 2017 (EUROSTAT, 2019).

In recent years, governments and organizations have made many important decisions to reduce GHG emissions. In 2017, the Swedish parliament decided that Sweden will be fossil fuel-free by 2045 at the latest. Swedish domestic GHG emissions from transportation will also be reduced by at least 70% between 2010 and 2030. Simultaneously, due to the agreement of the International Maritime Organization (IMO), shipping must become more energy-efficient, and before 2050, the shipping industry must reduce its GHG emissions to 50% of the level in 2008 (IMO, 2018).

There is no doubt that the set goals are ambitious. To reach them, the development and implementation of solutions must intensify, and the fossil fuel used in maritime transportation must be replaced by renewable alternatives. There are several renewable alternatives to fossil fuels that can be used in maritime transportation, including biofuels, hydrogen, wind power, solar power, and battery power. Among these, wind is a renewable resource that is readily available in large quantities, and wind energy is ideally suited to maritime transportation, as maritime transportation can use it efficiently and without unnecessary energy conversions. To

achieve an energy-efficient and sustainable society, the use of wind power for the propulsion of maritime vessels should be maximized. Therefore, wind-assisted ship propulsion (WASP) for large commercial ships is considered a promising solution to reduce shipping's dependence on fossil fuels.

1.1.2 Principles of sailing

To make it more convenient to explain the methodology applied in this thesis, some of the principles of sailing are first introduced.

For ships using rigid wingsails, the thrust propelling the ships originates from the wind loads on the sails. Usually, the thrust force is transferred through the mast from the sails to the ship. The external loads on the sail depend on the speed of the apparent wind, which is the wind that the ship and sails are experiencing. Figure 2 presents the wind triangle, where the apparent wind speed, i.e., the wind speed relative to the ship, and the apparent wind angle can be calculated using Equations (1) and (2), respectively.

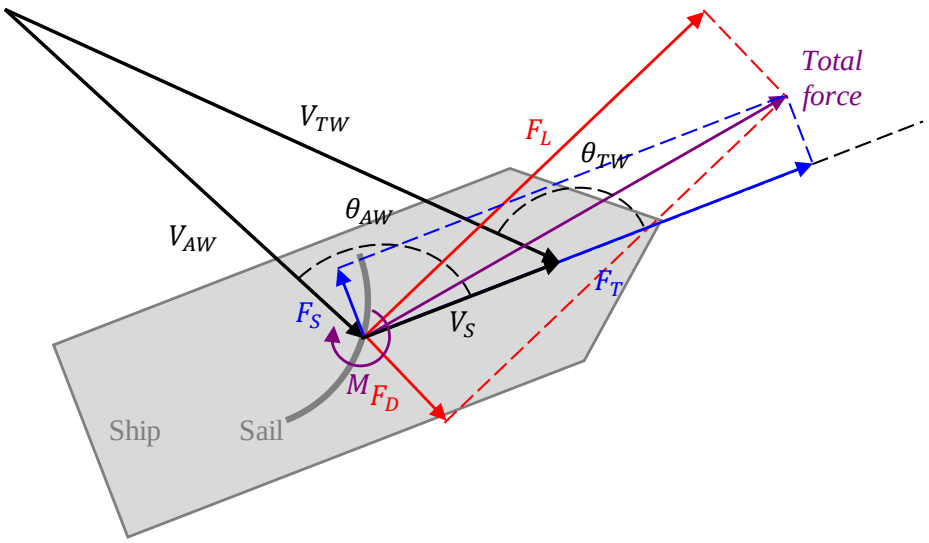

Figure 2. The wind triangle and loads on the sails.

$$V_{AW} = \sqrt{V_S^2 + V_{TW}^2 + 2V_S V_{TW} \cdot \cos\theta_{TW}} \tag{1}$$

$$\theta_{AW} = \tan^{-1}\left(\frac{V_{TW} \cdot \sin\theta_{TW}}{V_S + V_{TW} \cdot \cos\theta_{TW}}\right) \tag{2}$$

The external loads on the sail include the force and moment, as Figure 2 shows. Per aerodynamics, the component of the total force on the sail that is parallel to the apparent wind speed is the drag force, while that perpendicular to the apparent wind speed is the lift force. On the other hand, practically, the component that is parallel to the ship speed is the thrust force, which can be calculated using Equation (3), while that perpendicular to the ship speed is the

side force. The magnitude of the thrust force represents the propulsive performance of the WASP system, so one of the most important objects of a WASP concept is to generate the greatest possible thrust force. The side force does not account for the propulsion and causes heeling and rolling, as well as drift and additional induced resistance.

$$F_T = F_L \cdot \sin \theta_{AW} - F_D \cdot \cos \theta_{AW} \tag{3}$$

The non-dimensional force coefficients are represented by C_L in Equation (4). Similarly, C_D and C_T can be defined. The moment coefficient is defined using Equation (5).

$$C_L = \frac{F_L}{0.5\rho V_{AW}^2 A_S} \tag{4}$$

$$C_M = \frac{M}{0.5\rho V_{AW}^2 A_S L_c} \tag{5}$$

The power source of sailing is the wind, but the direction of travel relative to the wind is what determines its ability to generate forward motion. This direction is referred to as the point of sail and can be divided into segments of 45°, starting at 0° directly into the wind. The zones spanning 45° on either side of the wind are considered "no-go" zones (Cunliffe, 2016) since here, a sail is nearly unable to generate power from the wind (Kimball, 2009). When sailing on a course as close to the wind as possible, which is approximately 45°, the craft is "close-hauled". At 90° off the wind, the craft is on a "beam reach". At 135° off the wind, the craft is on a "broad reach". When sailing in the same direction as the wind, which is 180° off the wind, the craft is "running downwind". Between close-hauled and broad reach, the sail acts as a wing, with lift predominantly propelling the craft. Contrastingly, from broad reach to downwind, the sail acts as a parachute, with drag predominantly propelling the craft. For a craft with little forward resistance, such as ice boats and land yachts, this transition occurs further off the wind than for sailboats and sailing ships.

Compared with conventional airfoil profiles, such as the NACA 0015, profiles that are symmetric at both edges, i.e., the leading edge and the trailing edge share the same shape, will be operated differently when changing tack. Take the crescent-shaped profile as an example for comparison. The conventional NACA profile will always have the same leading edge, but the high-pressure side will become the low-pressure side when changing from one tack to the other, as shown in Figure 3(a). This type of profile operates like a modern Bermuda-type sail. However, a crescent-shaped profile will swap the leading and trailing edges when changing tack, but the same side will always be the high-pressure side and the opposite side will always be the low-pressure side, as shown in Figure 3(b). This makes wingsails with crescent-shaped profiles easier to operate under downwind conditions.

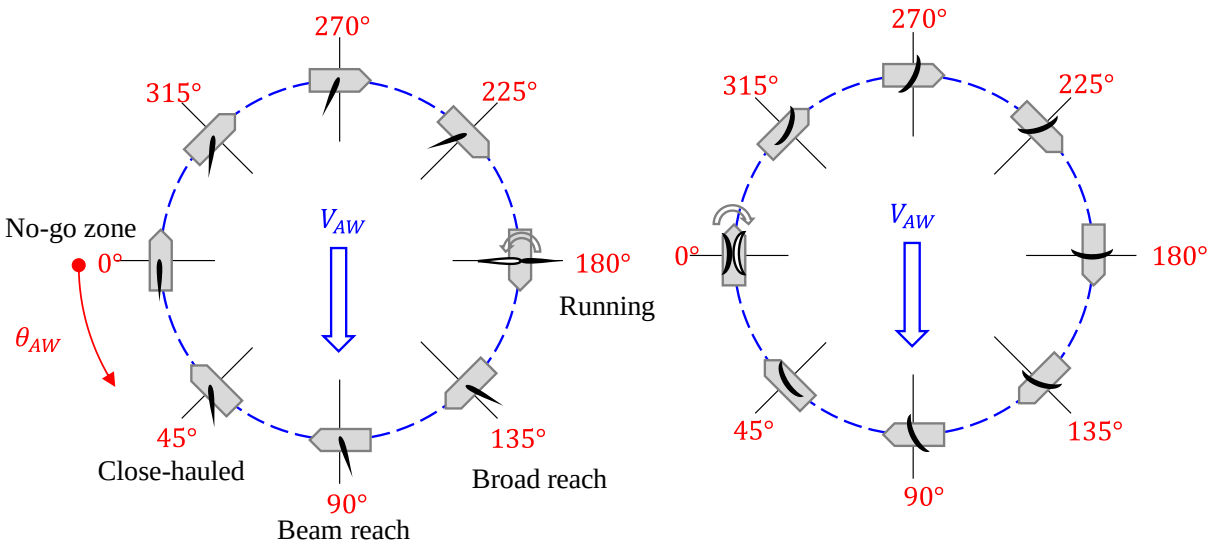

(a) Symmetric profile (NACA 0015). (b) Crescent-shaped profile.

Figure 3. Changing tack with an aerodynamically symmetric profile and a crescent-shaped profile.

1.1.3 Concepts of wind-assisted ship propulsion

For wind energy to be relevant in maritime transportation, it is necessary for sail arrangements to significantly contribute to vessel propulsion under most of the wind conditions to which vessels are exposed.

The propulsion power of a sail is generated by the apparent wind that the arrangement experiences. The apparent wind is the vector sum of the headwind and the velocity of the true wind. Due to the headwind component, the apparent wind will, over time, always be more ahead than astern. Therefore, a sail arrangement needs to perform well when the wind is coming forward from abeam (between beam reach and close reach), and it needs to give driving force at small relative angles of the wind.

Different categories and innovative WASP technologies have been proposed, such as rotor sails, vertical airfoils (which are also termed ventifoils or suction wings), kites, wind turbines, and various wingsails (Khan et al., 2021). Several of these are already being used on passenger and merchant vessels, while some are still being subjected to further optimization or full-scale testing in research projects (Cairns et al., 2021). Lu and Ringsberg (2020) compared three sail technologies, the Flettner rotor, the DynaRig, and a wingsail, in terms of their actual fuel savings for a specific ship sailing on specific voyage routes. The study showed that WASP technologies reduce fuel consumption by several percentage points, but it was not as much as expected because the amount of fuel savings depended on many factors for each of the three technologies. One of the most crucial factors was the sail's performance in a wide range of angles of attack related to the ship's heading direction. A sail's performance also depends on the aerodynamic interactions among the multiple sails on the ship.

A wingsail is an innovative type of sail that is designed to provide lift on both sides, similar to an airplane wing. Throughout the years, some projects were undertaken to develop and evaluate different concepts for WASP systems using rigid wingsails to reduce fuel consumption in excess of 30% (Hamada, 1985).

Compared with other concepts, rigid wingsails have some advantages:

- Compared with traditional soft sails, the main advantages of rigid wingsails are that they maintain their shape in light winds and are more robust to control since there is no rope that can become entangled (Sauzé & Neal, 2008). Meanwhile, rigid wingsails have simpler structures and are easier to design and operate (Silva et al., 2019).
- Unlike kite sails, rigid wingsails can propel ships via drag force and lift force, allowing ships to navigate against the wind (Kimball, 2009). The area of a kite sail is limited by what can be handled during the setting and hauling of the kite.
- The Oceanbird project (Workinn, 2021) even aims to achieve a 90% reduction of fuel consumptions, which is much higher than Flettner rotors' saving of 8% on average (International Transport Forum, 2020), 30% for tankers (Tillig & Ringsberg, 2020), and around 50% for maximum potential (Traut et al., 2014). Furthermore, the Flettner rotating cylinder concept is also limited in the maximum diameter of the cylinder, and the height is limited since it must be able to withstand the harshest wind conditions that the ship is designed for. Due to the bluff body, Flettner rotors also suffer from added drag, resulting in extra resistance when the rotors do not operate (Khan et al., 2021). Moreover, rigid wingsails show better propulsive performance than Flettner rotors under downwind conditions, where the drag force mainly contributes to propulsion (Lu & Ringsberg, 2020).

A fixed wingsail can have a larger sail area than Flettner rotors, but the size of the wings is limited by the available surface on deck, where they are stowed. The solution to maximizing the sail area under normal wind conditions while limiting the area during harsher winds is to make the sail area flexible. By using telescopic rigging, the sail area can be adjusted according to the wind conditions at the time. By making the rig foldable, the structural stresses under extreme weather conditions are further reduced, as well as the drag during unfavorable wind conditions. In the Effship project (Allenström et al., 2012), a telescopic wingsail arrangement with a crescent-shaped profile was developed. In the project, numerical simulations were executed, and different sail arrangements were analyzed. The results showed that the telescopic wingsail arrangement with a crescent moon airfoil has a better overall performance than the Flettner rotor and kit sail arrangements. Although the C_L of the crescent-shaped wingsail is lower compared with the Flettner rotor, the wingsail usually has a much larger sail area, so it can generate larger thrust. This solution was patented in Sweden (Fagerlund & Ramne, 2010).

Köhle et al. (2016) summarized the market potential and barriers of possible techniques of WASP, indicating that different solutions fit different applications. The proposed wingsail solution is one of few that can significantly contribute to the propulsion of larger tank and bulk transport ships on transcontinental routes (Allenström et al., 2012). While other solutions might

be better for ships with a smaller displacement, such as RoRo and RoPax ships, for tank and bulk transport ships, the telescopic arrangement can be retrofitted, making energy saving for existing ships possible. It should be noticed that relative saving is very much dependent on the ship's speed. A reduction in fuel consumption, i.e., relative savings, exhibits an upward trend with decreasing ship speeds. However, in most cases, the absolute amount of fuel saved, measured in tons of fuel, increases as the ship's speed increases. Therefore, a full-scale installation is expected to give a 20% reduction in fuel use for existing route time plans. Nevertheless, if routes and time plans are adapted to wind and weather conditions, the potential reduction can be several times larger.

The present thesis is motivated to reduce the carbon footprint of shipping by developing an innovative WASP system that will enable ships to use wind power as a complementary energy source to reduce their reliance on fossil fuels. It focuses on developing a new and innovative WASP system that will utilize advanced materials and technologies. By promoting the use of wind power in the shipping industry, this work will support the growth of renewable energy and contribute to the transition toward a low-carbon economy.

1.2 Overview of methods

1.2.1 Wind load prediction

To evaluate the propulsive performance of a WASP system, it is important to predict the wind loads on the sail, which is an aerodynamic problem. To solve this, some methodologies, such as theoretical, numerical, experimental, and empirical methods, can be used. Theoretical methods use aerodynamic theories such as thin-airfoil theory to deduce wind loads. These methods are normally efficient, but they are always based on some assumptions, resulting in their applicability to real-world problems being limited. Model-scale experimental methods, such as wind tunnel tests, provide direct predictions for flow characteristics. However, executing experiments is often expensive, experimental results are usually difficult to visualize, and there are considerable scale effects that make it difficult to predict full-scale performance. Empirical methods provide quick but approximate solutions to fluid flow problems, sometimes being limited in their accuracy and reliability. Among these, numerical methods have some advantages: They can be used to simulate complex fluid flow problems with high accuracy, offer a way to model full-scale problems to investigate the behavior of fluids under various conditions, and provide visualizations and detailed information about fluid flow characteristics.

Numerous studies have been conducted by using numerical methods to study the performance of WASP systems based on rigid sails. Ouchi et al. (2011) performed full-scale CFD simulations to evaluate the propulsive performance of a nine-wingsail system and conducted a case study for evaluation. Viola et al. (2015) developed a numerical optimization procedure for a rigid wingsail using the Reynolds-averaged Navier–Stokes (RANS) equation solver, which offered an efficient parametric sail aerodynamic analysis method. Lee et al. (2016) studied a series of rigid wingsails based on the NACA 0012 profile, conducted numerical aerodynamic analysis using a viscous Navier–Stokes flow solver, and established a design optimization

framework to maximize the thrust coefficient C_T. Ma et al. (2018) studied three typical airfoil-based sails using CFD simulations with the k–ω shear stress transport (SST) turbulence model. Persson et al. (2019) presented simplified approaches to model WASP systems, using a limited number of CFD simulation results to extrapolate propulsive performance under various conditions. Tillig and Ringsberg (2020) presented a novel approach to analytically capture aero- and hydrodynamic interaction effects on wind-propelled ships. Low aspect ratio wing theory was applied and modified to predict the lift and drag forces of hulls sailing at drift angles. The sails' aerodynamic interaction effects were captured by numerically solving the Navier–Stokes equations for incompressible, creeping flow. Malmek et al. (2020) developed two cost-effective aerodynamic methods to predict the performance of large-scale wingsails. One was based on the lifting line theory of potential flow in combination with pre-calculated two-dimensional RANS CFD data, and the other was a vortex lattice method (VLM). Zhu (2020), and Blount and Portell (2021) performed detached eddy simulation (DES) to study the performance of wingsails with a NACA 0015 profile under downwind conditions.

The studies mentioned above were mainly based on wingsails with conventional airfoil profiles, such as the NACA series. However, including camber in the profile geometry can significantly increase the lift coefficient, a mechanism that is also valid for sails. Atkinson (2019) performed three-dimensional CFD simulations to study a segment rigid sail. Nikmanesh (2021) proposed a type of crescent-shaped, cambered profile and predicted propulsive performance by performing unsteady RANS (uRANS) simulations based on the Spalart–Allmaras turbulence model, indicating that this type of profile provides a higher C_L, leading to larger thrust. Chen et al. (2022) introduced a set of arc-shaped wingsails and studied their aerodynamic characteristics by performing two-dimensional simulations. In October 2022, Japanese shipping company Mitsui O.S.K. Lines (MOL) delivered the world's first coal carrier equipped with crescent-shaped rigid wingsails (Prevljak, 2022).

1.2.2 Energy saving evaluation

The WASP system design is a type of systems engineering. The design parameters are coupled, which means that the relationship between them is one of mutual influence, condition, and transformation, presenting great complexity and considerable changeability. For example, if the area of the sail increases, the thrust force and side force will increase, as well as the yaw and heeling moments. Therefore, resistance also increases. The designer needs to judge and weigh since both the thrust and resistance increase (Viola et al., 2015).

Several studies have been carried out to analyze and evaluate the propulsive performance of WASP systems. Kijima et al. (1990) developed the Velocity Prediction Program (VPP), which is a computer program and a common approach used to solve the coupled equations of motion on high-performance sailing ships. The VPP is based on computational fluid dynamics, experimental fluid dynamics, or analytical formulations. Models of how the aero- or hydrodynamic forces and moments vary with key design parameters are used to solve the equations of motion for the ship (Larsson, 1990).

Tillig et al. (2017) developed a generic ship energy system model that Tillig and Ringsberg (2019) further developed. This model was later named ShipCLEAN (Tillig et al., 2019) and is aimed at predicting the fuel consumption of ships at sea while considering the external loads caused by wind, waves, currents, etc., and it is available for WASP components. By applying the model, Lu and Ringsberg (2020) compared three sail technologies (the Flettner rotor, the DynaRig, and a wingsail) in terms of the actual fuel savings for a specific ship sailing on specific voyage routes, showing that WASP technologies reduce fuel consumption by several percentage points but not as much as expected. One of the crucial factors found was the sail's performance with the wide range of α related to the ship's heading direction. A sail's performance also depends on the aerodynamic interactions among the multiple sails on the ship.

1.2.3 Structural response analysis

Sails must be strong and durable enough to withstand the forces that they will experience in use, including wind and wave loads, as well as other environmental factors. For application in large commercial ships, the wingsail is usually supported by an unstayed mast installed on the deck of the ship, so its structural response is similar to a cantilever that is subjected to a flow of air.

Today, numerical calculation methods based on the finite element method (FEM) are commonly utilized and have proven useful for structural analysis. Applicable mechanical solutions for a telescopic rig can also be found in existing mobile crane solutions. The shape, construction, and dimension of the sail panels can be derived using analytical, empirical, or modeling methods. However, to further optimize the construction for increased propulsion and sustainability, better calculation methods must be developed in parallel with the construction work. Therefore, a modern version of the FEM is used to analyze the structure and its performance.

In recent years, some researchers have performed structure analysis on WASP systems, though most of the studies that evaluated these systems focused on the fluid aspect. Ouchi et al. (2011, 2013) proposed a conceptual design for a telescopic rigid wingsail and used finite element analysis (FEA) to analyze deflection and stress distribution throughout the wingsail. Hu et al. (2015) investigated the structure design, dynamic performance, and control strategy of wingsails for large, ocean-going, sail-assisted ships.

As mentioned in Section 1.2.1, to achieve a higher C_L, the sectional profile of the wingsail can include significant camber. Nevertheless, because of camber, the wingsail is expected to induce strong flow separation, which results in vortex-induced vibration and fatigue that may lead to increased strength requirements (Storhaug et al., 2022). Due to strong flow separation, the structure of the wingsail will experience deformation, which can, in turn, affect the flow field. Therefore, it is necessary to analyze the fluid–structure interaction (FSI) of the wingsail (Bak et al., 2013). FSI models are an indispensable tool for calculations on large wind turbines and significantly increase calculation accuracy for large sail structures.

1.3 Objectives and goals

Recent studies on WASP have indicated that there are still several difficulties in developing WASP systems. In terms of technology, WASP systems require complex design and engineering integration, and there are many technical challenges associated with optimizing the performance of the sails and ensuring their stability and reliability.

1.3.1 Aerodynamic efficiency

One of the most important factors for aerodynamic efficiency is the design of the sail. The sail design must be optimized to ensure maximum performance and efficiency. This includes choosing the right materials, considering aerodynamic and hydrodynamic forces, and accounting for the effects of winds and waves. Take wingsails as an example: To contribute as much as possible to propulsion, the wingsail is expected to generate as great lift force and drag force as possible under sidewind and downwind conditions, respectively. In addition, for a given thrust force, a better performing aerodynamic profile will require less sail area, e.g., lower mast meaning, lower weight of the rig, and a lower heeling moment.

The first goal of this study is to introduce a novel telescopic wingsail design with a new crescent-shaped profile and establish high-fidelity numerical methods for predicting the wind loads. This profile is expected to be more aerodynamically efficient, i.e., generate higher C_L leading to higher C_T at relevant wind angles. To evaluate its performance, two- and three-dimensional CFD simulations are used, in addition to the uRANS and improved delayed detached-eddy simulation (IDDES) methods and the $k-\omega$ SST turbulence model. One of the sub-objectives of this study is to address suitable sail configurations with an advantageous C_L to maximize F_T for large sailing merchant ships and their ship operation profiles. This thesis compares the propulsive performance of two rigid wingsails with different sectional profiles (NACA 0015 and crescent-shaped). The analysis also focuses on exploring flow field properties, especially unsteady characteristics such as flow separation, wake flow, and tip vortices, as well as the impacts of external loading conditions on the wingsails.

1.3.2 Considerable fuel saving

WASP can be a good alternative for retrofitting existing vessels to reduce their dependence on fossil fuels, but sails are usually not the only solution, so WASP should be combined with other energy sources. Hence, studying how different sail technologies will be used and for which ship types and routes is useful.

The second goal of this study is to evaluate the level of relative fuel saving by applying the novel wingsail. In this thesis, the lift and drag coefficients from the CFD simulations are later used as input for the performance prediction model ShipCLEAN to perform studies with a real ship (a medium-sized tanker) using its operational data and hindcast weather. Further, the performance of the crescent-type sail is benchmarked against the performance of Flettner rotors.

1.3.3 Structural integrity

In practice, the structure of the wingsail is usually complex and includes panels, stiffeners, and horizontal section plates. To conduct FSI analysis, the structural model should, therefore, be simplified. Otherwise, the fluid mesh of the prism layers may need to be re-generated at every timestep to resolve the boundary layer flow and prevent the coupled simulation from diverging, which is computationally expensive. Therefore, the structural response of the full structure should be analyzed first to guide how the geometry of the structure can be simplified when performing FSI analysis. Moreover, since the wingsail is installed on the deck and is a considerable size, its weight must be kept as low as possible to ensure that it does not affect the cargo capacity and the stability of the hull.

The third goal of this study is to propose a lightweight design for telescopic wingsails and establish a numerical model to analyze its structural response. The present study uses quasistatic FEA to study the structural responses of a crescent-shaped wing sail rig. The objective of the structural analysis is to compare a few conceptual designs of telescopic rigs, ranging from a rig with a center mast to a mast-less rig. The rigs are compared against three criteria: the structural response (displacement), strength (ratio stress response/yield), and weight of the sail's rig. The external wind loads applied to the sails in the FEAs have been simulated and calculated using aerodynamic simulations in previous studies that the authors have conducted. The advantages and disadvantages of each concept are discussed, aiming to provide a good strategy for structural design and the arrangement of similar wind-assisted propulsion facilities. The results of the thesis will be used in future work as a guide for structural optimization and FSI analysis.

1.4 Assumptions and limitations

When comparing the newly introduced crescent-shaped profile with the NACA 0015, profiles with a flap are not considered. Even though the performance of the NACA 0015 profile can be improved with a flap, this is difficult to apply to a telescopic concept.

In the CFD simulations, the apparent wind, i.e., the inlet velocity, is assumed to be a uniformly distributed horizontal flow. Although real wind conditions are complex and variable, this assumption is considered reasonable because the Reynolds number of the wingsail profiles is normally in the range of 3×10^6 to 3×10^7, in which the force coefficients are not sensitive to the Reynolds number, as presented in Paper C. However, when analyzing fuel saving performance using ShipCLEAN, the wind profile is considered.

The geometry of the wingsail is simplified when performing CFD simulations. In the three-dimensional CFD simulations, the wingsail is simplified to uniformly extruded geometry, so the size differences among the different sections of the wingsail are not considered. The mast is not included since there is gap between the wingsail and the deck is only 5% of the entire height. Only one wingsail is considered at this stage, so the multi-wingsail interaction is neglected. The flow field induced by the hull of the ship is neglected in the CFD simulations.

The nonuniformity and instantaneity of the wind loads are not considered in FEA simulations. The wind loads are assumed to be uniformly distributed pressure on the pressure side and suction side, respectively. In addition, the structural analysis is based on quasi FEA simulations, so the dynamic response and FSI are not studied at this stage.

The material properties of the structure are assumed to be linear and elastic, which means that the nonlinear material properties are ignored. Since a factor of safety of 2 against the yield stress is introduced, the stress does not exceed the yield stress. The buckling analysis is limited only in terms of normal stress, and buckling due to shear stress is not studied. From the FEA results, the magnitude of shear stress is much lower than normal stress.

1.5 Outline of the thesis

The present thesis is divided into four parts. In Chapter 1, the background information and related studies are introduced, including an explanation of the research aims and motivations. In Chapter 2, the methodology used in this thesis is presented. The generated concept design and the established numerical model are also described and explained in this chapter. In Chapter 3, selected results from the three appended papers are summarized. In Chapter 4, a conclusion is provided, and possible future work is discussed.

2 Methodology

This section presents a brief summary of the methods and models used throughout Papers I, II, and III before examples of the key results are presented in Section 3. The workflow is shown in Figure 4. The red arrows in Figure 4 represent the methods and results that were transferred between papers. For example, the three-dimensional CFD simulations in Paper II were improved versions of those established in Paper I.

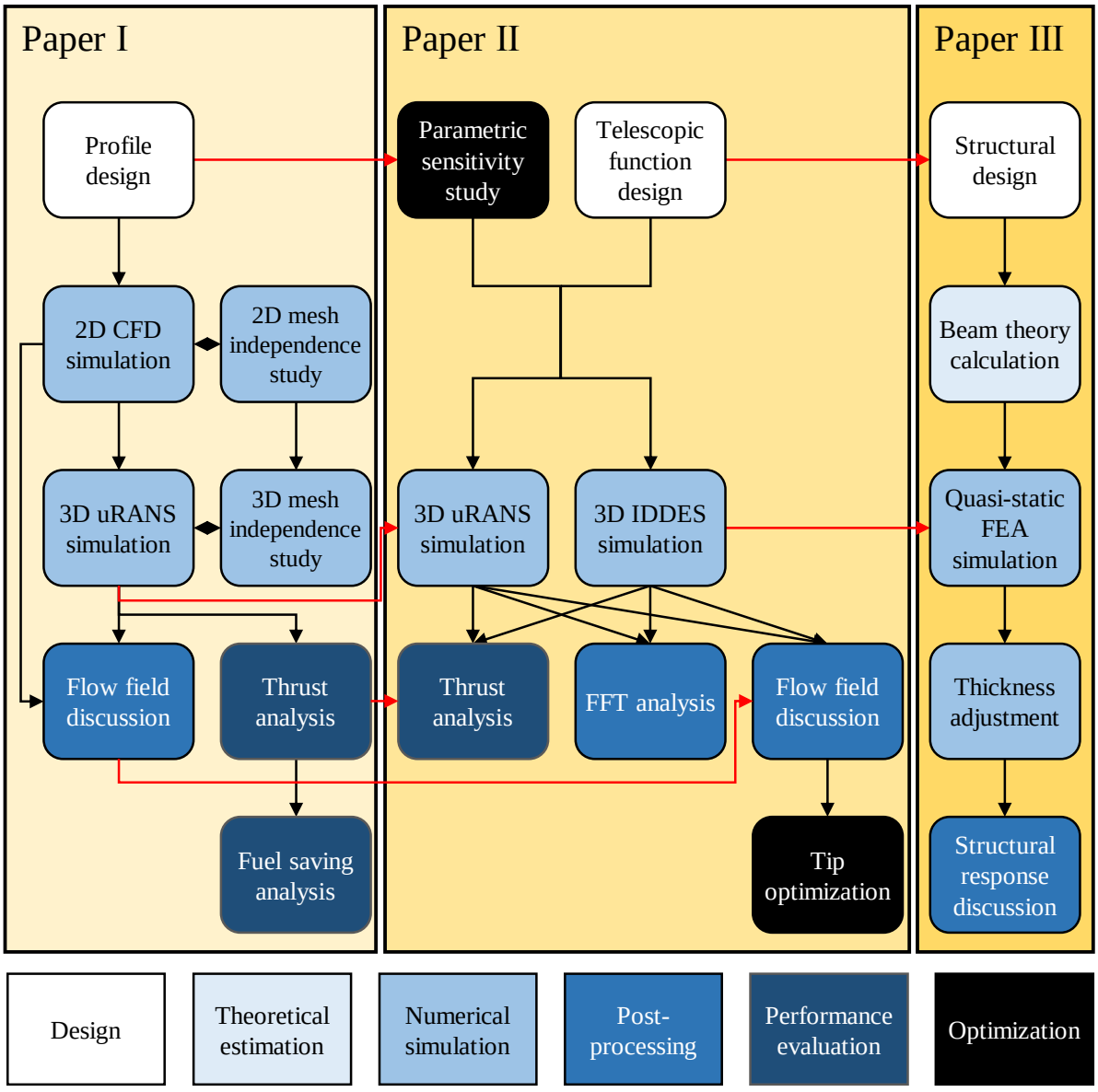

Figure 4. Workflow of the appended papers.

The main technology and methods that are developed in this thesis are outlined as follows:

- First, the design of a telescopic wingsail rig that can be adjusted for various wind conditions. This conceptual design is expected to provide notable thrust force. The concept design is discussed in detail in Sections 2.1.1 and 2.1.3.

- Second, the development of numerical models for predicting and evaluating the performance of the WASP system. This step includes developing a CFD model for predicting wind loads on the wingsail and an FEA model for analyzing the structural response of the wingsail structures. The CFD model is described in Section 2.2, and the FEA model is described in Section 2.3. The time-averaged CFD results are summarized in Section 3.1.1, and the unsteady characteristics are summarized in Section 3.2. The FEA results are summarized in Section 3.3.
- Third, performance analysis and evaluation of the conceptual sail at the system level. A model for the telescopic wingsail rig is entered into the ShipCLEAN model for estimating its fuel saving performance, and its performance is evaluated and compared with that of other sailing concepts. The method of the fuel saving analysis is shown in Section 2.4, and the results are summarized in Section 3.1.2.

2.1 Design and physical conditions

2.1.1 Crescent-shaped profile

In this thesis, a wingsail with a horizontal section profile is proposed, as illustrated in Figure 5: a simple crescent shape comprising arcs and circles. There are four main design parameters: the chord length, edge radius, suction-side arc radius, and mast diameter. The shape of the profile, including the pressure-side arc radius, is determined using these four parameters. The arcs of the pressure and suction sides are symmetric around the symmetric axis (the dashed blue line in Figure 5). The radius of the edges is chosen to make the profile structurally sound.

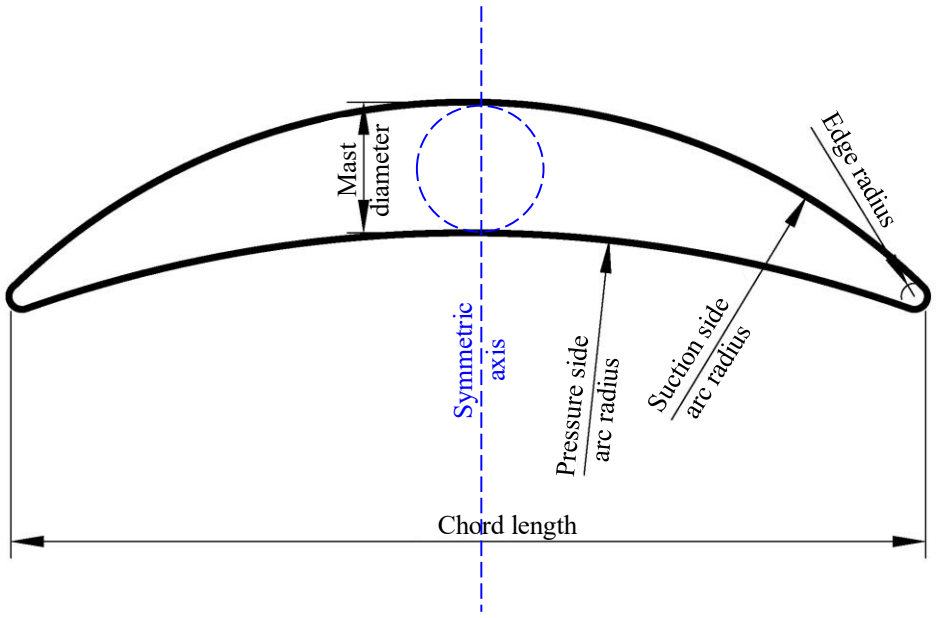

Figure 5. Design parameters of the crescent-shaped profile.

The mast diameter and suction-side arc radius are adjustable. The chord length is always set at $14\ \mathrm{m}$, and the edge radius is always $0.2\ \mathrm{m}$. The dimension parameters are suggested by ScandiNAOS AB according to their practice. A series of profiles are generated by varying the remaining two parameters and are labeled in the form "DxRy," where "x" represents the mast diameter and "y" represents the suction-side arc radius. For example, for the profile named "D2R8," the mast diameter is $2\ \mathrm{m}$ and the suction-side arc radius is $8\ \mathrm{m}$, which results in an arc radius of $10.67\ \mathrm{m}$ on the pressure side.

2.1.2 Wind conditions

The sectional profiles, wind conditions (apparent wind speeds and angles of attack), and height of the wingsail that are studied in each paper are listed in Table 1. Detailed information about fluid properties can be found in Papers I and II.

Table 1. The wingsail geometry and wind conditions studied in each paper.

	Sectional profile	V_{AW}	H	α
Paper I	NACA 0015 D2R10	$25\ \mathrm{m/s}$	$72\ \mathrm{m}$	$16°$ $-2° \sim 95°$
Paper II	D2R8	$8\ \mathrm{m/s}$ $32\ \mathrm{m/s}$	$74\ \mathrm{m}$ $32\ \mathrm{m}$	$19°, 21°, 23°$
Paper III	D2R8	$16\ \mathrm{m/s}$	$74\mathrm{m}$	$23°$

In Paper I, to simulate a critical condition, i.e., a condition with high wind speeds, a uniformly distributed inlet flow velocity of $25\ \mathrm{m/s}$ is used to simulate wind speed, so the Re is 2.3×10^7, calculated based on the sail's sectional profile chord length. The height of the sail, H, is preliminarily defined as $72\ \mathrm{m}$. According to wind tunnel tests (Sheldahl & Klimas, 1981), when the Reynolds number is 1×10^7, the critical angle of attack α_c of the NACA 0015 foil is approximately $16°$. A previous study (Nikmanesh, 2021) indicated that for the newly introduced crescent-shaped profile, the α_c is around $20°$. Therefore, the comparison between the two- and three-dimensional simulations, as well as the comparison between different boundary conditions, is based on α_c, with the angle of attack being $16°$ for the NACA 0015 foil and $20°$ for the crescent-shaped foil. Additionally, a wide range of α is also studied to predict propulsive performance. A series of two- and three-dimensional simulations with α from $-2°$ to $95°$ are performed.

The D2R8 profile is studied in Paper II, and three sets of three-dimensional simulation cases with $\alpha = 19°, 21°, 23°$ are performed. In Paper II, the height of the wingsail can be adjusted according to the apparent wind speed. Two conditions are simulated, the fully expanded condition and the fully retracted condition, with Re of 6.78×10^6 for the fully expanded condition and 2.71×10^7 for the fully retracted condition. According to the structure arrangement, the height of the wingsail is adjusted to $74\ \mathrm{m}$.

Following Paper II, in Paper III, which focuses on structural responses, the three-dimensional D2R8 profile is studied. The α with the highest C_L, i.e., 23°, is studied. A more critical fully expanded condition with $V_{AW} = 16$ m/s is applied.

2.1.3 Structural arrangement

The wingsail and its rig must have a lightweight design to reduce its influence on the ship's cargo capacity and fulfill any stability requirements. One challenge with this is that the wind loads acting on such a sail cause bending and torsion in its structure, which increase the required strength-to-weight ratio of the sail rig.

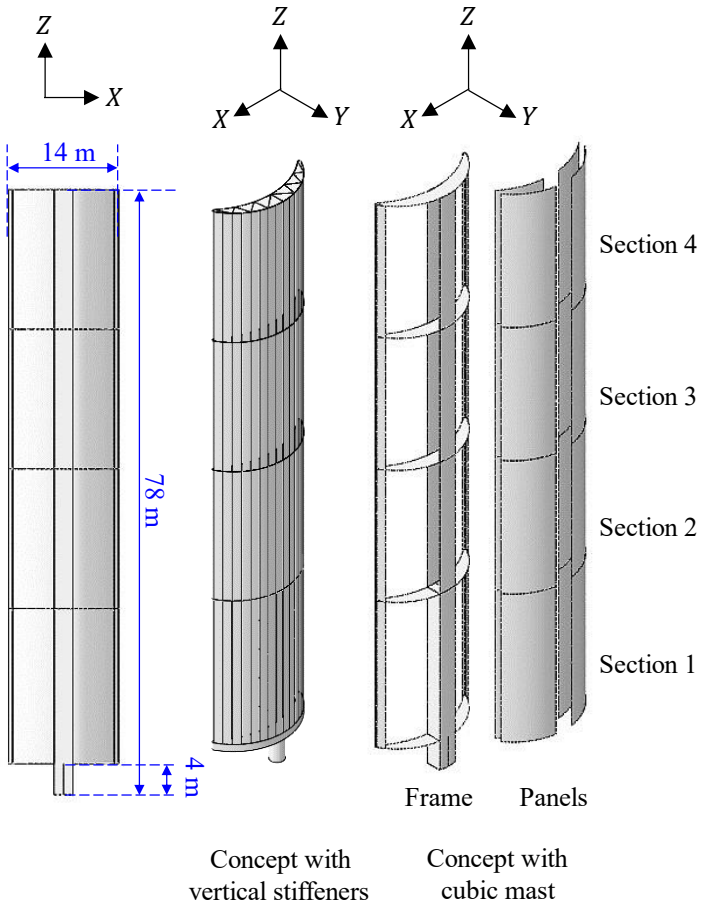

Figure 6. Size and structural designs of the wingsail.

In Paper III, the rigid wingsail is designed to be divided into four sections for the telescopic function, as shown in Figure 6. In this thesis, the lowest section is named "section 1," and the highest section is named "section 4." Two concept designs are presented. One of the concepts aims to use the global shell structure to bear global bending; several vertical stiffeners are used to increase the strength and rigidity of the wingsail structure. To release the stress concentration at the mast and lower part of section 1, some web structures are introduced. To prevent stress concentration in the mast and reduce the weight of the wingsail rig, another concept with a cubic mast is considered. The entire structure can be divided into two parts: the frame, which

is expected to bear global bending and torsion, and the panels, which are assumed only to suffer under local wind pressure. The mast only extends to the lowest section.

For the concept utilizing vertical stiffeners, since the whole surface needs to be strong enough to withstand global bending, all parts of the wingsail are made of steel (S275) (BS EN, 2004). However, aluminum (6061-T4) (ASTM, 2004) is introduced for the concept utilizing a cubic mast to reduce the total weight of the structure. For the concept utilizing a cubic mast, two material arrangements are studied: “steel frame, aluminum panels” and “all in aluminum.”

2.2 Computational fluid dynamics simulation

CFD simulations are applied for predicting the external load on the sail. The present study makes use of the mesh generators and solvers in the software STAR-CCM+ (Siemens PLM Software, 2021). In the CFD simulations, the wingsail is modeled as a uniformly extruded rigid body.

2.2.1 Domain and boundary conditions

Two-dimensional simulations are first performed to identify the α_c and provide a preliminary view of the flow field. Then, three-dimensional simulations with two types of boundary conditions are performed to study three-dimensional flow characteristics and the influence of tip vortices. One is a periodic top and bottom, and the other is a symmetric bottom and free tip, as Figure 7 shows.

A rectangular domain is used for the two-dimensional simulations, while a cuboid domain is used for the three-dimensional simulations. Full-scale simulations are performed in this thesis. For simulations with a periodic top and bottom, the spanwise size of the domain is the same as the spanwise length of the sail. For the two-dimensional simulations, the size of the domain follows the size of the bottom boundary of the three-dimensional simulations.

For both boundary conditions, the crossflow sides are set as pressure outlets to make the simulations as representative of real conditions as possible. For the two-dimensional simulations, the arrangement of the inlet and outlet boundaries follows the bottom boundary in Figure 7(b). The non-slip boundary condition is specified on the foil. The upstream boundary of the domain is assigned as a velocity inlet with a uniformly distributed inlet flow, representing apparent wind. A pressure outlet boundary condition with a zero-pressure loss coefficient is imposed on the downstream boundary of the domain with the crossflow sides. To prevent reversed flow from influencing the pressure outlet boundaries, the direction of the backflow is set to be extrapolated. The pressure loss at the pressure outlets is assumed to be 0, and the pressure jump under-relaxation factor is set as 0.5.

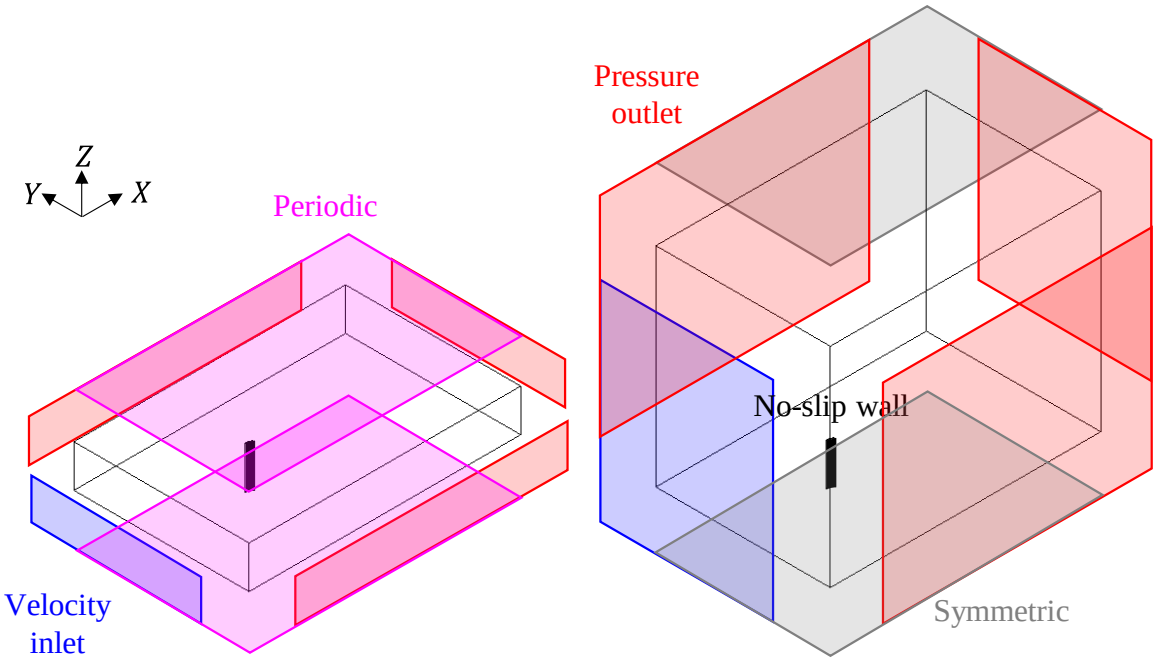

(a) Periodic top and bottom. (b) Free-stream tip and symmetric bottom.

Figure 7. The two types of boundary conditions used in the three-dimensional simulations. Red panels: pressure outlets; blue panels: velocity inlets; purple panels: periodic boundaries; gray panels: symmetric boundaries; black panels: no-slip walls.

2.2.2 Numerical mesh

An unstructured mesh with trimmed cell topology is mainly used for the simulations. Figure 8 shows the mesh of the three-dimensional simulation with a freestream tip and symmetric bottom, with typical cell sizes. The cells have a uniform size in each region at each refinement level. The region near the foil and the wake region are both refined, which can be seen in the section plane of $Z = 0.5H$ in Figure 8(b). The mesh in the wake region is refined using two parameters, the length and separate angle of the wake refinement. A cylindrical volumetric mesh refinement with a length of $1.1H$ is introduced to refine the mesh near the foil. The diameter of the cylinder is $1.4L_c$. Flow separation points are expected to distribute around the two edges, so, similarly, a more refined set of mesh is applied to the region near the edges of the foil to capture the flow separation phenomena, as Figure 8(c) shows. The refinement, aside from that of the prism layer, is based on the base size, labeled l_{base} in Figure 8.

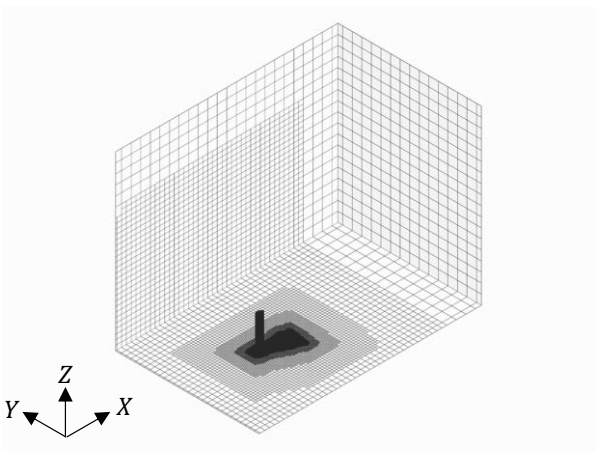

(a) Entire domain.

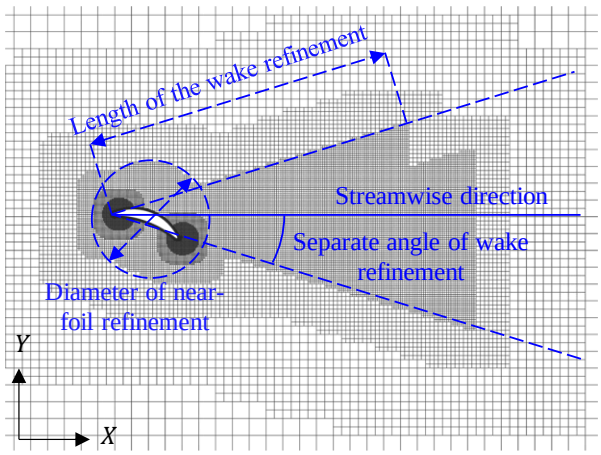

(b) Section plane at $Z = 0.5H$.

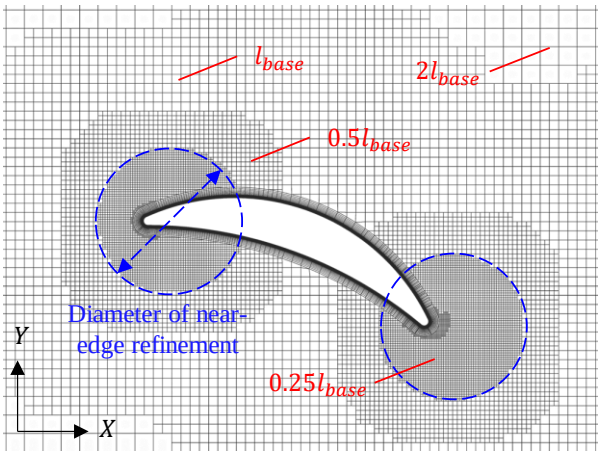

(c) Attached region near the foil, at the section plane of (b).

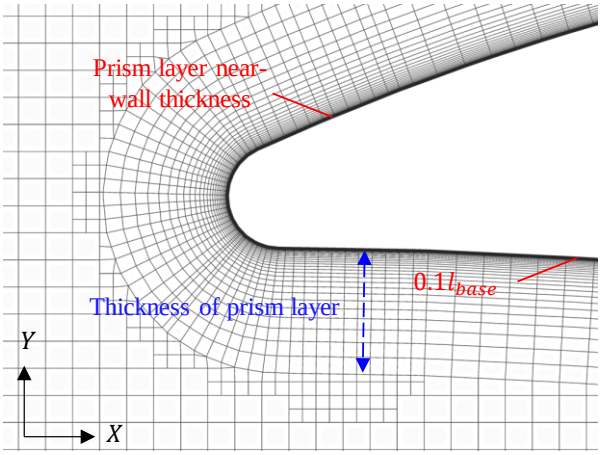

(d) Attached region near the leading edge, at the section plane of (b).

Figure 8. Three-dimensional trimmed mesh when $\alpha = 20°$ for the D2R10 profile.

Prism cells are generated near the wall of the foil to resolve flow in the boundary layers, as shown in Figure 8(d). The absolute total thickness of the prism layer is 0.5 m, and the number of prism layers is 55 for all simulation cases. Since the crescent-shaped profile has large camber, a strong flow separation phenomenon is expected. Therefore, it is desirable for the y^+ of the first-layer cells near the wall to be less than 1 to have a more detailed and accurate study of the boundary layer flow. In the simulation cases, the order of the magnitude of y^+ is around 10^{-1} on most areas of the wall. To obtain this low y^+ value, the near-wall thickness of the prism layer is set as the absolute value of 1×10^{-5} m, which does not change during global mesh refinement.

Under the deep-stall conditions, the von Kármán vortex street is expected to spread for a long distance in the downstream region, so extra downstream refinement of the downstream region is introduced when $\alpha \geq 40°$, as can be seen in Figure 9.

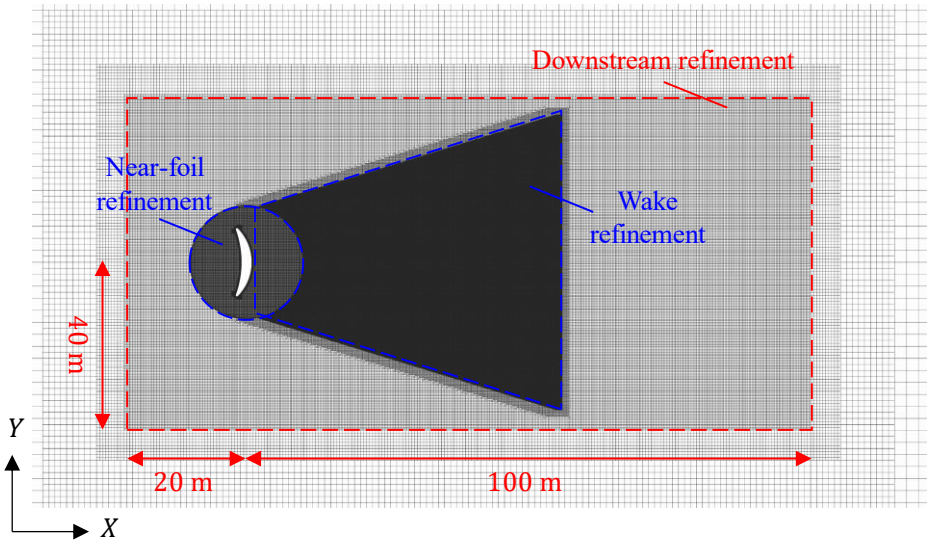

Figure 9. Two-dimensional trimmed mesh for the deep-stall conditions ($\alpha = 90°$).

Two-dimensional mesh independence studies are conducted from two perspectives: the refinement strategy and the size of cells. For the refinement strategy, three factors, including the existence of near-foil refinement and the length and separate angle of the wake refinement, are studied to exclude any influences from the mesh. As a result, the mesh follows the strategy of having wake refinement with 0.3 rad at a separate angle and a length of 60 m, as well as near-foil refinement.

By following the certain refinement strategy, several two-dimensional simulations with different base sizes are performed. Variations in base size influence the entire mesh, except for the prism layer mesh, in the normal direction. Then, a series of three-dimensional mesh is generated based on the same refinement strategy.

2.2.3 Viscous regimes

To solve the high-Re problem, turbulence models need to be incorporated. In Paper I, a CFD model based on the uRANS method is developed, and the time-averaged loading conditions are well-solved since the boundary layer flow is resolved with a finely layered mesh. However, significant flow separation is found, leading to significant unsteady characteristics in the flow field. When studying the propulsive performance of a single sail, it is enough to only consider the time-averaged loads. However, unsteady characteristics should be considered when analyzing structural response. For example, a low-frequency oscillation of the external loads may cause a vortex-induced vibration of the whole sail, while a high-frequency oscillation may cause local vibrations on the shell panels, resulting in buckling. To simulate separating flow more accurately, the large eddy simulation (LES) method (Smagorinsky, 1963) needs to be introduced since all turbulent scales are modeled in uRANS, while only small, isotropic turbulent scales are modeled in LES (Davidson, 2019; Yao et al., 2008). By applying the LES method, both time-averaged properties and unsteady characteristics can be determined. On the other hand, the LES method imposes costly near-wall meshing requirements. To avoid these

and keep the boundary layer flow well-resolved, the detached eddy simulation (DES) method, which combines uRANS and LES, is selected in this thesis. The k–ω SST model (Menter, 1993) is applied for both the uRANS and IDDES (Shur et al., 2008) simulations.

Take the fully expanded condition with $\alpha = 23°$ as an example. Figure 10 shows the distribution of regions calculated using the uRANS and LES methods. Most areas, especially the boundary flow regions, are calculated using the uRANS method, while the LES regions are mainly distributed in the downstream field. Due to the impact of the tip vortices, fewer areas are calculated by LES when approaching the tip (see Figure 10(a)).

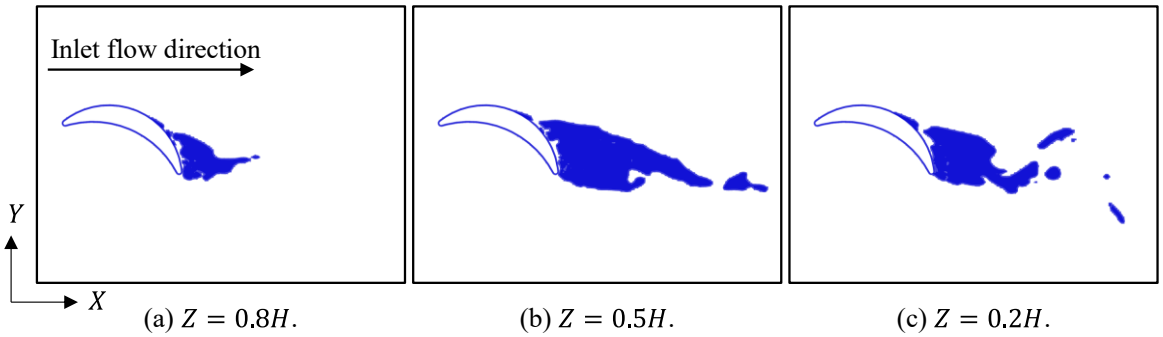

Figure 10. Distribution of the DES upwind blending factor at different spanwise positions, with a fully expanded condition of $\alpha = 23°$. Blue marks out the regions calculated with LES, while the remainder of the computation domain is calculated using uRANS.

The approach of blended wall treatment is applied to the RANS equations (Wilcox, 1989). This approach has the advantage of treating complex geometries with local flow characteristics. Since the velocity over complex walls varies widely, and the geometry of the wingsail profile has a curvature, it is difficult to ensure that y^+ in all cells adjacent to the walls are either above a high value or below a low value, which is required in a conventional wall treatment model. Contrastingly, blended wall treatment is considered a function of local y^+. Blended wall laws are employed to model smooth variable changes in the buffer layer between the viscous sublayer and the logarithmic region.

2.2.4 Solver and schemes

The CFD model is important in this thesis because there is a lack of research on wingsails with such a cambered profile. Hence, this thesis aims to establish and develop a high-fidelity CFD model for resolving the flow field that the wingsail with a crescent-shaped profile induces.

The finite volume method (FVM) is utilized to discretize the governing equations. This method employs a segregated flow solver that is accomplished with the semi-implicit method for pressure-linked equations (SIMPLE) algorithm (Patankar, 1980). It is worth noting that the flow is assumed to be incompressible in this thesis because of the low freestream Mach number.

The convection fluxes on cell faces are discretized by means of a hybrid second-order upwind and bounded-central scheme. The diffusion fluxes on both the internal and boundary cell faces

are discretized with a second-order scheme. The second-order hybrid Gauss-LSQ method is used in gradient computation, which involves the reconstruction of field values in a cell face, such as the secondary gradients of the diffusion fluxes and pressure gradients, as well as the rate-of-strain tensors used in the turbulence models. A second-order implicit method is utilized to discretize the time derivative, while the Reichardt law (Reichardt, 1951) is utilized for the momentum equations.

The gamma transition model (Menter et al., 2015), which solves for turbulence intermittency to predict the onset of transition in the turbulence boundary layer, is also introduced to exclude the influence of transition flow. According to the results, the transition model mainly influences turbulence on the pressure side. It is found that the influence of the transition flow on propulsive performance can be ignored. Further, having the transition model significantly slows down the simulation speed since an extra equation needs to be solved, so the transition model is not applied in this thesis.

2.3 Structural analysis

2.3.1 Finite element analysis model

For the fully expanded wingsail, structure analysis is based on the apparent wind having $V_{AW} = 16\ \mathrm{m/s}$. According to the CFD results from Paper II, C_L is 2.10. The external load applied on the wingsail is divided into two parts: the pressure force on the pressure side and the suction force on the suction side, both of which are assumed to be uniformly distributed across the surface of the wingsail. Based on the CFD results, the magnitude of the total force on the suction side is approximately twice that on the pressure side.

For the boundary condition, the bottom of the mast, where it is fixed to the deck of the ship, is a fixed boundary, so no translation or rotation is allowed.

For the concept utilizing a cubic mast, each pair of sub-parts that contact each other is tied together at the contact surface to ensure that there is no relative motion between them. The panels can have small relative tangential displacement in the vertical direction because the panels do not need to bear global bending.

Quasistatic FEA is used to predict and evaluate the structural response. The commercial software ABAQUS (Dassault Systemes, 2020) is used to perform the FEA simulations. The analysis product is ABAQUS/Standard. The geometrical nonlinearities are considered in ABAQUS using the NLGEOM option, which considers large deformations and displacements but not large rotations.

The structure of the wingsail is considered a group of shell elements in the FEA simulations. Five thickness integration points are set, and Simpson's Rule is applied for integration.

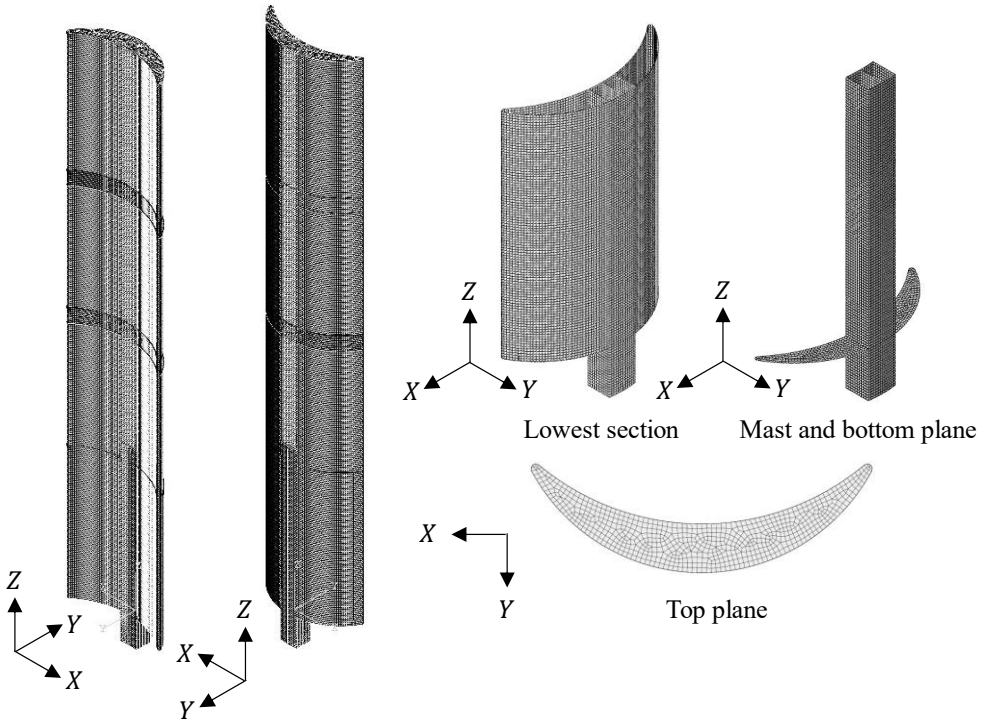

Figure 11. The numerical mesh of the concept utilizing a cubic mast.

A set of quad-dominated mesh is applied to the FEA model, as shown in Figure 11. The quadrilateral mesh elements are assigned the S4R element type, while the triangular mesh elements, which are mainly distributed on the horizontal section plates, are assigned the S3 element type. The typical element size is 0.2 m, selected based on mesh independence studies. According to the stress distribution, more refined mesh is applied to the edges. Since the section profile of the wingsail has some arcs and circles, curvature control is applied to the mesh generator. The maximum deviation factor is set to 0.1 so that the approximate number of elements per circle at the edges of the crescent-shaped profile is 8.

The gravity of the wingsail structure, i.e., the inertia loads from the self-weight, is ignored since it does not have a noticeable influence on stress distribution.

2.3.2 Evaluation criteria

In this thesis, three properties of each structure are evaluated: its weight, strength, and rigidity. Since there is no guidance for this crescent-shaped structure, the authors of Paper III formulate a series of conservative criteria:

- The total weight of the wingsail must be as low as possible.
- The maximum von Mises stress (σ_{Mises}) should not exceed the yield stress. Including a factor of safety of 2, the allowable von Mises stress for steel (S275) (ASTM, 2004) is 140 MPa, while the allowable stress for aluminum (6061-T4) (BS EN, 2004) is 105 MPa. The maximum normal stress in compression should not exceed the buckling stress. The maximum shear stress should be less than 50% of the allowable von Mises stress; that is,

the allowable shear stress is 70 MPa for steel and 53 MPa for aluminum.

- Rigidity or flexibility is also relevant because if the structure is not rigid enough, the telescopic function will not work. The maximum deflection, which usually occurs at the tip, should not be larger than 5% of the fully expanded height. In the fully expanded state, the maximum allowable tip deflection is 3.7 m. The relative displacement of the panels should not exceed half of the mast diameter (i.e., 1 m).

Because only quasistatic condition is considered in the present study, while the inertia loads from dynamic forces, wind gusts and other loads are ignored, these criteria listed above are set to be stricter than those recommended by DNV (DNV, 2022).

2.4 Fuel saving evaluation

Predicting the performance of a WASP system requires the inclusion of the full system, i.e., the sails and the ship, especially due to the F_S that the sails create. The F_S and yaw moments that WASP systems introduce must be compensated for by a drift of the ship and the rudder angle, both of which introduce an added resistance that causes both a lower net thrust (i.e., the thrust of the sail minus the added resistance caused by the sail) and the need for sail trim optimization to achieve the best performance and respect any given constraints on the rudder or heel angle, for instance. Therefore, a model respecting at least four degrees of freedom, i.e., surge, drift, yaw, and heel, must be used. Further, the performance of a WASP system also depends on the ship upon which it is installed, which means that any performance or comparison study must incorporate a case study ship. In this thesis, a tanker with a deadweight of approximately 100,000 tons is used. The sail is positioned 5 m behind the forward perpendicular, at the centerline of the ship.

ShipCLEAN, a generic model developed to provide accurate predictions with little input data that respects the minimum four degrees of freedom, is used as a performance prediction tool in this thesis. Polar plots for fuel saving are first created for different wind strengths and true wind angles. Then, to predict long-term fuel savings, the automatic identification system (AIS) data of the ship are used to derive the position and speed of the ship during 2018. Environmental conditions are retrieved from the Copernicus Marine Environment Monitoring Service (CMEMS) and are updated every 3 hours. Detailed information of the route and weather conditions of the case study can be found in Paper I.

3 Results

This chapter presents a summary of the results of the appended papers. It highlights the main achievements of and presents a selection of important results from the papers.

3.1 Summary of Paper I

Paper I introduces the concept design of a telescopic wingsail with a new crescent-shaped profile. To evaluate its performance, two- and three-dimensional CFD simulations with uRANS and the k–ω SST turbulence model are used. One objective of the study in Paper I is to address suitable sail configurations with an advantageous C_L to maximize F_T for large sailing merchant ships and their ship operation profiles. Paper I compares the propulsive performance of two rigid wingsails with different sectional profiles (NACA 0015 and crescent-shaped). The analysis also focuses on exploring flow field properties, including flow separation points and tip vortices, as well as the impacts of external loading conditions on the wingsails. A case study in which the new sail is applied to a fossil fuel-free ship is included, and the ship modeling platform, ShipCLEAN, is used to evaluate its propulsive performance.

3.1.1 Force coefficients

Based on the results of Paper I, which are derived from a comparison of the two- and three-dimensional simulations with a periodic top and bottom, the differences for the crescent-shaped foil, D2R10, are 7.5% for C_L and 58.1% for C_D, as Figure 12 presents. Therefore, two-dimensional simulations significantly overestimate force coefficients, even under low α conditions, and C_D is more sensitive than C_L. In the two-dimensional simulations, due to the limitation of spanwise flow, the vortices are constrained and not well-developed (Park et al., 2017). An overestimation of force coefficients, especially C_D, was also found in similar research performing high-Reynolds-number CFD simulations for airfoils with strong flow separation (Zhu, 2020). Comparing the results from the different boundary conditions, these two cases provide force coefficients with obvious differences, indicating that the tip vortices, which are discussed in Section 3.2, have significant impacts. Specifically, when there is a freestream tip, the lift force on the foil decreases by 5.7%, and the drag force increases by 35.0%.

As Figure 12 shows, the crescent-shaped profile, D2R10, has significantly higher force coefficients and is expected to provide better propulsive performance. Furthermore, the impacts of tip vortices on the crescent-shaped concept are not as significant as those on the NACA 0015 wingsail. On the other hand, because of flow separation, the crescent-shaped wingsail shows a remarkable oscillation amplitude with the force coefficients. Therefore, the crescent-shaped sail may suffer from more serious flutter, which makes higher requirements on the structure of the sails.

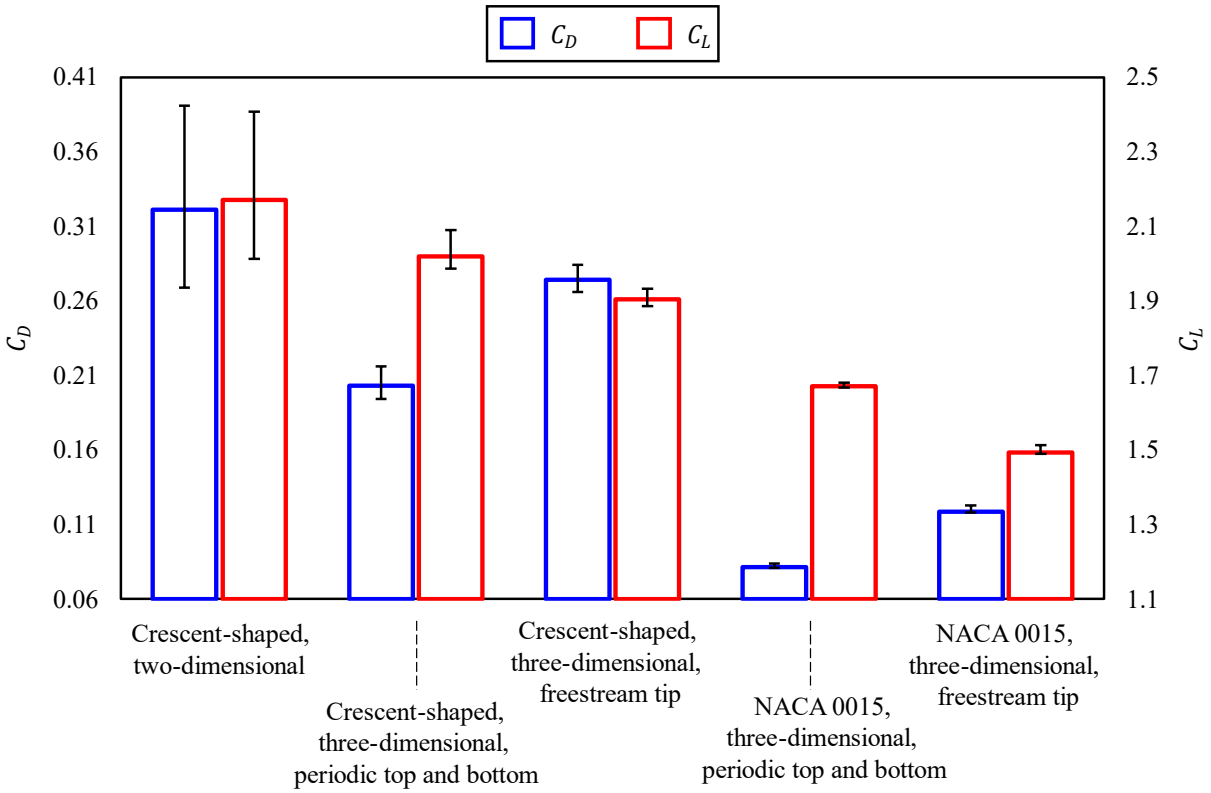

Figure 12. The force coefficients of the NACA 0015 and D2R10 crescent-shaped foils from the two- and three-dimensional simulations with different boundary conditions. The error bars represent the amplitude of oscillation.

The plots of the force coefficients within a wider range of α can be found in Figure 13, with the blue lines and symbols representing the two-dimensional results and the red lines and symbols representing the three-dimensional results. In Figure 13(a), it can be seen that there is no clear α_c for this type of profile, and two peaks of C_L occur when $\alpha = 20°$ and $\alpha = 35°$. The highest C_L is approximately 2.7 when $\alpha = 35°$ based on the two-dimensional simulations and 1.9 when $\alpha = 20°$ based on the three-dimensional simulations. As for C_D, as shown in Figure 13(b), both the two-dimensional and three-dimensional simulations show that when $\alpha \leq 80°$, C_D increases as α increases. The two-dimensional simulations also predict much higher C_D than the three-dimensional simulations, and other researchers have detected a similar phenomenon (Najjar & Vanka, 1995). According to the two-dimensional simulations, the highest C_D is around 3.7 when $\alpha = 80°$. For the high-Re conditions, C_D for a flat plate is approximately 1.98, and for a semicircle opening upstream, it is approximately 2.30 (Hoerner, 1976). The C_D of the crescent-shaped profile should probably be between these. Additionally, due to the tip vortices, C_D is expected to be even lower, so the predicted C_D is unreasonably high. In addition, C_D suddenly decreases when α increases from 80° to 90° in two-dimensional simulations. As the findings from the two-dimensional simulations do not agree with the basic physics that are addressed in the three-dimensional simulations, it is believed that the two-dimensional simulations cannot provide reasonable predictions of the force coefficients when $\alpha > 20°$ due to the strong flow separation, which is explained in Section 3.2.

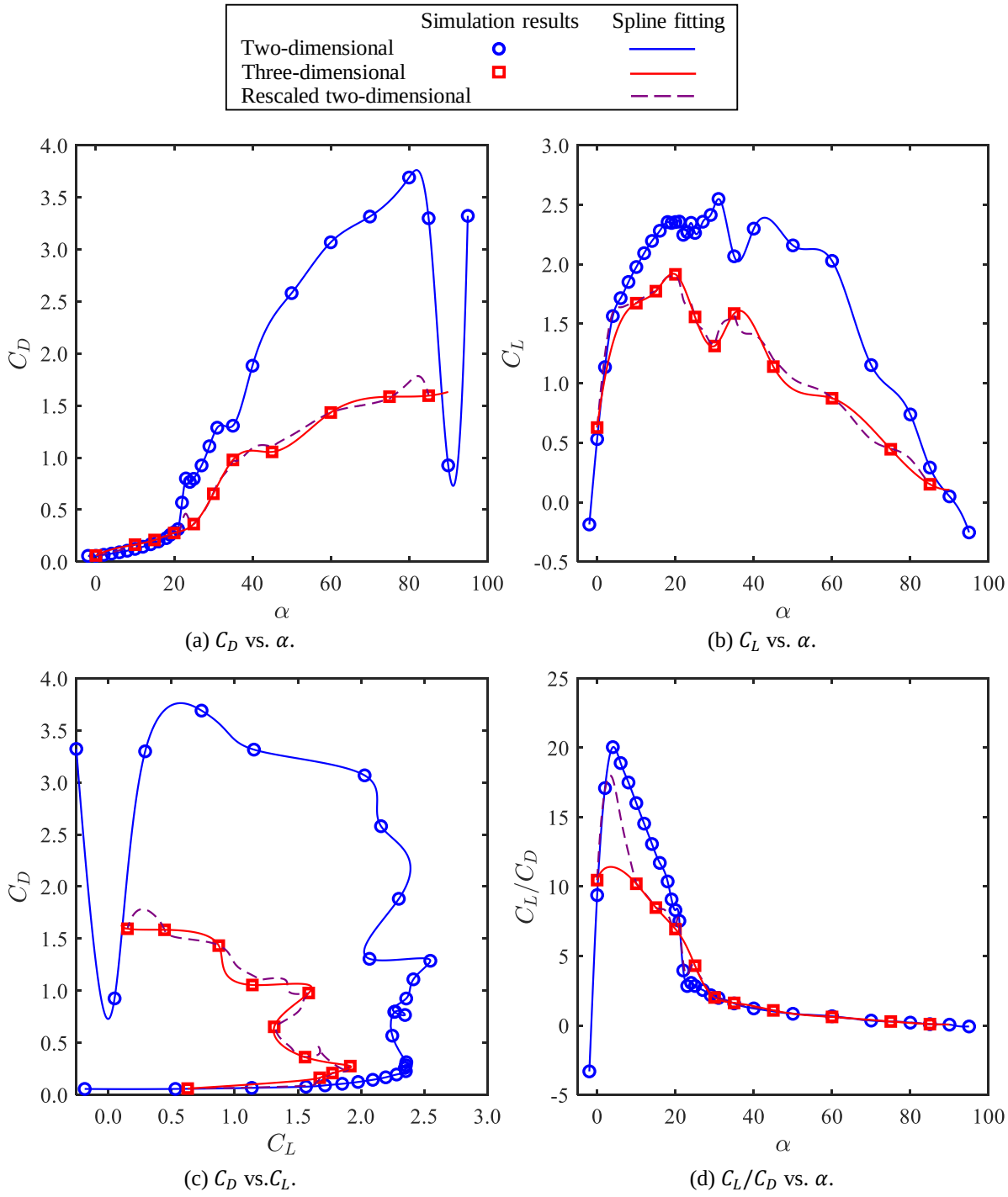

(a) C_D vs. α.

(b) C_L vs. α.

(c) C_D vs.C_L.

(d) C_L/C_D vs. α.

Figure 13. Time-averaged C_L and C_D curves.

However, the assumption that the two-dimensional simulations correctly show the trend of the force coefficients is still held. Based on this assumption, a hybrid two- and three-dimensional simulation method is proposed. First, a series of two-dimensional simulation cases with various α are performed to get the time-averaged force coefficients. Second, a limited number of three-dimensional simulations with distinctive α, e.g., α that have a peak or valley force coefficient value, are performed. Third, the ratio of C_L and C_D between the two- and three-dimensional simulations is calculated. Finally, C_L and C_D are rescaled based on this ratio. In this way, the

computational capacity can be reduced because the three-dimensional simulations are much heavier than the two-dimensional simulations. In Figure 13, the purple dashed line represents the rescaled two-dimensional results. From Figure 13(a) and Figure 13(b), it can be seen that the rescaled two-dimensional results are closer to the three-dimensional results, so the rescaling method is feasible.

3.1.2 Propulsive performance

Based on the force coefficients from the CFD simulations with the freestream tip setup, propulsive performance is executed with the assumption that the force coefficients will remain the same when the apparent wind speed changes following the direction of navigation since the force coefficients are believed to be less sensitive to Re.

Notably, when the point of sail is luffing, close-hauled, or beam reach, i.e., θ_{AW} is from 30° to around 90°, F_L is the main source of thrust. However, under other conditions, the wingsail may be operated to use F_D. Therefore, to predict the propulsive performance for all the directions of apparent wind, an enumeration method is used to ensure that C_T with θ_{AW} is in the 0° to 180° range and α is in the 0° to 90° range. The results for the level of propulsion (the highest C_T at different θ_{AW}) and how the wingsail is operated (α that is applied to get the highest C_T) are plotted in Figure 14. Since the polar diagram is always symmetric, only half of the polar plot, i.e., $0° \leq \theta_{AW} \leq 180°$, is presented.

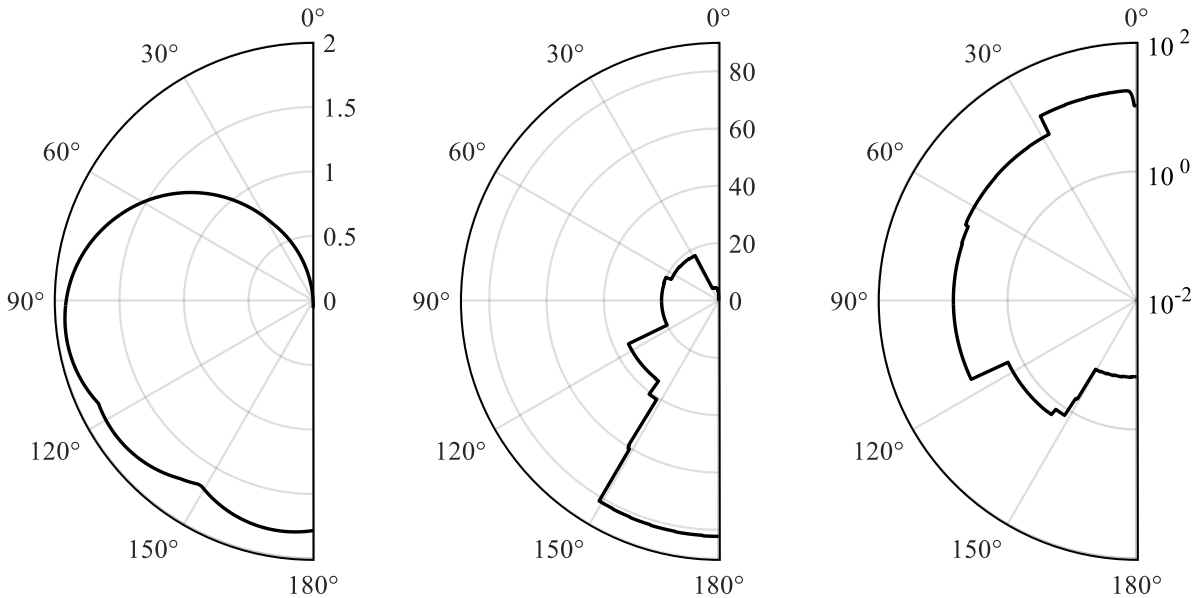

(a) C_T vs. θ_{AW}. (b) α vs. θ_{AW}. (c) C_L/C_D vs. θ_{AW}.

Figure 14. Polar diagram of C_T, α, and L/D versus θ_{AW} for the crescent-shaped profile at $V_{AW} = 25$ m/s.

When the ship is navigating against the wind, i.e., the luffing point of sail, C_T is rather low or even less than 0. Here, the wingsail is operated with a very low α to reduce the extra resistance. As θ_{AW} increases, e.g., to $\theta_{AW} = 60°$, C_T increases, and the wingsail is operated with α_c to

have the maximum C_L. For θ_{AW} in the 60° to 180° range, the wingsail can provide notable propulsion. However, the wingsail is not operated in the same way. For instance, when $30° < \theta_{AW} < 120°$, α should be around 20° to get the maximum C_L, and F_L is the main source of thrust. When $120° < \theta_{AW} < 150°$, i.e., the point of sail is board reach, the optimum α is around 40° with $C_L \approx C_D$, and the wingsail uses both F_D and F_L for propulsion. When the point of sail is running, which means θ_{AW} is around 180°, F_D is mainly used, and the wingsail is operated with $\alpha \approx 80°$.

The polar diagram is applied to the inhouse program, ShipCLEAN (Tillig & Ringsberg, 2019). Figure 15 presents a polar plot of the fuel savings for the case study tanker with one crescent sail in 10 kn and 20 kn of wind.

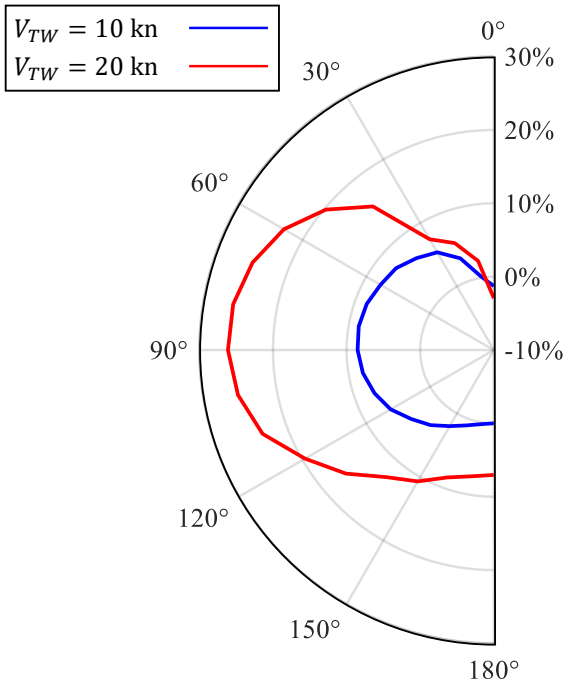

Figure 15. Polar plot of relative fuel consumption savings vs. θ_{TW} at two V_{TW}.

The polar plot shows that a maximum fuel saving of about 9% at $\theta_{TW} = 90°$ in $V_{TW} = 10$ kn, and 25% in $\theta_{TW} = 90°$ in $V_{TW} = 20$ kn can be expected. However, the fuel savings vary over the true wind angle; thus, the performance must be predicted using actual routes with realistic weather, as presented in the following section.

As a result of long-term fuel savings, total savings of 9.5% are achieved with the crescent sail. For comparison purposes, the simulations are repeated with a Flettner rotor (5 m in diameter and 30 m in height) positioned similarly. The Flettner rotor has resulted in 9.8% savings on the same route. About 34% of the time the fuel savings are larger than 5%. The maximum additional fuel consumption is less than 1%. The maximum fuel saving is 97.5%. See Paper I for more detailed results.

3.1.3 Flow field characteristics

The flow field that the crescent-shaped profile induces has a remarkable flow separation phenomenon at the suction side close to the trailing edge, which results in unsteady characteristics.

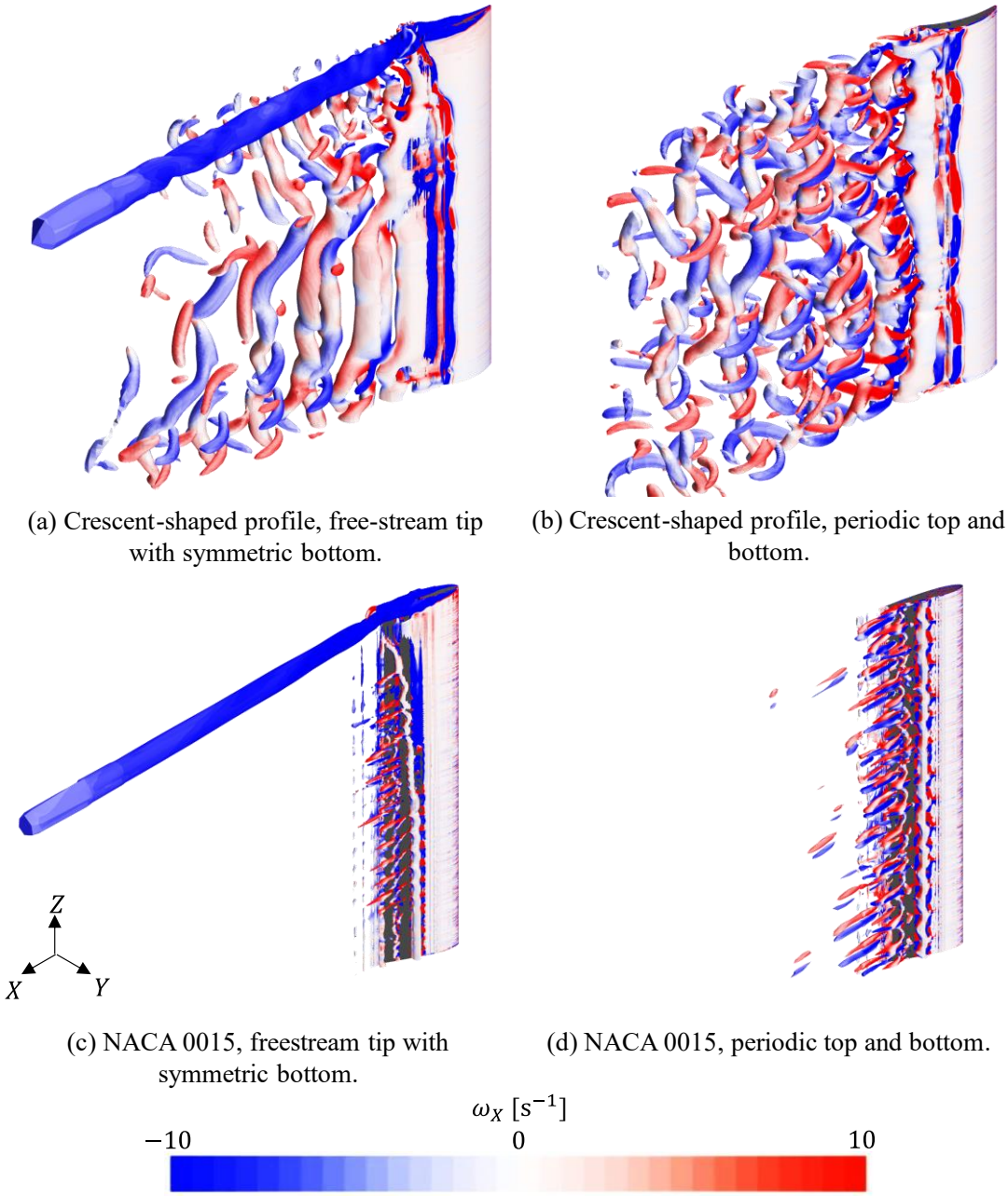

(a) Crescent-shaped profile, free-stream tip with symmetric bottom.

(b) Crescent-shaped profile, periodic top and bottom.

(c) NACA 0015, freestream tip with symmetric bottom.

(d) NACA 0015, periodic top and bottom.

Figure 16. The iso-surfaces of $Q = 5\ \mathrm{s}^{-2}$, colored with ω_X. $\alpha = 20°$ for the crescent-shaped profile and $\alpha = 16°$ for NACA 0015. The inlet flow velocity is in the positive X direction.

For the NACA 0015, there is usually no or one flow separation point depending on the α. The characteristic of flow separation does not appear if α is lower than the critical angle of attack. However, when looking at the flow field that the crescent-shaped foil generated, flow separation always occurs. From the iso-surface plot in Figure 16, where the colorful contours represent the

streamwise vorticity, the circular patterns of rotating air left behind the tip of the foil, which are the tip vortices, can be easily recognized (see Figure 16(a) and Figure 16(c)). Tip vortices cause a reduction in C_L. Wingsails with different section profiles also show different wake characteristics. For the crescent-shaped profile, vortex shedding is much more significant. As shown in Figure 16(a) and Figure 16(b), numerous vortex tubes can be seen in the wake region. However, for the NACA 0015 profile (see Figure 16(c) and Figure 16(d)), only limited vortex tubes can be seen developing on the suction side. The oscillation in force coefficients of the crescent-shaped wingsail is much stronger than those of the wingsail with the NACA 0015 profile.

The characteristics of the flow field that the crescent-shaped wingsail induces are more deeply examined and discussed in Paper II.

3.2 Summary of Paper II

In Paper II, full-scale simulations, utilizing both the uRANS and IDDES methods, are performed to analyze the flow field around a wingsail. The paper's analysis includes flow separation and vortex shedding, the development and dissipation of wake vortices, and lift reduction due to tip vortices. It also studies the telescopic function of the wingsail by analyzing sails with different heights and under different wind conditions. The paper concludes that the uRANS and IDDES simulations make similar predictions for time-averaged loads but disagree on the unsteady characteristics of the flow field. The IDDES simulations also indicate more complex vortex shedding phenomena.

3.2.1 Flow separation

The flow field that the crescent-shaped profile induces has a remarkable flow separation phenomenon at the suction side close to the trailing edge, resulting in unsteady characteristics. To reduce the influence of the tip vortices, analysis of the flow separation and vortex shedding is based on the fully expanded condition. For a clearer presentation and discussion of the flow separation phenomenon, the simulation case with the largest α, i.e., $\alpha = 23°$, is taken as an example. Figure 17, which presents streamwise velocity distribution and the streamline at the sectional plane with different spanwise positions, shows that the results from the uRANS and IDDES methods share some similarities. For upstream areas of the half chord, i.e., on the left of the half chord in the sub-figures of Figure 17, the flow is resolved by applying the k–ω SST turbulence model when using both the uRANS and IDDES methods. Therefore, the characteristics of the flow field that the two methods predict are almost the same. There is a high-velocity region where the streamwise velocity is approximately twice the inlet flow velocity on the suction side upward of the half chord, which causes a reduction in pressure and finally leads to lift force. There is also a pronounced low-velocity region on the suction side of the profile that extends to the downstream areas. The observed phenomena support the hypothesis that the IDDES method provides more detailed information on separating flow since eddies smaller than the integral scale but larger than sub-grid scales are directly resolved instead of being modeled (H. Yao et al., 2018).

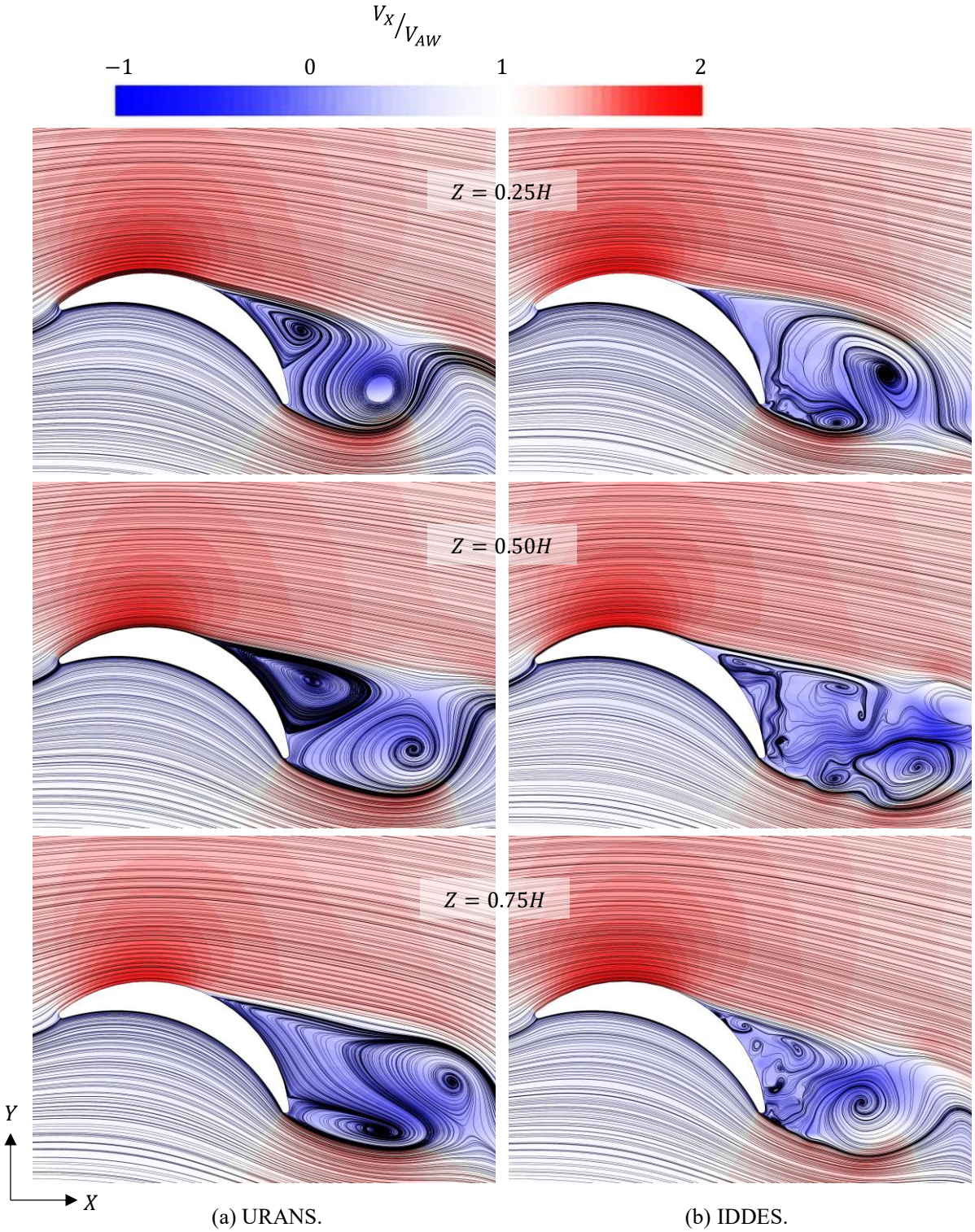

(a) URANS. (b) IDDES.

Figure 17. V_X distribution and streamlines at different spanwise sections under the fully expanded condition of $V_{AW} = 8$ m/s, $\alpha = 23°$.

As shown in Figure 10, the low-velocity region is mainly calculated using a LES when applying the IDDES method. Therefore, the flow field in this area is different for the two methods. The results from the uRANS method show two main vortices (see Figure 17(a)). At the lower part of the sail, e.g., $Z = 0.25H$, the IDDES results also show the main vortices because the bottom

panel with the symmetric boundary condition constrains vortex development in the spanwise direction. However, at the higher part of the sail, e.g., $Z = 0.50H$ and $Z = 0.75H$, the flow shows more complex characteristics according to the IDDES results (see Figure 17(b)).

Periodic oscillations are evident from the time history of the C_L values in the uRANS simulations. Contrastingly, the oscillations are quite random, without a clear period, in the IDDES simulations. Referring to the FSI simulations in Paper II, these irregular oscillations explain the high-frequency damping found in the IDDES results.

Therefore, to study the unsteady properties of force coefficients, fast Fourier transform (FFT) analysis is conducted. Figure 18 presents the FFT analysis results for C_L under the fully expanded condition. The length of physical time of the selected data is 10 s, so the first peak with a frequency of 0.1 Hz is spurious and can be ignored. When looking at the dashed lines, a second set of peaks is evident, with frequencies around 0.4 Hz, so the uRANS simulations indicate that C_L has a clear oscillating period of 2.5 s and an amplitude of approximately 0.02. The C_L values that the IDDES simulations predict do not show periodic oscillations. In Figure 18(b), in which the FFT plot is zoomed in on the low-frequency region, the second set of solid-line peaks is unclear. Some small oscillations can also be found in the solid lines in the high-frequency region of the FFT results, shown in Figure 18(c). The time history and FFT results of C_D and C_M, as well as those under the fully retracted condition, show similar characteristics.

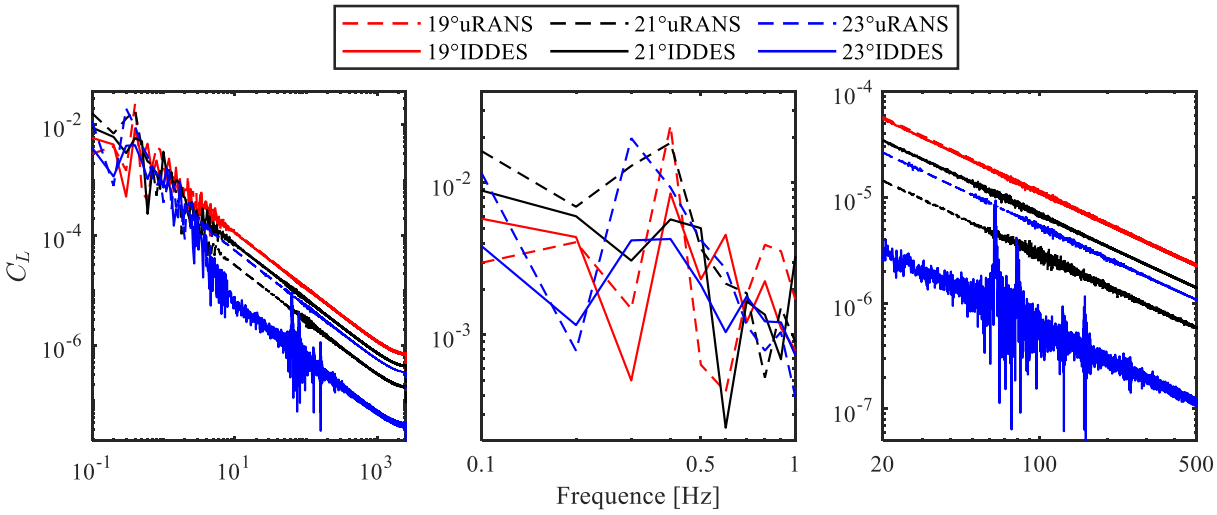

(a) All frequency range. (b) Low frequency range. (c) High frequency range.

Figure 18. FFT results of C_L, fully expanded condition.

3.2.2 Wake flow

Normally, more than one wingsail is installed and operated on a ship. Analysis of the wake flow is expected to provide some guidance for future studies on ships with multiple sails. The wake flow that the two methods resolve shows many differences. Taking the results under the fully expanded condition as examples, the IDDES simulations predict a flow field with much more complex vortex structures. From the uRANS simulations, the spanwise vortex tubes can be

easily observed, so the vortex shedding phenomena do not show significant spanwise characteristics, except for the tip vortices. However, the vortices have numerous streamwise and crossflow structures when applying the IDDES method.

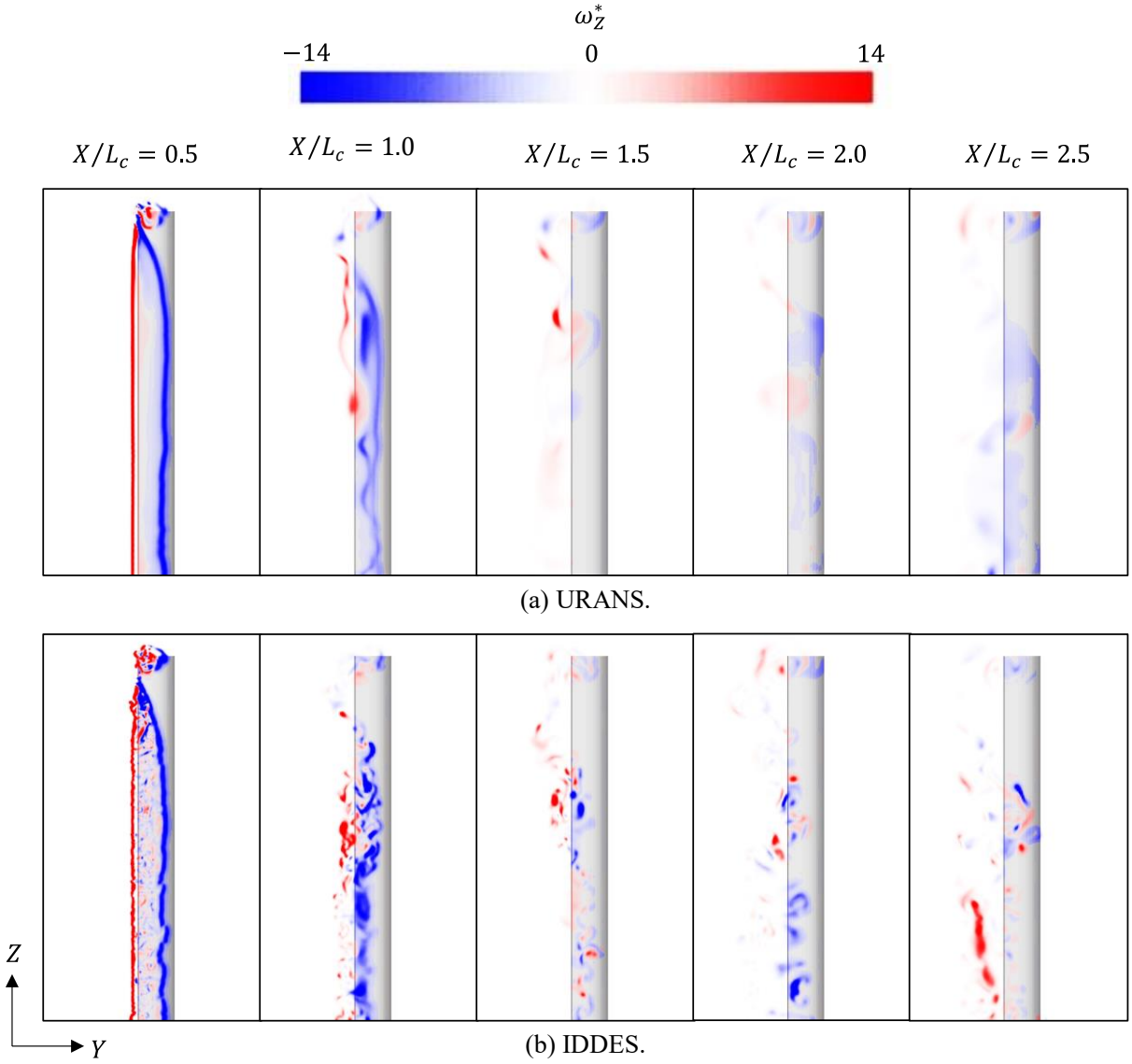

(a) URANS.

(b) IDDES.

Figure 19. Non-dimensional ω_Z distribution at different streamwise positions in the wake field under the fully expanded condition of $V_{AW} = 8$ m/s, $\alpha = 23°$. The inlet flow orients in the direction perpendicular to the paper/screen, pointing outwards.

When looking at the ω_Z distribution at section planes with different streamwise positions, as shown in Figure 19, the differences between the results that the two methods simulate are more apparent. The uRANS results show some vertical vortex tubes. For example, in Figure 19(a), when $X/L_C = 0.5$, i.e., it is just behind the trailing edge, a strong vortex tube can be found. However, when using the IDDES method (see Figure 19(b)), there are small vortices on the decimeter scale at the section plane of $X/L_C = 0.5$. When looking at the position $X/L_C = 1.0$, the distribution of ω_Z is preserved, as shown in Figure 19(a), while for the IDDES results, it

can only be found in the lower part close to the bottom panel. Moreover, the vortices dissipate quickly in the wake region when applying the uRANS method, which indicates that there is more energy loss. The turbulent kinematic energy in the wake region is also much lower when applying the IDDES method. When looking at the streamwise position of $X/L_C = 2.0$, the vortices that the IDDES method predicts are still noticeable, while those that the uRANS method predicts are almost dissipated.

3.2.3 Tip vortices

Another important characteristic of the flow field is the phenomenon of tip vortices, which is believed to be the main reason for lift reduction when changing the boundary conditions from periodic top and bottom to free tip and symmetric bottom. Notably, when the top and bottom have periodic boundary conditions, the pressure distribution along the foil is similar at the different Z positions. However, if the boundary condition is a free tip and symmetric bottom, the pressure difference between the pressure and suction sides becomes smaller when approaching the tip of the wingsail, leading to lift reduction.

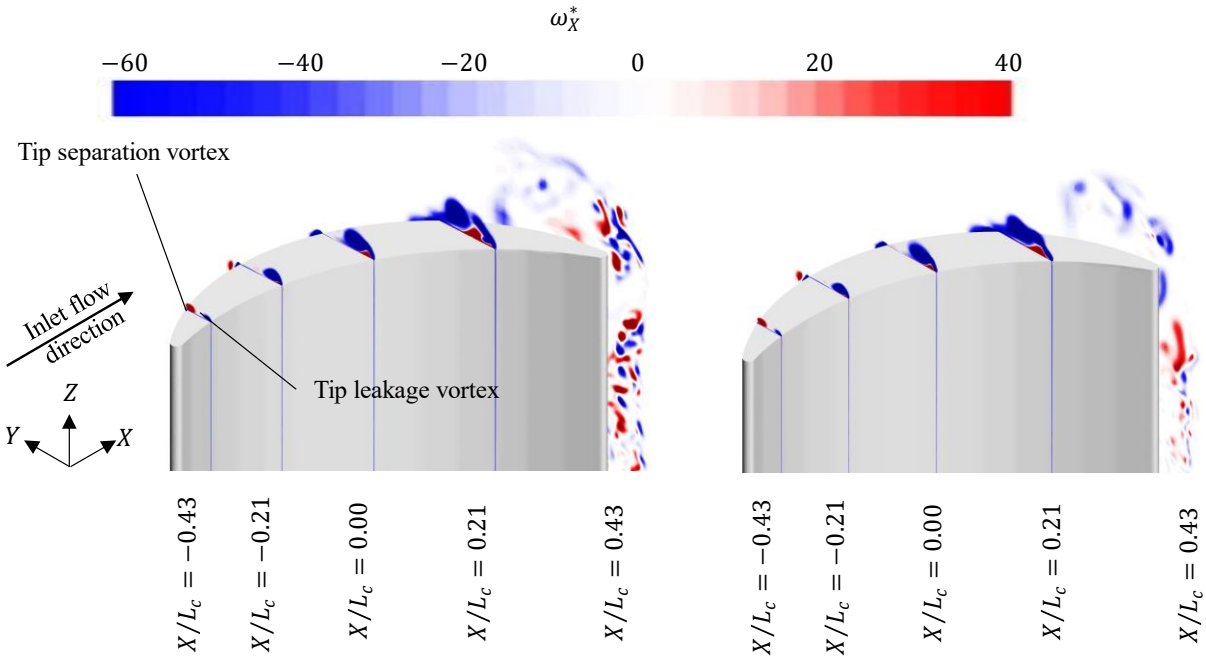

(a) Fully expanded condition. (b) Fully retracted condition.

Figure 20. The non-dimensional ω_X distribution at different streamwise positions around the tip, based on the IDDES simulations, $\alpha = 23°$. For the fully expanded condition, $V_{AW} = 8$ m/s, while for the fully retracted condition, $V_{AW} = 32$ m/s.

By plotting ω_X^* at several different streamwise positions around the tip (Figure 20), two tip vortices, the tip separation vortex and the tip leakage vortex, develop at the suction and pressure sides, respectively. According to the uRANS simulations, the two vortices combine at around the half chord into a single vortex with a more complex internal flow structure. Nevertheless, in the IDDES results, the two vortices do not combine. The tip leakage vortex is also much

stronger than the tip separation vortex, which dissipates quickly at around the half chord. Due to the higher apparent wind speed, the tip vortices are stronger under the fully retracted condition. However, when comparing the dimensionless value of ω_X, the distribution is similar between the two conditions.

It is believed that tip vortices have notable negative effects on propulsive performance. That is, the pressure on the pressure side is lower when it is close to the tip, leading to a reduction in lift force. Therefore, some actions are suggested to release the phenomenon of tip vortices, e.g., a top-mounted disk installed on the tip would likely improve propulsive performance.

3.3 Summary of Paper III

In Paper III, quasistatic FEA is performed to study the structural responses of a crescent-shaped wingsail rig. A few conceptual designs of telescopic rigs, including different structural designs and material arrangements, are analyzed and compared by considering three criteria: rigidity, strength, and weight. The external wind loads applied to the sails in the structure analysis are obtained from the aerodynamic simulations performed in Paper II. The advantages and disadvantages of each concept are discussed, aiming to provide a good strategy for the structural design and arrangement of WASP systems. The results of the study can also be used in future work as a basis for structural optimization and FSI analysis.

3.3.1 Thickness and weight

A series of FEA simulations are performed to determine the thickness of different parts of the structure. The thicknesses of the different parts are then adjusted several times to satisfy the strength requirement and minimize the weight.

Table 2. Weight, maximum von Mises stress, and maximum deflection of different structural designs.

		Concept utilizing vertical stiffeners	Concept utilizing a cubic mast	
			Steel frame, aluminum panels	All in aluminum
Total weight	[t]	130	116	74
Weight excluding the panels	[t]		75	33
Max. von Mises stress	[MPa]	158 [a]	141 [b]	103 [b]
Max. deflection	[m]	0.32	0.59	1.14

[a] The Max. σ_{Mises} happens at horizontal section plate of section 2, close to the edges (see Figure 21).
[b] The Max. σ_{Mises} happens at bottom plate, close to the mast (see Figure 22).

By comparing the two concepts, the total weight can be reduced by approximately 11% by dividing the wingsail structure into a strong frame and light panels (see Table 2). For the all-aluminum concept utilizing a cubic mast, the weight can be significantly reduced, but this

results in a much larger tip displacement. Therefore, the “steel frame and aluminum panels” design shows better rigidity, while the “all in aluminum” design is lighter.

3.3.2 Strength

In the concept utilizing vertical stiffeners, at the section plate of section 2 approaching the edges, stress concentration is found, although web structures have been added to avoid stress concentration at the bottom. However, for the remaining parts of the wingsail, the von Mises stress (σ_{Mises}) is much lower than the threshold value, as shown in Figure 21, so there is no need to continue adjusting the thickness.

In Figure 21 and Figure 22, the counterplots follow the visualization rule that if the values for elements are within 75% of each other, they will be averaged and then displayed.

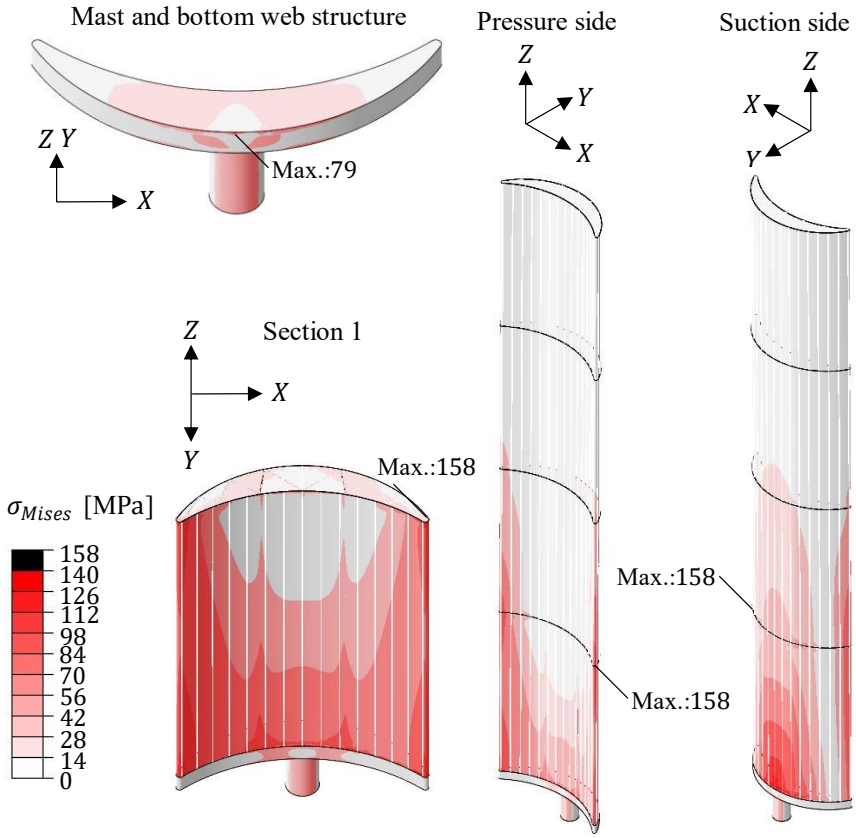

Figure 21. Von Mises stress distribution for the concept utilizing vertical stiffeners.

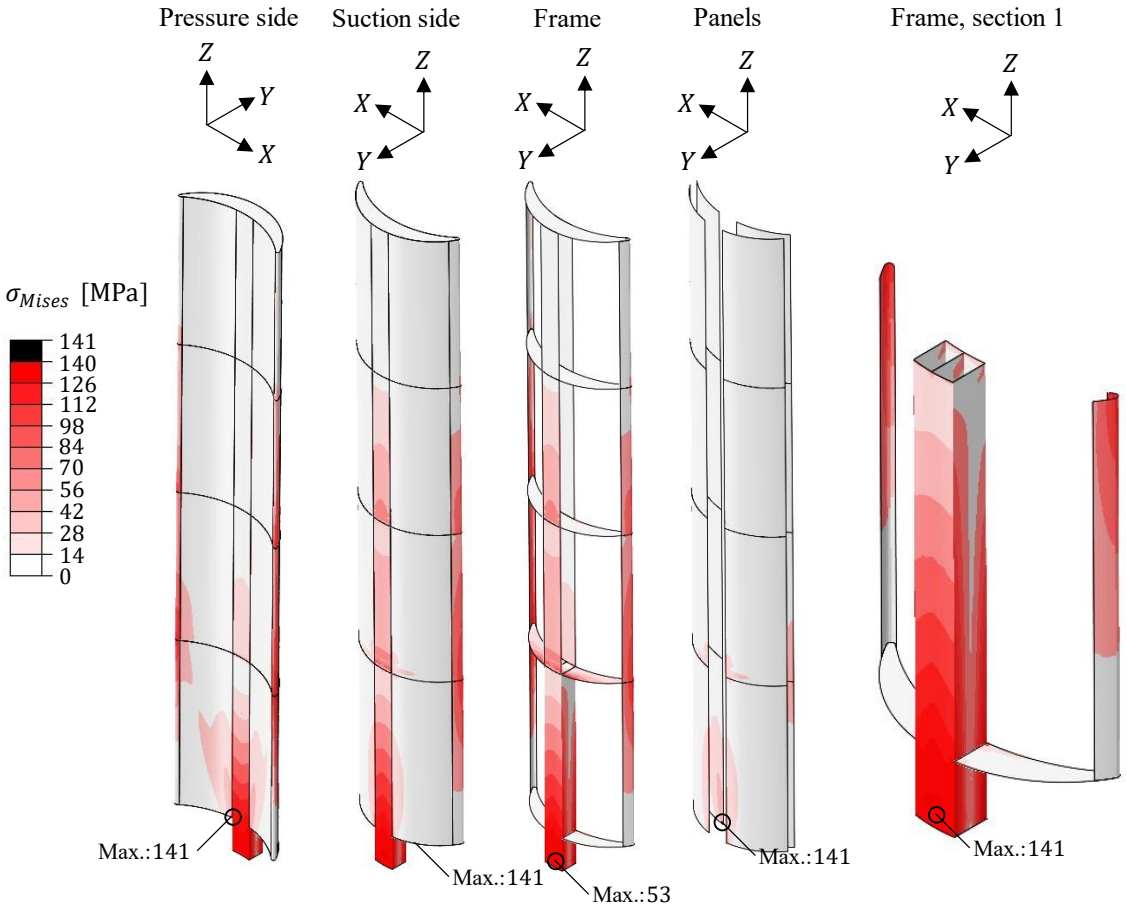

(a) Steel frame, aluminum panels.

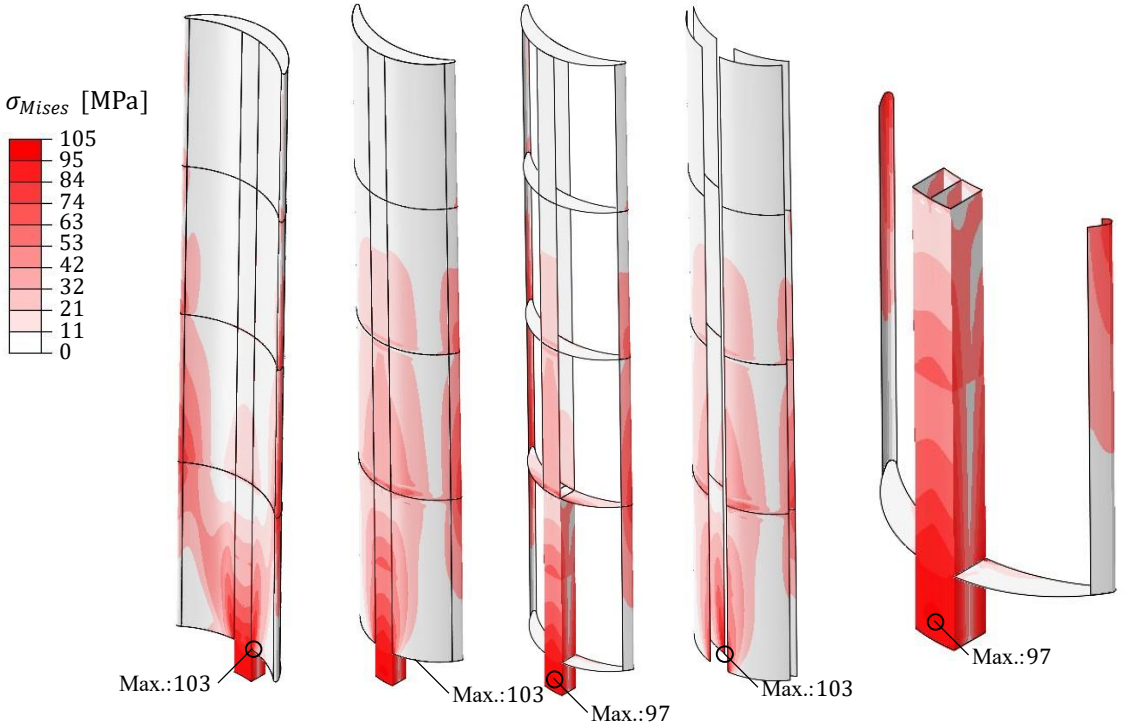

(b) All in aluminum.

Figure 22. Von Mises stress distribution for the concept utilizing a cubic mast.

Figure 22 shows the von Mises stress distributions for the two material arrangements. When the wingsail has a steel frame, as shown in Figure 22(a), the maximum von Mises stress occurs at the bottom of the mast. The stress distributed throughout the panels is much lower than in the frame, so the frame bears global bending. On the other hand, for the "all in aluminum" concept shown in Figure 22(b), the stress in the panels is comparatively larger, although the distribution of von Mises stress throughout the frame shows similar characteristics. The maximum von Mises stress is found at the contact area of the mast and the bottom plate. The stress concentration is reduced by introducing the cubic mast, but stress still occurs. The maximum von Mises stress occurs at the contact area of the mast and the bottom for both material arrangements.

The risk of buckling due to compressive normal stress is assessed in this thesis by calculating the buckling stress of the mast according to Euler's formula for buckling and comparing it with the maximum compressive normal stress from the FEA results. Shear buckling is not studied here since the shear stress throughout the wingsail structure is lower than normal stress. Additionally, shear stress mainly occurs at horizontal section plates, which are unaffected by global bending and are much thicker and stronger than the other parts of the structure.

Compressive normal stress mainly occurs in the mast and central plates. The riskiest part with the highest compressive normal stress is the bottom of the mast on the suction side of the wingsail, which is the compressed side in the structural response. For the all-aluminum arrangement, the normal stress distribution shows similar characteristics. High compressive normal stress brings the risk of buckling at the mast. To reduce the compressive normal stress at the bottom of the mast, several solutions can be considered, such as making the lower part of the mast thicker or adding stiffeners inside the mast.

3.3.3 Rigidity

The characteristics of the distribution of the deformation displacement in the Y direction (γ_y) are similar for the two material arrangements, as shown in Figure 23. In the all-aluminum structure, the displacement is around twice as large as in the structure with a steel frame and aluminum panels. For the steel frame structure, maximum displacement occurs at the edges of the top plate, while for the all-aluminum structure, it occurs at the middle of the top plate. Hence, the rigidity of the center plates is higher than that of the edges when applying a steel frame, but for the all-aluminum arrangement, the edges show higher rigidity. In addition, the deformation of section 1 is small due to the strong mast, especially with the steel frame arrangement. A possible solution to increase the rigidity of the higher sections would be to add a vertical plate expanding in the Y direction between the center plates for each section, but it may affect the telescopic function of the wingsail.

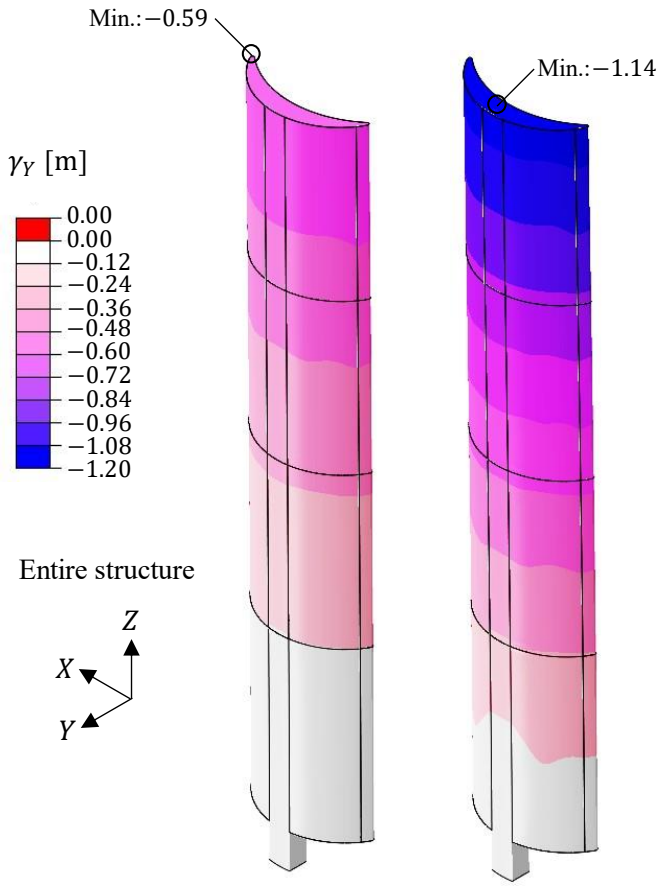

(a) Steel frame, aluminum panels.

(b) All in aluminum.

Figure 23. The deflection magnitude distribution for the concept utilizing a cubic mast.

It is also found that the center plates of section 2 experience significant rotation at their bottom, increasing the displacement of the upper sections (i.e., sections 2, 3, and 4). Therefore, compressive normal stress also occurs there, so the lower part of each center plate can be made thicker, or some extra stiffeners can be added for reinforcement.

4 Conclusions and future work

4.1 Conclusions

4.1.1 Practical significance

In conclusion, this thesis demonstrates the significant potential of wingsails in augmenting ship propulsion and reducing fuel consumption. The introduction of the novel crescent-shaped sail profile proves to be more effective in generating thrust force compared to the NACA 0015 profile, as evidenced by high-fidelity CFD simulations, as the potential thrust force coefficient is approximately 30% higher. Although the lift-to-drag ratio of the crescent-shaped wingsail is much lower than that of NACA 0015, F_D is seldom negative for propulsion, except under headwind conditions.

The implementation of crescent-shaped wingsails presents a promising avenue for enhancing the efficiency and sustainability of maritime transportation since the case study highlights the considerable fuel savings that can be achieved by installing a single crescent-shaped wingsail, with anticipated savings ranging from 9% in $V_{TW} = 10$ kn to 25% in $V_{TW} = 20$ kn. Furthermore, the long-term fuel saving prediction indicates that the overall savings attributed to the crescent-shaped wingsail amount to 9.5%. One drawback of the new profile is the increased resistance experienced when sailing against the wind; however, such occurrences are infrequent.

4.1.2 Aerodynamic characteristics

The present study identifies certain challenges associated with the newly proposed wingsail profile, particularly regarding flow separation. The strong flow separation observed in this profile exacerbates flow unsteadiness and consequently imposes more unsteady surface loads on the sail, which may potentially compromise the strength and stability of the wingsail structure. The CFD results, especially those utilizing the IDDES method, reveal the presence of vortex tubes extending in the spanwise direction. These results also suggest less dissipation and energy loss in the wake region, which allows for discernible vortex structures to persist further downstream of the sail. Therefore, the wake flow may lead to interactions among sails in a ship equipped with multiple wingsails.

To investigate the effects of tip vortices on aerodynamics, this thesis employs two computational domain and spanwise side boundary condition setups: periodic boundary conditions and symmetry boundary conditions, with the top-side boundary positioned far from the sail's top-side edge to minimize boundary influence on flow. The sail configuration is affixed to the bottom side boundary, which is the water-free surface and is, therefore, subject to symmetry boundary conditions. The second case reproduces the vortices induced from the tip of the wingsail. Moreover, as side-edge vortices exist, this effect alleviates the breaking of the spanwise coherence in the vortex shedding that evolves downstream of the sail trailing edge.

4.1.3 Modeling experience

Two-dimensional simulations generally overestimate the force coefficients for the crescent-shaped profile. This discrepancy can be attributed to the exclusion of vortex evolution and coherence in the spanwise direction in two-dimensional simulations, as well as lift reduction caused by tip vortices due to the freestream tip. Despite these differences, both the two- and three-dimensional simulations exhibit similar trends in force changes concerning the angles of attack. Consequently, by rescaling the two-dimensional results to a limited number of three-dimensional simulation cases, propulsive performance can be effectively predicted.

For the time-averaged force coefficients, which are crucial to propulsive performance, both uRANS and IDDES methods yield similar predictions. However, the external loads that these methods predict exhibit distinct unsteady characteristics, which are expected to significantly impact the structural response. FFT analysis reveals that the uRANS-based results display more pronounced low-frequency oscillations, while the IDDES-based results capture the high-frequency characteristics of external loads. These high-frequency oscillations may contribute to local vibrations or buckling of the structures, warranting further investigation in future FSI analyses. Being able to provide more detailed information about the flow field, particularly in terms of vortex shedding in the wake region, is likely responsible for this difference, as large-scale eddies are resolved without modeling in the IDDES method.

4.1.4 Structural design and evaluation

In conclusion, the structural analysis demonstrates that the wingsail concept featuring a strong frame with a cuboid mast and lightweight panels offers superior performance in terms of weight, strength, and rigidity. Among the assessment criteria considered, strength—specifically, von Mises yield and compressive normal stress—emerges as the most critical factor when evaluating wingsail structures. The cuboid mast design has the advantage of mitigating stress concentration in the lower sections, particularly at the interface between the mast and the bottom plate. Extending the mast throughout section 1 also alleviates stress concentration on section 2's horizontal plate. In comparison to the previous concept utilizing vertical stiffeners, the "frame and panels" concept achieves the necessary strength at a significantly reduced weight. Substituting steel with aluminum can further decrease the frame's weight by approximately 50%, although the flexibility, as indicated by the tip displacement, increases.

To summarize, this thesis predicts the propulsive performance and structural response of a single crescent-shaped wingsail. This thesis also provides insights into the potential causes of structural instability or fatigue in relation to fluid dynamics, which will occur due to multi-wingsail interaction problems. This can be extended to guide the design of wingsail geometries and installation.

4.2 Future work

Three main areas of future work are identified, namely multiple wingsail interaction, FSI analysis, and hull–wingsail interaction.

Usually, two or more wingsails are installed on a ship to increase its propulsive power. In addition, a wingsail with a crescent-shaped profile affects the wake flow over a relatively long distance. Therefore, when more than one wingsail is installed on a ship, the interactions among these wingsails can be important. The first main area, multiple wingsail interaction, entails using numerical and experimental methods to study the aerodynamic interactions among multiple wingsails. This area can include how multi-wingsail interaction affects the wind loads on the wingsail, what the characteristics of the flow field that multiple wingsails induce are, and which arrangement of the wingsails provides better propulsive performance.

Wind loads on the wingsail are unsteady, and they experience oscillations with both low and high frequencies, which cause vortex-induced vibrations. Hence, dynamic structural responses need to be studied. In addition, the deformation and vibration of the structure may influence the flow field, and the affected flow field may also influence wind loads, so the second area of study, FSI analysis, is proposed to solve these problems. FSI analysis can be fully coupled simulations, i.e., coupled FEA and CFD at each time step, or aeroelastic simulations with the assumption that the geometry deformation of the section profile can be ignored.

The third area of study, the interaction between wingsails and the hull, is vital for WASP, as it influences overall performance. Aerodynamic and hydrodynamic interactions affect lift, drag, and resistance, while structural considerations ensure integrity and stability. The wingsails' position and size can impact balance and maneuverability, necessitating careful integration with the hull. Hence, analyzing and optimizing this interaction is essential for efficient propulsion and vessel performance. This methodology may involve coupling aerodynamic and hydrodynamic simulations, i.e., two-phase flow simulations.

Other ideas for future work can be the optimization of wingsail geometry for improved aerodynamic efficiency and life cycle assessment to evaluate the sustainability of the wingsail, among others.

References

Allenström, B., Li, D.-Q., & Ran, H. (2012). EffShip report WP6 wind, wave and solar energy. In *Gothenburg: SSPA*.

ASTM. (2004). *Standards specification for aluminum and aluminum-alloy sheet and plate*. American Society for Testing and Materials.

Atkinson, G. M. (2019). Analysis of lift, drag and CX polar graph for a 3D segment rigid sail using CFD analysis. *Journal of Marine Engineering and Technology*, *18*(1), 36–45. https://doi.org/10.1080/20464177.2018.1494953

Atkinson, G., Nguyen, H., & Binns, J. (2018). Considerations regarding the use of rigid sails on modern powered ships. *Cogent Engineering*, *5*(1), 1–20. https://doi.org/10.1080/23311916.2018.1543564

Bak, S., Yoo, J., & Song, C. Y. (2013). Fluid-structure interaction analysis of deformation of sail of 30-foot yacht. *International Journal of Naval Architecture and Ocean Engineering*, *5*(2), 263–276.

Bialystocki, N., & Konovessis, D. (2016). On the estimation of ship's fuel consumption and speed curve: A statistical approach. *Journal of Ocean Engineering and Science*, *1*(2), 157–166.

Blount, H., & Portell, J. M. (2021). *CFD investigation of wind powered ships under extreme conditions* [Chalmers University of Technology]. https://odr.chalmers.se/handle/20.500.12380/304254

BS EN. (2004). 10025-2: 2004: Hot rolled products of structural steels. Part 2-Technical delivery conditions for non-alloy structural steels. In *British Standards Institution, London*.

Cairns, J., Vezza, M., Green, R., & MacVicar, D. (2021). Numerical optimisation of a ship wind-assisted propulsion system using blowing and suction over a range of wind conditions. *Ocean Engineering*, *240*, 109903. https://doi.org/10.1016/J.OCEANENG.2021.109903

Campbell, I. C. (1995). The lateen sail in world history. *Journal of World History*, 1–23.

Carter, R. (2002). The Neolithic origins of seafaring in the Arabian Gulf. *Archaeology International*, *6*(1). https://doi.org/10.5334/ai.0613

Casson, L. (1995). *Ships and seamanship in the ancient world*. JHU Press.

Castro, F., Fonseca, N., Vacas, T., & Ciciliot, F. (2008). A Quantitative Look at Mediterranean Lateen-and Square-Rigged Ships (Part 1). *International Journal of Nautical Archaeology*, *37*(2), 347–359.

Chen, Z., Cai, W., & Zeng, Q. (2022). A numerical study on the thrust and interaction of a three-sail wind-assisted propulsion system. *Proceedings of the ASME 2022, 41st International Conference on Ocean, Offshore and Arctic*.

Cunliffe, T. (2016). *The Complete Day Skipper: Skippering with Confidence Right From the Start (5 ed.)*. Bloomsbury Publishing.

Dassault Systemes. (2020). Abaqus 2020. In *Abaqus Analysis User's Guide*.

Davidson, L. (2019). *Fluid mechanics, turbulent flow and turbulence modeling*. Division of Fluid Dynamics, Department of Mechanics and Maritime Sciences, Chalmers University of Technology.

DNV. (2022). *[DNV-ST-0511] Wind assisted propulsion systems - edition Oct, 2022*. https://standards.dnv.com/explorer/document/C0E1D699CA1748C585C31004BC1B1C85/5?_ga=2.144478517.1272353220.1681210027-409665076.1638902377

Ellis, S. (2005). *The Phantom Voyagers: Evidence of Indonesian settlement in Africa in ancient times, by Robert Dick-Read. Winchester: Thurlton Publishing, 2005. 251 pp.£ 15.99 paperback. ISBN 0-9549231-0-3 (paperback).* Oxford University Press.

EUROSTAT. (2019). *Greenhouse gas emissions by source sector*. EUROSTAT.

Fagerlund, P., & Ramne, B. (2010). *Teleskopiskt segelarrangemang* (Patent No. 1001108–8).

Gadonneix, P., Sambo, A., Tie'nan, L., Choudhury, A. R., Teyssen, J., Lleras, J. A. V., Naqi, A. A., Meyers, K., Shin, H. C., & Nadeau, M.-J. (2011). Global transport scenarios 2050. *World Energy Council*, *456*.

Gaynor, J. L. (2013). Ages of sail, ocean basins, and Southeast Asia. *Journal of World History*, 309–333.

Hamada, N. (1985, November). The development in Japan of modern sail-assisted ships for energy conservation. *Regional Conference on Sail-Motor Propulsion*. https://trid.trb.org/view/400086

Hoerner, S. F. (1976). Fluid-Dynamic Drag: Practical Information on Aerodynamic Drag and Hydrodynamic Resistance. In *The Aeronautical Journal* (Vol. 80, Issue 788). Cambridge University Press. https://doi.org/10.1017/s0001924000034187

Hu, Y., He, J., Tang, J., Xue, S., Liu, S., & Wu, Y. (2015). Sail Structure Design and Stability Calculation for Sail-assisted Ships. *Marine Engineering Frontiers*, *3*(0), 1. https://doi.org/10.14355/mef.2015.03.001

IMO. (2018). *Interpretation of Initial IMO Strategy on Reduction of GHG Emissions from Ships* (Vol. 60, Issue 1, pp. 195–201).

International Chamber of Shipping. (2014). *Shipping, world trade and the reduction of CO2 emissions*. London: International Chamber of Shipping.

International Transport Forum. (2020). *Navigating towards cleaner maritime shipping*. OECD Publishing. www.itf-oecd.org

Johnstone, P. (2013). *The sea-craft of prehistory*. Routledge.

Khan, L., Macklin, J., Peck, B., Morton, O., & Souppez, J.-B. R. G. (2021, September 15). A review of wind-assisted ship propulsion for sustainable commercial shipping: Latest developments and future stakes. *Proceedings of the Wind Propulsion Conference 2021*.

Kijima, K., Katsuno, T., Nakiri, Y., & Furukawa, Y. (1990). On the manoeuvring performance of a ship with theparameter of loading condition. *Journal of the Society of Naval Architects of Japan*, *1990*(168), 141–148.

Kimball, J. (2009). *Physics of Sailing*. CRC Press. https://doi.org/10.1201/9781420073775

Köhler, J., Traut, M., Faber, J., Nelissen, D., Mao, W., & Ahdour, S. (2016). *Study on the analysis of market potentials and market barriers for wind propulsion technologies for ships : final report*. Publications Office. https://doi.org/doi/10.2834/68747

Larsson, L. (1990). Scientific methods in yacht design. *Annual Review of Fluid Mechanics*, *22*(1), 349–385.

Lee, H., Jo, Y., Lee, D. J., & Choi, S. (2016). Surrogate model based design optimization of multiple wing sails considering flow interaction effect. *Ocean Engineering*, *121*, 422–436. https://doi.org/10.1016/j.oceaneng.2016.05.051

Lu, R., & Ringsberg, J. W. (2020). Ship energy performance study of three wind-assisted ship propulsion technologies including a parametric study of the Flettner rotor technology. *Ships and Offshore Structures*, *15*(3), 249–258. https://doi.org/10.1080/17445302.2019.1612544

Ma, Y., Bi, H., Gan, R., Li, X., & Yan, X. (2018). New insights into airfoil sail selection for sail-assisted vessel with computational fluid dynamics simulation. *Advances in Mechanical Engineering*, *10*(4), 1–12. https://doi.org/10.1177/1687814018771254

Mahdi, W. (1999). The dispersal of Austronesian boat forms in the Indian Ocean. *Archaeology & Language III, Artefacts, Languages and Texts*, 144–208.

Malmek, K., Dhomé, U., Larsson, L., Werner, S., Ringsberg, J. W., & Finnsgård, C. (2020). Comparison of two rapid numerical methods for predicting the performance of multiple rigid wing-sails. *The 5th International Conference on Innovation in High Performance Sailing Yachts and Sail-Assisted Ship Propulsion (INNOV'SAIL 2020)*.

Menter, F. R. (1993). Zonal two equation κ-ω turbulence models for aerodynamic flows. *AIAA 23rd Fluid Dynamics, Plasmadynamics, and Lasers Conference, 1993*. https://doi.org/10.2514/6.1993-2906

Menter, F. R., Smirnov, P. E., Liu, T., & Avancha, R. (2015). A One-Equation Local Correlation-Based Transition Model. *Flow, Turbulence and Combustion 2015 95:4*, *95*(4), 583–619. https://doi.org/10.1007/S10494-015-9622-4

Najjar, F. M., & Vanka, S. P. (1995). Effects of intrinsic three-dimensionality on the drag characteristics of a normal flat plate. *Physics of Fluids*, *7*(10), 2516–2518.

Nikmanesh, M. (2021). *Sailing performance analysis using CFD simulations: A study on crescent shaped wing profiles* [Chalmers University of Technology]. https://odr.chalmers.se/handle/20.500.12380/304303

Ouchi, K., Uzawa, K., & Kanai, A. (2011). Huge Hard Wing Sails for the Propulsor of Next Generation Sailing Vessel. *Second International Symposium on Marine Propulsors*, *June*, 1–5.

Ouchi, K., Uzawa, K., Kanai, A., & Katori, M. (2013). Wind challenger" the next generation hybrid sailing vessel. *The Third International Symposium on Marine Propulsors, Launceston, Tasmania, Australia*, 562–567.

Park, J. S., Witherden, F. D., & Vincent, P. E. (2017). High-order implicit large-eddy simulations of flow over a NACA0021 aerofoil. *AIAA Journal*, *55*(7), 2186–2197. https://doi.org/10.2514/1.J055304

Patankar, S. V. (1980). *Numerical heat transfer and fluid flow*. CRC Press. https://doi.org/10.13182/nse81-a20112

Persson, A., Li, D.-Q., Olsson, F., Werner, S., & Dhomé, U. (2019). Performance prediction of wind propulsion systems using 3D CFD and route simulation. *RINA, Royal Institution of Naval Architects-International Conference on Wind Propulsion, WP 2019, 15-16 October 2019, London, United Kingdom*, 19–30.

Prevljak, N. H. (2022, October 10). World's 1st cargo ship equipped with 'Wind Challenger' delivered. *Offshore Energy*.

Reichardt, H. (1951). Vollständige Darstellung der turbulenten Geschwindigkeitsverteilung in glatten Leitungen. *ZAMM - Journal of Applied Mathematics and Mechanics / Zeitschrift Für Angewandte Mathematik Und Mechanik*, *31*(7), 208–219. https://doi.org/10.1002/ZAMM.19510310704

Satchwell, C. J. (1985). Applications of Windship Technology in the Design and Operation of Wind-Propelled Ships. *Regional Conference on Sail-Motor Propulsion*.

Sauzé, C., & Neal, M. (2008). Design considerations for sailing robots performing long term autonomous oceanography. *Proceedings of the International Robotic Sailing Conference*, *27*(2), 21–29. www.roboticsailing.org

Sheldahl, R. E., & Klimas, P. C. (1981). *Aerodynamic characteristics of seven symmetrical airfoil sections through 180-degree angle of attack for use in aerodynamic analysis of vertical axis wind turbines.* https://doi.org/10.2172/6548367

Shur, M. L., Spalart, P. R., Strelets, M. K., & Travin, A. K. (2008). A hybrid RANS-LES approach with delayed-DES and wall-modelled LES capabilities. *International Journal of Heat and Fluid Flow*, *29*(6), 1638–1649. https://doi.org/10.1016/j.ijheatfluidflow.2008.07.001

Siemens PLM Software. (2021). *STAR-CCM+ user guide (version 16.02)*. Siemens PLM Software Inc: Munich, Germany.

Silva, M. F., Friebe, A., Malheiro, B., Guedes, P., Ferreira, P., & Waller, M. (2019). Rigid wing sailboats: A state of the art survey. *Ocean Engineering*, *187*, 106150. https://doi.org/10.1016/j.oceaneng.2019.106150

Smagorinsky, J. (1963). General circulation experiments with the primitive equations. *Monthly Weather Review*, *91*(3), 99–164. https://doi.org/10.1175/1520-0493(1963)091<0099:gcewtp>2.3.co;2

Smith, T. W. P., Jalkanen, J. P., Anderson, B. A., Corbett, J. J., Faber, J., Hanayama, S., O'keeffe, E., Parker, S., Johansson, L., & Aldous, L. (2015). *Third IMO greenhouse gas study 2014*.

Snell, D. C. (2008). *A companion to the ancient Near East*. John Wiley & Sons.

Storhaug, G., Borzacchiello, G. R., & Hoffmeister, H. (2022). Fatigue assessment of wind assisted propulsion systems. *Proceedings of the ASME 2022 41st Internal Conference on Ocean, Offshore and Arctic Engineering*.

Tillig, F., & Ringsberg, J. W. (2019). A 4 DOF simulation model developed for fuel consumption prediction of ships at sea. *Ships and Offshore Structures*, *14*(sup1), 112–120.

Tillig, F., & Ringsberg, J. W. (2020). Design, operation and analysis of wind-assisted cargo ships. *Ocean Engineering*, *211*, 107603. https://doi.org/10.1016/j.oceaneng.2020.107603

Tillig, F., Ringsberg, J. W., Mao, W., & Ramne, B. (2017). A generic energy systems model for efficient ship design and operation. *Proceedings of the Institution of Mechanical Engineers, Part M: Journal of Engineering for the Maritime Environment*, *231*(2), 649–666.

Tillig, F., Ringsberg, J. W., Psaraftis, H. N., & Zis, T. (2019). ShipCLEAN–an integrated model for transport efficiency, economics and CO2 emissions in shipping. *Proceedings of the 2nd International Conference on Modelling and Optimization of Ship Energy Systems (MOSES 2019)*, 8–10.

Traut, M., Gilbert, P., Walsh, C., Bows, A., Filippone, A., Stansby, P., & Wood, R. (2014). Propulsive power contribution of a kite and a Flettner rotor on selected shipping routes. *Applied Energy*, *113*, 362–372. https://doi.org/10.1016/j.apenergy.2013.07.026

Viola, I. M., Biancolini, M. E., Sacher, M., & Cella, U. (2015). A CFD-based wing sail optimisation method coupled to a vpp. *5th High Performance Yacht Design Conference, HPYD 2015*, 1–7.

Viola, I. M., Sacher, M., Xu, J., & Wang, F. (2015). A numerical method for the design of ships with wind-assisted propulsion. *Ocean Engineering*, *105*, 33–42. https://doi.org/10.1016/j.oceaneng.2015.06.009

Wilcox, D. C. (1989). *Turbulence Modeling for CFD* (Vol. 27, Issue 10).

Workinn, D. (2021). *A high-level interface for a sailing vessel* [KTH Royal Institute of Technology]. http://urn.kb.se/resolve?urn=urn:nbn:se:kth:diva-299430

Yao, H., Davidson, L., & Chroneer, Z. (2018). *Investigation of interior noise from generic side-view mirror using incompressible and compressible solvers of DES and LES*. SAE Technical Paper. https://doi.org/https://doi.org/10.4271/2018-01-0735

Yao, H.-D., He, G.-W., Wang, M., & Zhang, X. (2008). Time correlations of pressure in isotropic turbulence. *Physics of Fluids*, *20*(2), 025105. https://doi.org/https://doi.org/10.1063/1.2870111

Zhu, H. (2020). *CFD Investigation of Wind-powered Ships under Extreme Condition* [Chalmers University of Technology]. https://odr.chalmers.se/handle/20.500.12380/301919

Paper I

Propulsive Performance Analysis of a Rigid Wingsail with Crescent-Shaped Profiles Based on Unsteady RANS CFD

Propulsive Performance Analysis of a Rigid Wingsail with Crescent-Shaped Profiles Based on Unsteady RANS CFD

Heng Zhu[1,*], Hua-Dong Yao[1], Fabian Thies[1], Jonas W. Ringsberg[1], Bengt Ramne[2]

[1] Chalmers University of Technology, Department of Mechanics and Maritime Sciences, Gothenburg, Sweden

[2] ScandiNAOS AB, Gothenburg, Sweden

[*] Corresponding author: heng.zhu@chalmers.se

Abstract

The use of wind-powered ship propulsion is considered an effective method for reducing greenhouse gas emissions. This study presents numerical analyses of the aerodynamics of a single rigid wingsail, using the unsteady Reynolds-averaged Navier-Stokes (uRANS) equations. The wingsail is designed with a new sectional profile, the crescent-shaped foil. A comparison of this new profile and the classical NACA 0015 profile is carried out. The simulations are performed in both two and three dimensions, with a focus on key physical quantities such as the external loads on the wingsail, the flow field, and the propulsive performance. It is concluded that the wingsail with the crescent-shaped section has higher propulsion efficiency than the NACA0015. However, stronger flow separation is found for the former section. As the separation deteriorates the flow unsteadiness, this effect poses a challenge to the strength and stability of the wingsail structure. Moreover, the three-dimensional simulations of both profiles, particularly NACA 0015, show that the tip vortices induced from the side edge of the wingsail account for substantial negative effects on the propulsion performance. A case study with the crescent sail profile is carried out and reveals that this design reduced fuel consumption by 9%.

KEYWORDS: *crescent-shaped profile, high Reynolds number, rigid wingsail, unsteady RANS, wind-assisted ship propulsion*

Nomenclature

A_S	Sail area [m^2]
C_D	Drag force coefficient
C_L	Lift force coefficient
C_M	Moment coefficient
C_p	Pressure coefficient
C_T	Thrust force coefficient
C_τ	Wall shear stress coefficient
F_D	Drag force [N]
F_L	Lift force [N]
F_S	Side force [N]
F_T	Thrust force [N]
H	Sail height (spanwise length) [m]
L_c	Chord length [m]
p	Pressure [Pa]
Q	Q-criterion [s^{-2}]
Re	Reynolds number
V_{AW}	Apparent wind speed [m/s]
V_S	Ship speed [m/s]
V_{TW}	True wind speed [m/s]
V_X	Streamwise velocity [m/s]
V_Z	Spanwise velocity [m/s]
X_c	Chord-wise position [m]
y^+	Dimensionless wall-normal distance
α	Angle of attack [°]
α_c	Critical angle of attack [°]
θ_{AW}	Apparent wind angle [°]
θ_{TW}	True wind angle [°]
μ	Dynamic viscosity [Pa · s]
ρ	Air density [kg/m^3]

1. Introduction

Transportation accounts for a considerable proportion of greenhouse gas (GHG) emissions. According to the data in 2016 (Ritchie et al., 2020), transportation produces 16% of the total GHG emissions worldwide, with shipping representing 11% of transportation emissions. Most of the trade volume (around 90%) is transported by shipping (International Chamber of Shipping, 2014). For instance, a Pure Car and Truck Carrier (PCTC) may consume 30 to 60 tons of fossil fuel per day depending on how it is operated (Bialystocki & Konovessis, 2016). From 2007 to 2012, ocean-going ships consumed an average of 250 to 325 million tons of fuel per year and emitted 740 to 795 million tons of CO_2 (Smith et al., 2015). A previous study projected that the world's transportation needs could double by 2050 (Gadonneix et al., 2011). To address this problem, the International Maritime Organization (IMO) has agreed that shipping must become more energy-efficient and reduce GHG

emissions to 50% of 2008 levels by 2050 (IMO, 2018).

Wind-assisted propulsion for large commercial ships is considered one of the most promising solutions to reduce shipping's dependence on fossil fuels. Different categories of innovative sail technologies have been proposed, such as rotor sails, vertical airfoils (also termed Ventifoils or suction wings), kites, wind turbines, and various wingsails (Khan et al., 2021). Several of these technologies are already used on passenger and merchant vessels, while some are still subjected to further optimization or full-scale testing in research projects (Cairns et al., 2021). Lu and Ringsberg (Lu and Ringsberg 2020) compared three sail technologies (the Flettner rotor, the DynaRig, and a classical wingsail with airfoil profiles) with regard to the actual fuel savings for a specific ship sailing on specific voyage routes. Their study showed that wind-assisted ship propulsion technologies reduced fuel consumption by several percentages. The amount of fuel savings depended on many factors for each of the three technologies. One of the crucial factors was the sail's performance for the wide range of angles of attack (α) related to the ship's heading direction. A sail's performance also depends on the aerodynamic interactions between the sails on the ship if more than one sail is installed.

Several studies have been carried out, using numerical methods, to evaluate the performance of wind-assisted ship propulsion systems based on rigid sails. Ouchi et al. (Ouchi et al. 2011) performed full-scale computational fluid dynamics (CFD) simulations to evaluate the propulsive performance of a nine-wingsail system and carried out a case study for evaluation. Viola et al. (Viola et al. 2015) developed a numerical optimization procedure for a rigid wingsail using the Reynolds-averaged Navier–Stokes (RANS) equations solver, which offered an efficient parametric sail aerodynamic analysis method. Persson et al. (Persson et al. 2019) presented simplified approaches to model wind-assisted ship propulsion systems, using a limited number of CFD simulation results to extrapolate the propulsive performance under various conditions. Tillig and Ringsberg (Tillig & Ringsberg, 2020) presented a novel approach to analytically capture aero- and hydrodynamic interaction effects on wind-propelled ships. The low-aspect-ratio wing theory was applied and modified to predict the lift and drag forces of hulls sailing at drift angles. The sails' aerodynamic interaction effects were captured by numerically solving the Navier-Stokes equations for incompressible, creeping flow. Malmek et al. (Malmek et al. 2020) developed two cost-effective aerodynamic methods to predict the performance of large-scale wingsails. One was based on the lifting line theory of potential flow in combination with pre-calculated two-dimensional RANS CFD data, and the other is a vortex lattice method (VLM). Zhu (Zhu 2020), and Blount and Portell (Blount & Portell, 2021) performed detached eddy simulations (DES) to study the performance of wingsails with a NACA 0015 profile under downwind conditions.

The studies mentioned above were mainly based on wingsails with conventional airfoil profiles, such as the NACA series. It is worth noting that the profiles have no cambers to adapt to wind directions in practice. However, including a camber in the profile geometry can substantially increase the lift coefficient. This mechanism is also valid for sails. Atkinson (Atkinson 2019) performed three-dimensional CFD simulations for studying a segmented rigid sail. Nikmanesh (Nikmanesh 2021) put forward a crescent-shaped profile, which is cambered, and predicted the propulsive performance by conducting unsteady RANS (URANS) simulations based on the Spalart–Allmaras turbulence model, indicating that this kind of profile provides a higher C_L, leading to larger thrust. Chen et al. (Chen et al. 2022), introduced a set of arc-shaped wingsails and studied their aerodynamic characteristics by performing two-dimensional simulations.

This study introduces a concept design of a telescopic wingsail with a new crescent-shaped profile. To evaluate its performance, two- and three-dimensional CFD simulations have been using uRANS with the k-ω SST turbulence model. One objective of this study is to address suitable sail configurations with an advantageous lift force coefficient (C_L) to maximize the thrust force (F_T) for large sailing merchant ships and their ship operation profiles. This study compares the propulsive performance of two rigid wingsails with different sectional profiles (NACA 0015 and crescent-shaped profiles). The analysis also focuses on exploring the flow field properties, including the flow separation points, tip vortices, as well as the impacts on the external loading conditions on the wingsails. A case study where the crescent-shaped wingsail is applied to a ship is included, using the ship-modeling platform ShipCLEAN (Tillig et al., 2019) to evaluate the propulsive performance.

2. Methodology

2.1 Concept design

In this study, the propulsive performance of a wind-assisted ship propulsion concept based on telescopic rigid wingsails with a crescent-shaped sectional profile is analyzed. The rig is designed to have a telescopic function so that it can be better operated under different conditions. For example, under weak-wind conditions, the sails can be fully expanded to capture maximum thrust, while they can be retracted under strong-wind conditions to protect the structures. Some existing conceptual wingsails, such as the Oceanbird (Workinn, 2021), were designed to have a larger section area at the

bottom and a smaller section area close to the tip. But in the proposed concept, because of the telescopic function, the wingsail is designed to be uniformly extruded, which means that the shape of the sectional profile remains the same through the spanwise direction, as shown in Figure 1.

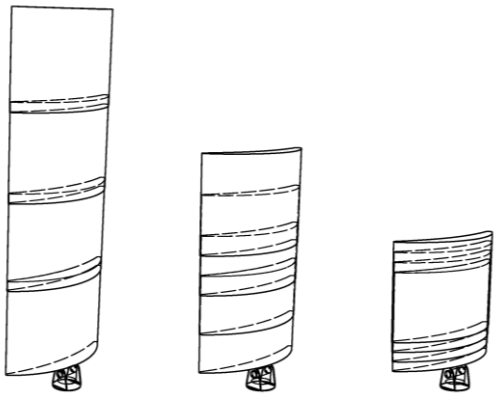

Figure 1. Telescopic rig with retractable crescent-shaped panels.

2.1.1 Wind triangle

For ships using rigid wingsails, the wind load on the wingsails produces the thrust propelling the ships. Usually, the thrust force is transferred through the mast from the wingsails to the ship. The external loads on the sail depend on the speed of the apparent wind, which is the wind that the ship and the sails are experiencing.

Figure 2 shows the wind triangle, where the apparent wind speed (V_{AW}) (i.e., the wind speed relative to the ship) and the apparent wind angle (θ_{AW}) can be calculated by Equations (1) and (2), respectively.

$$V_{AW} = \sqrt{V_S^2 + V_{TW}^2 + 2V_S V_{TW} \cdot \cos\theta_{TW}} \tag{1}$$

$$\theta_{AW} = \tan^{-1}\left(\frac{V_{TW} \cdot \sin\theta_{TW}}{V_S + V_{TW} \cdot \cos\theta_{TW}}\right) \tag{2}$$

The external loads on the sail include the force and the moment, as Figure 2 shows. From the aerodynamics aspect, the component of the total force on the sail that is parallel to the apparent wind speed is the drag force, while that perpendicular to the apparent wind speed is the lift force. On the other hand, from the practical aspect, the component that is parallel to the ship's speed is the thrust force, which can be calculated by Equation (3), while that perpendicular to the ship's speed is the side force. The magnitude of the thrust force represents the propulsive performance of the wind-assisted propulsion system, so one of the most important objectives of a wind-assisted propulsion concept is to generate a thrust force that is as large as possible. The side force does not account for the propulsion and causes heeling, rolling, drift, and induced resistance.

$$F_T = F_L \cdot \sin\theta_{AW} - F_D \cdot \cos\theta_{AW} \tag{3}$$

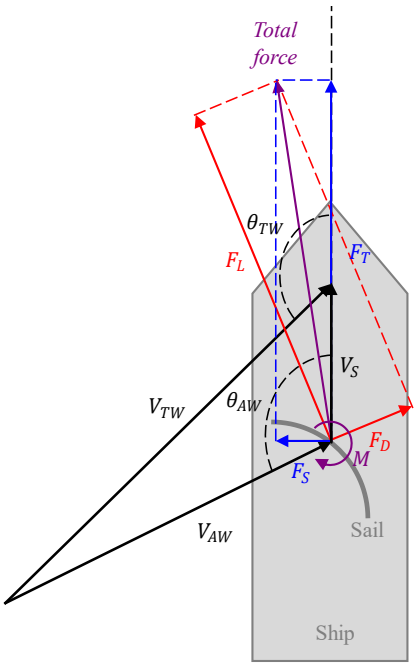

Figure 2. Wind triangle and loads on a sail.

In this study, CFD simulations are used to predict the aerodynamic forces F_L and F_D. The non-dimensional force coefficients C_L and C_D are defined by Equations (4) and (5), respectively. The moment coefficient is defined by Equation (6).

$$C_L = \frac{F_L}{0.5\rho V_{AW}^2 A_S} \tag{4}$$

$$C_D = \frac{F_D}{0.5\rho V_{AW}^2 A_S} \tag{5}$$

$$C_M = \frac{M}{0.5\rho V_{AW}^2 A_S L_c} \tag{6}$$

Similarly, the thrust force coefficient can be obtained by Equation (7).

$$C_T = \frac{F_T}{0.5\rho V_{AW}^2 A_S} \tag{7}$$

2.1.2 Crescent-shaped sectional profile

For a sail to operate equally well on both starboard and port tack, it can either be symmetrical with respect to the chord or symmetrical with respect to the normal of the chord. According to a rough estimation based on the thin-foil theory (Houghton & Carruthers, 1982), a section profile with a substantial camber is expected to provide higher C_L than an aerodynamically symmetrical profile (e.g., NACA 0015). Although the propulsive performance of the NACA 0015 profile can be improved

by introducing a flap at the trailing edge, it would make the telescopic function hard to achieve.

Compared with traditional airfoil profiles, such as NACA 0015, a curved profile that is symmetric at both edges would be operated differently when changing the tack. The aerodynamically symmetrical profile will always have the same leading edge, but the high-pressure side will become the low-pressure side when changing from one tack to the other, which can be observed in Figure 3(a). The symmetrical profile will operate like a modern Bermuda-type sail. The crescent-shaped profile will swap the leading and trailing edge when changing tack, but the same side will always be the high-pressure side and the opposite side will always be the low-pressure side (see Figure 3(b)).

The geometry of the crescent-shaped profile used in this study is presented in Figure 4. The geometry is symmetric with respect to the center line that is normal to the profile chord. The chord length of the profile is 14 m. The maximum thickness is 2 m and locates in the middle of the chord. Given that the surfaces on the pressure and suction sides are curved, a camber is formed along the chord.

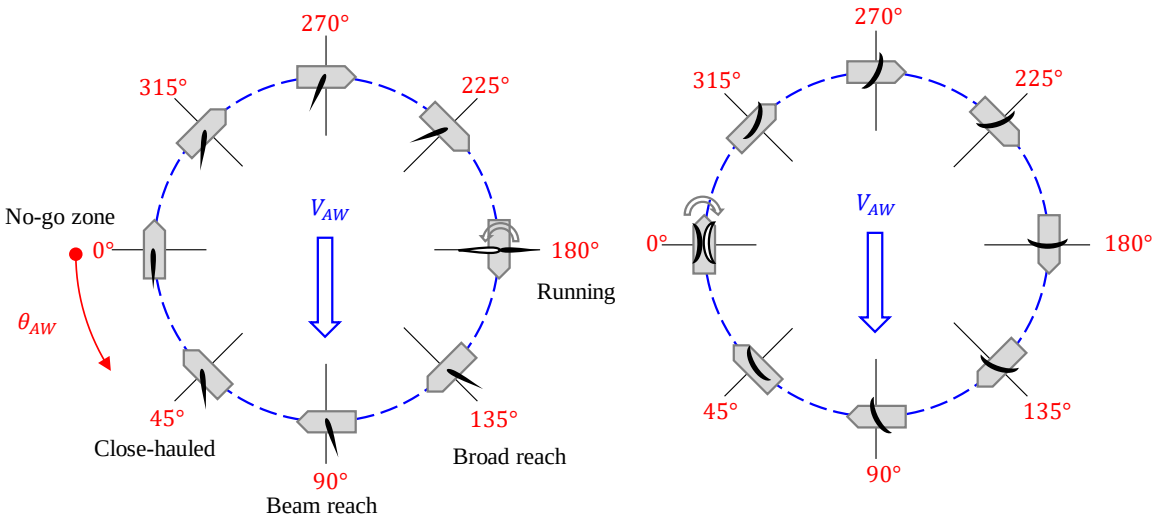

(a) Symmetric profile (NACA 0015). (b) Crescent-shaped profile.

Figure 3. Changing tack with an aerodynamically symmetrical profile and crescent-shaped profile.

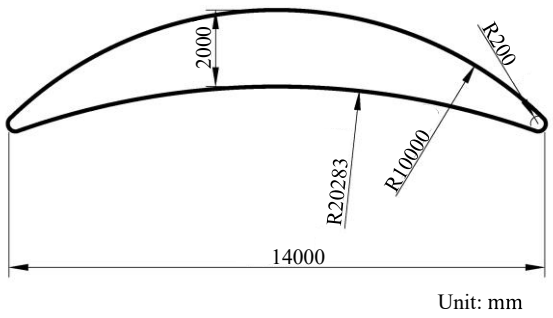

Figure 4. Dimensions of the crescent-shaped profile.

The propulsive performance of the profile varies depending on the chosen design parameters. The optimum parameters depend on both the flow and structural conditions. Based on the initial estimates (Nikmanesh, 2021), where a series of two-dimensional CFD simulations were performed, the chosen profile with the best thrust coefficient is expected to be reasonably close to the final design.

2.2 CFD simulation

2.2.1 Physical condition

CFD simulations are performed for predicting the external load on the sail. The present study makes use of the mesh generators and solvers in the commercial software STAR-CCM+ (Siemens PLM Software, 2021).

A global coordinate system is introduced for all the simulation cases in the study. The X axis has the same direction as the inlet flow. The Y axis points from the pressure side to the suction side. The Z axis vertically points from the bottom to the top. The origin locates at the bottom surface. For the crescent-shaped profile, the origin is at the center of the mean camber line (Figure 5(a)), whereas, for NACA 0015, it is located at the leading edge (Figure 5(b)).

To simulate the critical condition (i.e., a condition with high wind speed), a uniformly distributed inlet flow velocity of 25 m/s is set for the wind speed. Thus, the Reynolds number is 2.3×10^7, calculated based on the chord length of the sail sectional profile. Table 1 lists the properties of the fluid (air at 25 °C).

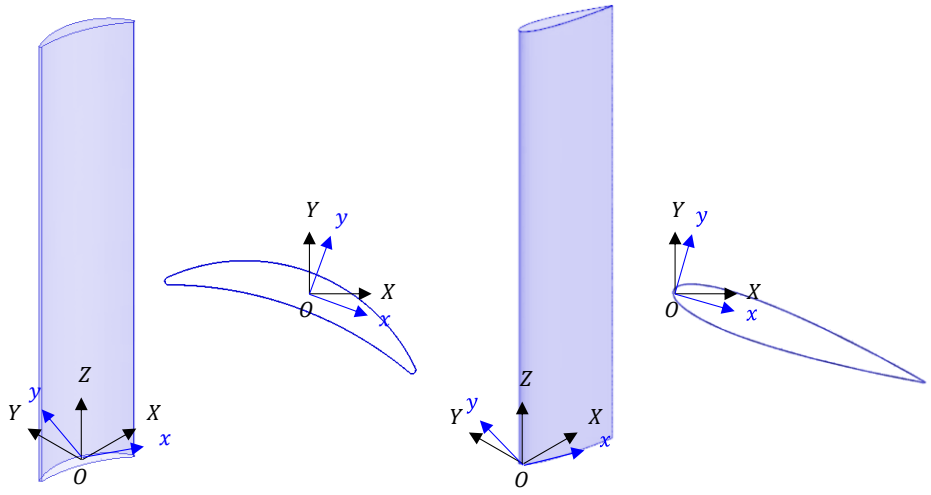

(a) Crescent-shaped profile. (b) NACA 0015.

Figure 5. Global coordinate system. For the crescent-shaped profile, $\alpha = 20°$; for NACA 0015, $\alpha = 16°$.

2.2.2 Domain and boundary conditions

Two-dimensional simulations are first performed to identify the critical angle of attack (α_c) and provide a preliminary view of the flow field. It is found that when α is around 20°, a peak of C_L can be obtained. Then, three-dimensional simulations with two sets of boundary conditions are performed to study the three-dimensional flow characteristics and the influence of tip vortices.

Table 1. Properties of the fluid (Hilsenrath, 1955).

Property	Value	Unit
μ	1.85508×10^{-5}	Pa · s
ρ	1.18415	kg/m^3

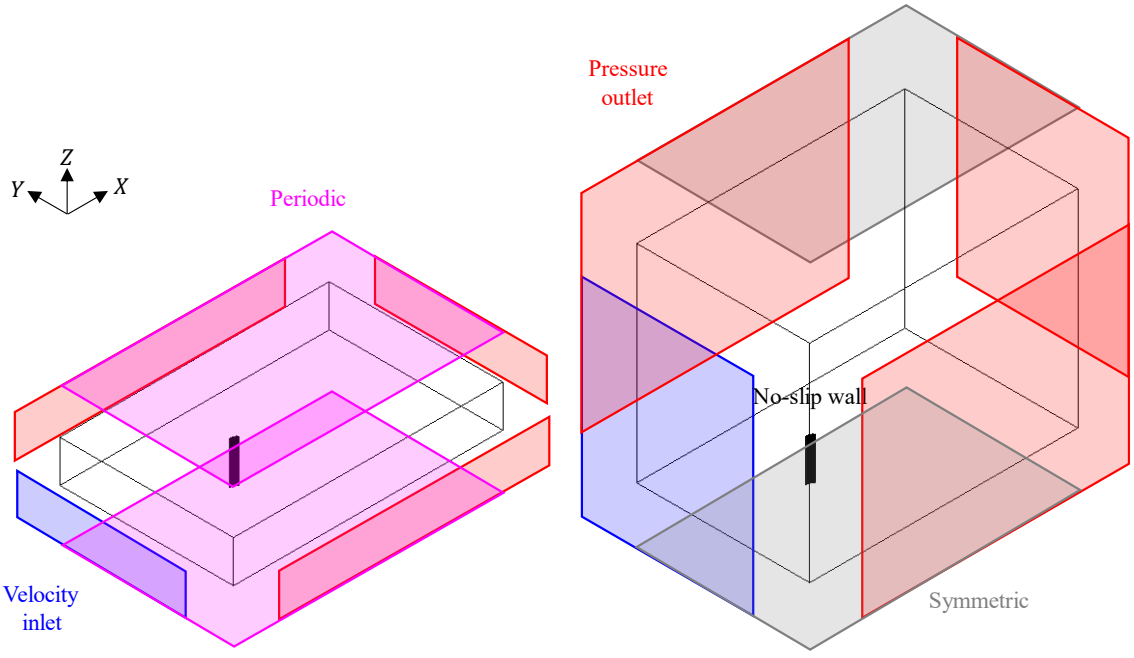

(a) Periodic top and bottom. (b) Free-stream tip and symmetric bottom.

Figure 6. Two sets of boundary conditions and computational domains for the three-dimensional simulations.

In the first set of boundary conditions, periodic boundary conditions are applied to the top and bottom boundaries of the computational domain in the spanwise direction. In the second set, symmetric boundary conditions are imposed at the bottom boundary (where the sail is attached) and the top surface, as Figure 6 shows. For both sets of boundary conditions, the side boundaries in the crossflow direction are set to the pressure outlets to make the simulations closer to the real condition. For two-dimensional simulations, the

arrangement of the inlet and outlet boundaries follows Figure 6(a). The non-slip boundary condition is specified on the wall of the wingsail. The upstream boundary of the domain is assigned as the velocity inlet. The pressure outlet boundary condition with a zero-pressure loss coefficient is imposed on the downstream boundary of the domain.

The computational domains are rectangular. Full-scale geometries are simulated in this study. Figure 7 presents the size and arrangement of the three-dimensional simulations with the freestream tip and symmetric bottom boundary conditions. The total height of the sail (i.e., the spanwise length) is 72 m in both of these series of simulation cases. For simulations with a periodic top and bottom, the spanwise size of the domain is the same as the spanwise length of the sail. For two-dimensional simulations, the size of the domain follows the size of the bottom boundary in Figure 7.

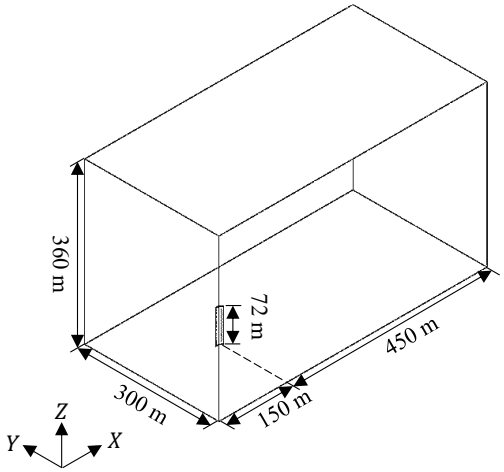

Figure 7. The computational domain of the three-dimensional simulations.

2.2.3 Turbulence modeling

Turbulence is simulated using the unsteady RANS (uRANS) with the k-ω SST model (Menter, 1993). This two-equation turbulence model computes the eddy-viscosity turbulence based on the turbulence kinetic energy and the specific turbulence dissipation rate. The convection term of the model is discretized with a second-order upwind scheme. The k - ω SST model interprets the standard k-ω model within the inner region of the boundary condition, and as in the freestream, it switches to the k-ϵ model to avoid the problem that the k-ω model is sensitive to the inlet freestream turbulence.

An approach of blended wall treatment is applied to the RANS equations (Wilcox, 1989). This approach has the advantage of treating complex geometries with local flow characteristics. Because the velocity over complex walls varies in a wide range and the geometry of the wingsail profile has a curvature, it is difficult to ensure that y^+ in all cells adjacent to the walls are either above a high value or below a small value, which is needed by a conventional wall treatment model. By contrast, the blended wall treatment is regarded as a function of the local y^+. Blended wall laws are employed to model smooth variable changes in the buffer layer between the viscous sublayer and the logarithmic region. The Reichardt law (Reichardt, 1951) is utilized for the momentum equations.

The gamma transition model (Menter et al., 2015), which solves for turbulence intermittency to predict the onset of the transition in the turbulence boundary layer, is also introduced to include the influence of the transition flow. For deep-stall conditions, attached flow only exists in a very small area near the edges, so the influence of the transition under large-α conditions is not studied. For the two-dimensional simulation case with $\alpha = 20°$ as an example, the transition on the suction side happens very close to the leading edge, as shown in Figure 8. The transition model mainly influences the turbulence on the pressure side. By comparing the time-averaged pressure and wall shear stress, it can be summarized that simulations without the transition model may underestimate C_L by 0.3% and C_D by 3.5%. However, because F_D is relatively much lower (normally less than 10%) than F_L for small-α conditions, the influence of the transition flow on the propulsive performance can be ignored. Moreover, the transition model substantially slows down the simulation speed because an extra equation needs to be solved, so the transition model is not applied in this study.

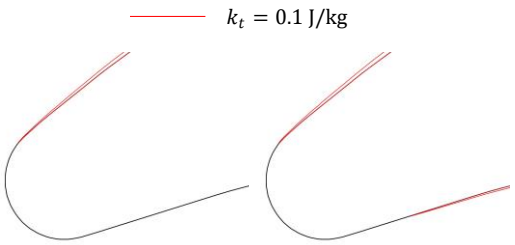

(a) With transition . (b) Without transition .

Figure 8. Isoline of $k_t = 0.1$ J/kg around the leading edge.

2.2.4 Solver and discretization schemes

A finite volume method is utilized to discretize the governing equations. The method employs a segregated flow solver that is accomplished with the semi-implicit method for the pressure-linked equations (SIMPLE) algorithm (Patankar, 1980). The flow is assumed to be incompressible in this study because of the low freestream Mach number.

The convection fluxes on cell faces are discretized by means of a hybrid second-order upwind and bounded-central scheme. The diffusion fluxes on both internal and boundary cell faces are discretized with a second-order scheme. The second-order hybrid Gauss-LSQ method is

used in gradient computation, which involves the reconstruction of the field values in a cell face, such as the secondary gradients of the diffusion fluxes and the pressure gradients, as well as the rate-of-strain tensors used in turbulence models. A second-order implicit method is applied to discretize the time derivative. The time-marching procedure adopts iterations within each time step.

2.3 Numerical mesh

2.3.1 Mesh typology

Unstructured meshes with a trimmed cell topology are mainly used for the simulations. Figure 9 shows the mesh of the three-dimensional simulation with a freestream tip and symmetric bottom, together with typical cell sizes. The cells have a uniform size in each region at each refinement level. The region near the foil and the wake region are both refined, which can be seen in the section plane of $Z = 0.5H$ in Figure 9(b). The mesh in the wake region is refined by two parameters: the length and the separate angle of the wake refinement. A cylindrical volumetric mesh refinement with a length of $1.1H$ is introduced for refining the mesh near the foil. The diameter of the cylinder is 20 m. Flow separation points are expected to distribute around the two edges, so similarly, a more refined set of meshing is applied to the region near the edges of the foil to capture the flow separation phenomena, as Figure 9(c) shows. The refinement, except for the prism layer, is based on the base size, called l_{base}, in Figure 9.

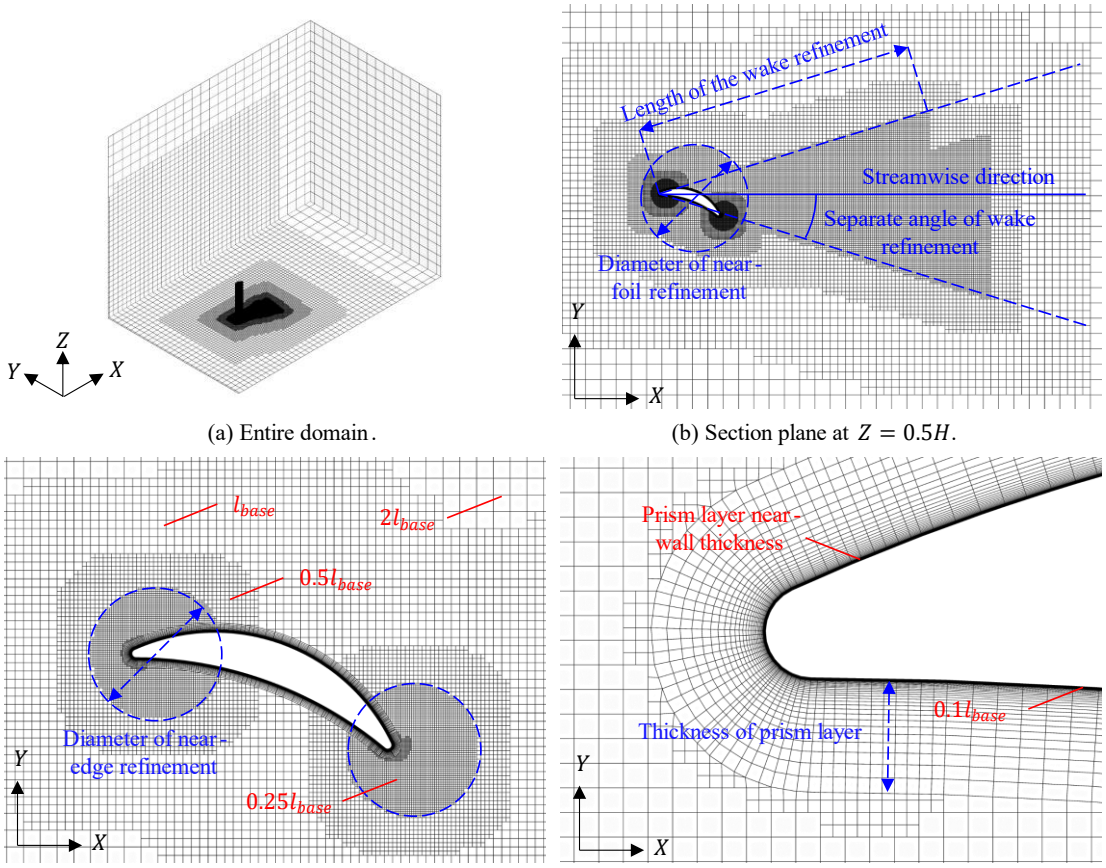

(a) Entire domain.

(b) Section plane at $Z = 0.5H$.

(c) Attached region near the foil, at the section plane of (b).

(d) Attached region near the leading edge, at the section plane of (b).

Figure 9. Three-dimensional trimmed mesh at $\alpha = 20°$.

Prism layers are generated near the wall of the foil to resolve the flow in the boundary layers, as shown in Figure 9(d). The absolute total thickness of the prism layer is 0.5 m, and the number of prism layers is 55 for all the simulation cases. Because the crescent-shaped profile has a quite large camber, a strong flow separation is expected. Thus, it is desired that y^+ of the first-layer cells near the wall is less than 1 to achieve a more detailed and accurate study of the boundary layer flow. In the simulation cases, the order of magnitude of y^+ is around 10^{-1} on most areas of the wall. To obtain this low y^+ value, the near-wall thickness of the prism layer is set to an absolute value of 1×10^{-5} m, which does not change during global mesh refinement.

Polyhedral meshes are also used to cross-compare with the trimmed meshes described above. By following the same refinement strategy, which means having consistently refined regions, the polyhedral mesh is

generated as shown in Figure 10. Compared with the trimmed mesh, the cell sizes develop smoothly in the polyhedral mesh. The impact of mesh typology is discussed in Section 2.3.3.

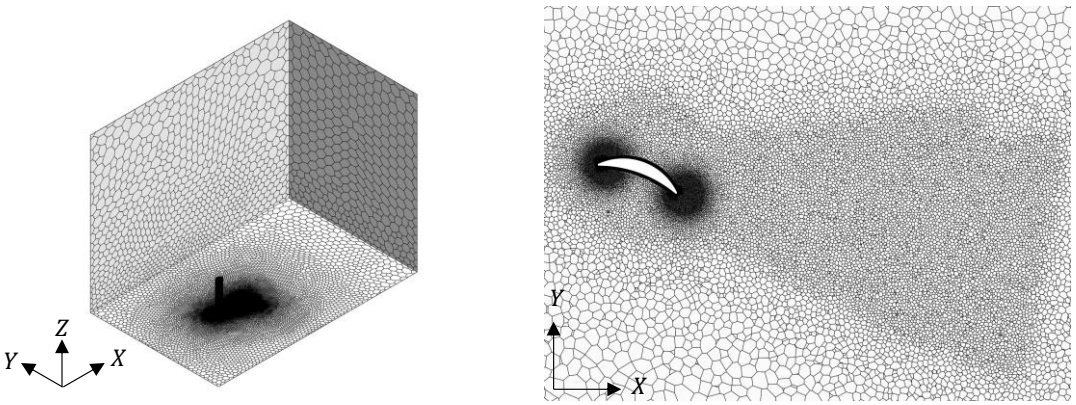

(a) Entire domain. (b) Section plane at $Z = 0.5H$.

Figure 10. Three-dimensional polyhedral mesh when $\alpha = 20°$.

As shown in Figure 3, when θ_{AW} is larger than 90°, the wingsail operates with a high α. When θ_{AW} is around 180° (i.e., the downwind condition), F_D is mainly used as the thrust for propulsion. Two-dimensional and three-dimensional simulations are performed for deep-stall conditions, for example, the condition when $\alpha = 90°$. Under deep-stall conditions, von Kármán vortex streets are expected to spread for a quite long distance in the downstream areas, so an extra downstream refinement for the downstream areas is introduced when $\alpha \geq 35°$ (Figure 11).

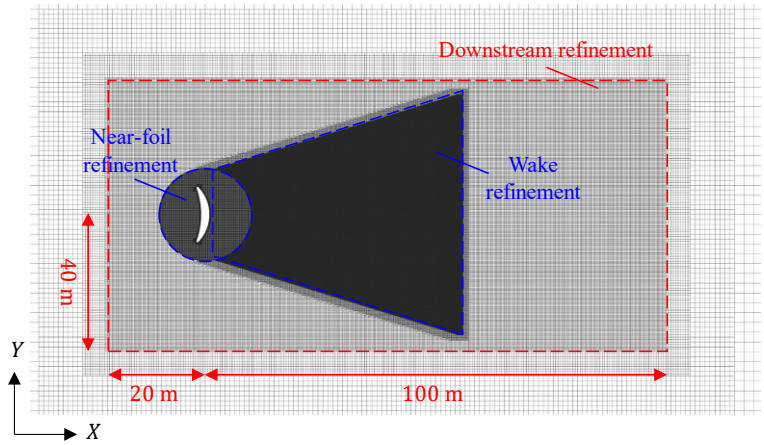

Figure 11. Two-dimensional trimmed mesh for deep-stall conditions ($\alpha = 90°$).

2.3.2 Two-dimensional mesh independence

Two-dimensional mesh independence studies are carried out by considering two aspects: the refinement strategy and the size of the cells.

Regarding the refinement strategy, three factors (the existence of the near-foil refinement, the length, and the separate angle of the wake refinement) are studied to ensure that the mesh quality is sufficient to obtain converged CFD results. The time-averaged values, as well as the oscillating amplitudes of C_L and C_D, are regarded as indicators of the mesh resolution independence. The base size (l_{base} in Figure 9) for these cases is 0.5 m. Figure 12(a) shows the results based on the mesh without near-foil refinement with different separate angles of wake refinement. The length of wake refinement is fixed at 60 m. When the separate angle is larger than 0.3 rad, the values of the force coefficients converge. Similarly, by fixing the separate angle of wake refinement at 0.3 rad, a few sets of mesh with different lengths of wake refinement are studied, as shown in Figure 12(b), indicating that the length of wake refinement should be longer than 60 m to exclude the influence of the mesh. Figure 12(c) shows the effects of near-foil refinement based on a series of mesh sets having a 0.3 rad separate angle of wake refinement. The near-foil refinement does not considerably increase the total number of cells. Although the effects on C_L and C_D are not obvious, this local refinement is retained in subsequent studies to reduce the mesh change when

variating the angle of attack. In summary, the mesh follows the strategy of having wake refinement with 0.3 rad in a separate angle and 60 m in length, as well as near-foil refinement.

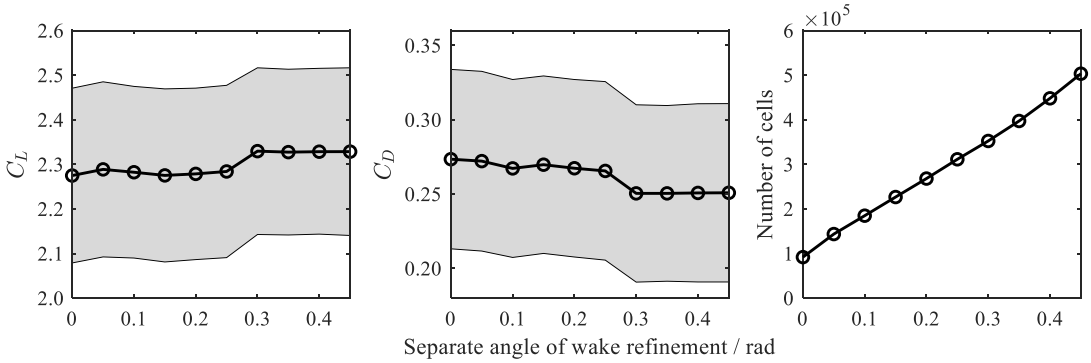

(a) Different separate angles of wake refinement.

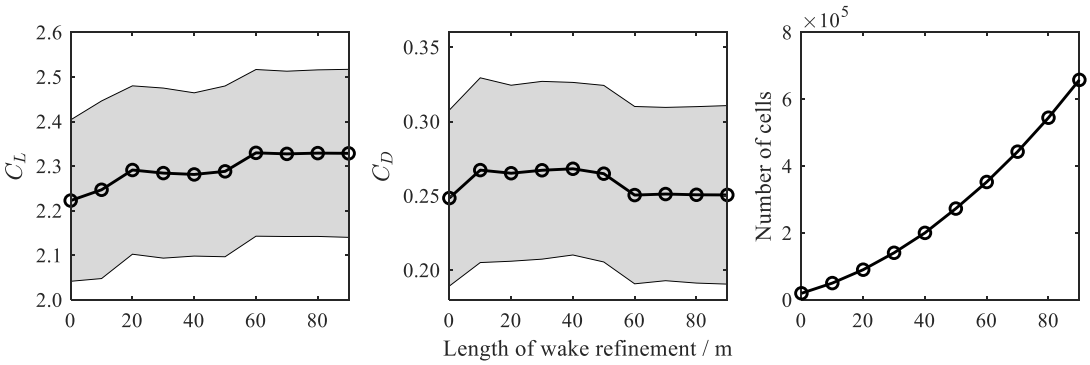

(b) Different lengths of wake refinement.

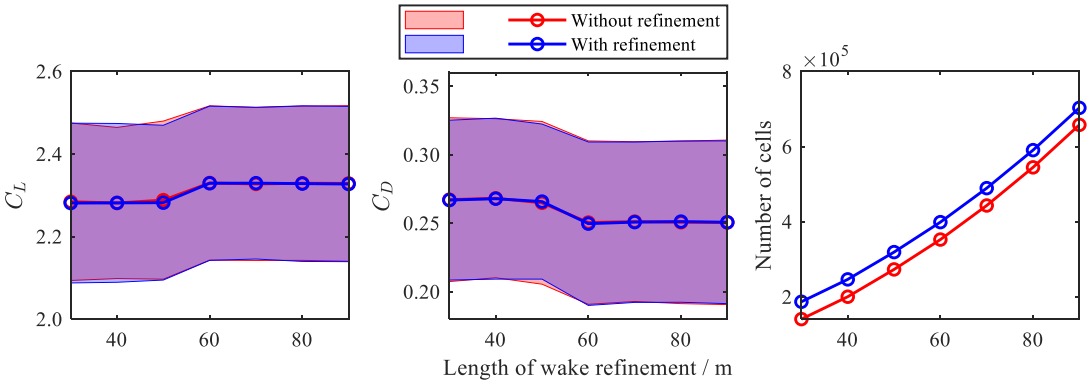

(c) With or without near-foil refinement and different lengths of wake refinement.

Figure 12. Two-dimensional mesh independence study based on different refinement strategies.

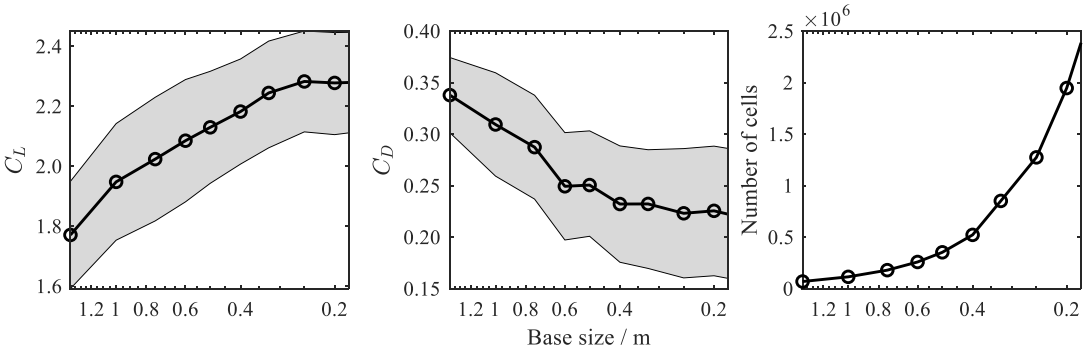

Figure 13. Two-dimensional mesh independence study based on different base sizes.

By following a certain refinement strategy, two-dimensional simulations with different base sizes are carried out. The variation of the base size affects the entire mesh, except for the prism layer mesh in the

normal direction. As shown in Figure 13, when the base size is smaller than 0.35 m, the difference in the force coefficients from the two most refined cases is lower than 1% for C_L and 4% for C_D. Because C_D is only around 8% of C_L, the thrust force is mainly based on the lift. Because of the limitation of two-dimensional simulations, in which the flow separation cannot be well-resolved, the two-dimensional mesh independence study does not go deeper.

2.3.3 Three-dimensional mesh independence

A series of three-dimensional meshes are generated based on the same refinement strategy. To study the three-dimensional mesh independence, five sets of mesh are generated. For a convenient description, the five sets of mesh are numbered from 1 to 5, from the coarsest to the finest. Regarding the force coefficients, the results from mesh 3, mesh 4, and mesh 5 are similar (Figure 14). Between mesh 3 and mesh 5, the difference of C_L is 0.37%, and the difference of C_D is 0.36%. Thus, it can be concluded that when the mesh is more refined than mesh 3, the simulation results are irrelevant to the mesh. The number of cells in mesh 3 is 23,735,358. The following three-dimensional simulation results are all based on mesh 3.

As mentioned in Section 2.3.1, another three-dimensional simulation based on a polyhedral mesh with a similar total number of cells is also performed to exclude the influence of mesh typology. The differences between the force coefficients of the two types of mesh are under 1%, so it can be concluded that mesh typology does not affect the simulation results.

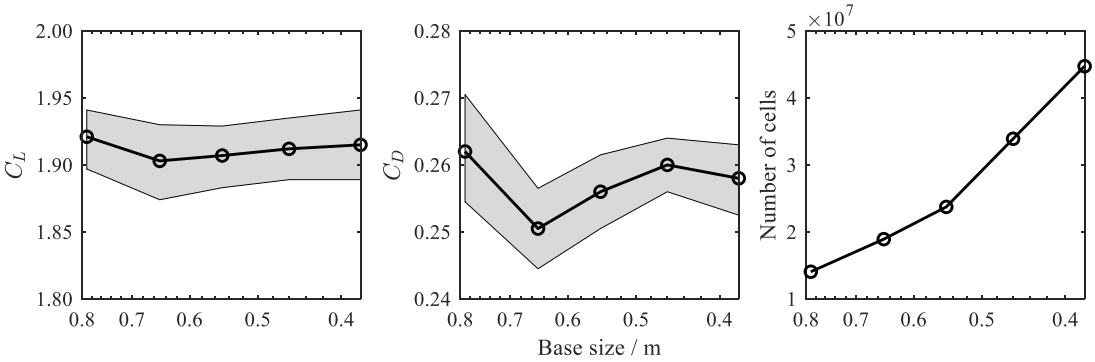

Figure 14. Three-dimensional mesh independence study based on different base sizes.

2.4 Performance evaluation

Predicting the performance of a wind-assisted ship propulsion system requires the inclusion of the full system (i.e., the sails and the ship). F_S and the yaw moments introduced by the wind-assisted ship propulsion systems must be compensated by a drift of the ship and a rudder angle, both of which introduce added resistance, causing both a lower net thrust (i.e., the thrust of the sail minus the added resistance caused by the sail) and the need for sail trim optimization to achieve the best performance under any given constraints (e.g., the effects of the rudder or heel angle). Thus, a model respecting at least four degrees of freedom (i.e., surge, drift, yaw, and heel) must be used. Furthermore, the performance of a wind-assisted ship propulsion system also depends on the ship it is installed on, which means that any performance or comparison study must involve a case study ship. Here, a tanker with a deadweight of approximately 100,000 tons is used (the ship's dimensions are given in Table 2).

ShipCLEAN is used as a performance prediction tool in this study. ShipCLEAN is a generic model developed to provide accurate predictions with very little input data, respecting four degrees of freedom. The development, applicability, and achievable accuracy of ShipCLEAN have been documented in numerous publications (e.g., Tillig and Ringsberg (Tillig and Ringsberg 2019) and Tillig and Ringsberg (Tillig and Ringsberg 2020)).

Table 2. Main dimensions of the case study ship.

Main dimension	Value	Unit
L_{oa}	228.6	m
B	42.0	m
T_{design}	15	m
Δ at T_{design}	123,000	t
Design speed	14.8	kn

In general, the ShipCLEAN model consists of two parts: a classic one-degree-of-freedom power prediction that includes several methods to evaluate missing dimensions, and a four-degrees-of-freedom dynamic portion that includes all effects of variable environmental conditions and includes methods for sail trim optimization. The achievable accuracy of the power prediction was demonstrated by Tillig et al. (Tillig et al. 2018) and the uncertainties in the prediction of sail forces and aero- and hydrodynamic interactions were

discussed by Thies and Ringsberg (Thies and Ringsberg 2022).

3. Results and discussion

3.1 Loads on the sail

3.1.1 Force coefficients

According to the wind tunnel tests (Sheldahl & Klimas, 1981), when the Reynolds number is 1×10^7, the critical angle of attack, α_c, of the NACA 0015 foil is approximately 16°, and the maximum C_L is around 1.42. A previous study (Nikmanesh, 2021) indicated that, for the newly introduced crescent-shaped profile, α_c is around 20°. The following comparison between two- and three-dimensional simulations, as well as the comparison between different boundary conditions, are based on α_c (i.e., the angle of attack is 16° for the NACA 0015 foil and 20° for the crescent-shaped foil).

For the crescent-shaped foil, in the view of force coefficients, by comparing two- and three-dimensional simulations having periodic top and bottom, the differences in between are separately 7.5% for C_L and 58.1% for C_D, as Figure 15 presents. This suggests that two-dimensional simulations substantially overestimate the force coefficients even under low-α conditions and C_D is more sensitive than C_L. In two-dimensional simulations, because of the limitation of the spanwise flow, the vortices are constrained and not well-developed (Park et al., 2017). Overestimation of force coefficients, especially C_D, was also found by similar research performing high-Reynolds-number CFD simulations for airfoils with strong flow separation (Zhu, 2020). By comparing the results from different boundary conditions, it can be determined that these two cases provide force coefficients with obvious differences. When there is a freestream tip, the lift force on the foil decreases by 5.7% and the drag force increases by 35.0%.

As Figure 15 shows, the crescent-shaped profile has substantially higher force coefficients and is expected to provide better propulsive performance. Moreover, because of tip vortices, the reduction of C_L for the wingsail with the crescent-shaped profile is 5.7%, while the value is 10.7% for the sail with the NACA 0015 profile. Therefore, the effects of the tip vortices on the crescent-shaped concept are not as substantial as those on the NACA 0015 wingsail. On the other hand, because of flow separation, which is discussed in Section 3.2.1, the crescent-shaped wingsail shows remarkable oscillation amplitude of the force coefficients. Therefore, the crescent-shaped sail is believed to suffer from more serious flutter, which increases the requirements of the sail structure.

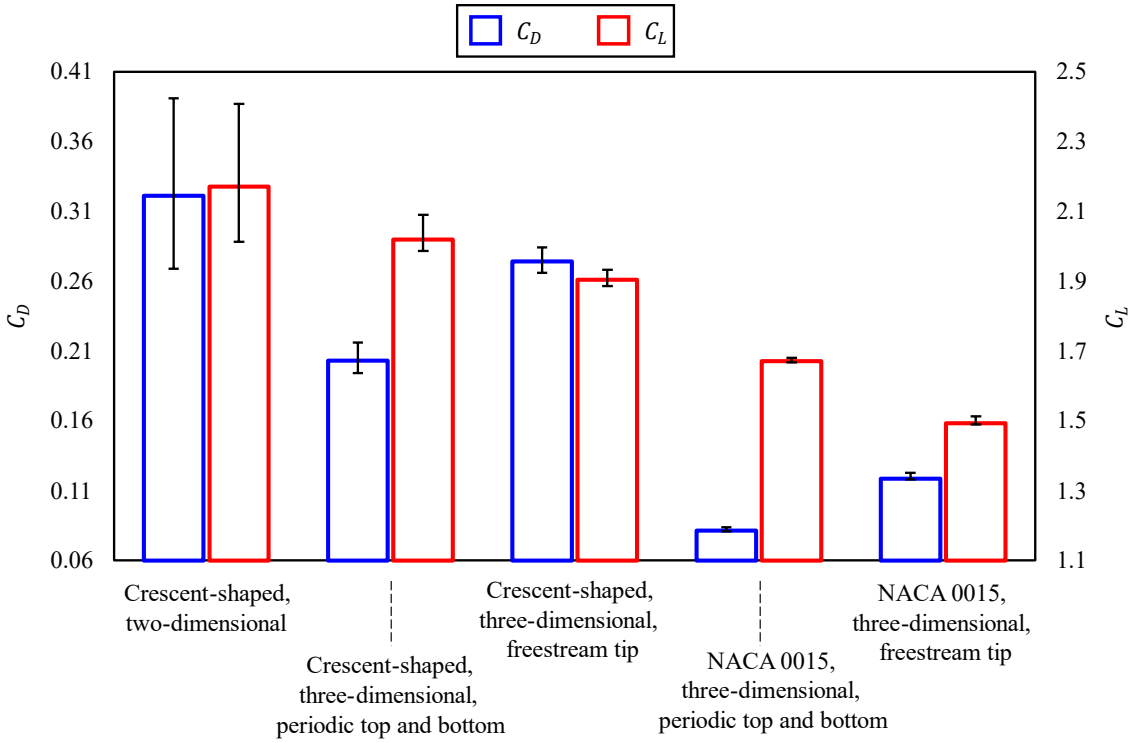

Figure 15. Force coefficients of NACA 0015 and crescent-shaped foils from two- and three-dimensional simulations with different boundary conditions. The error bars represent the amplitude of oscillation.

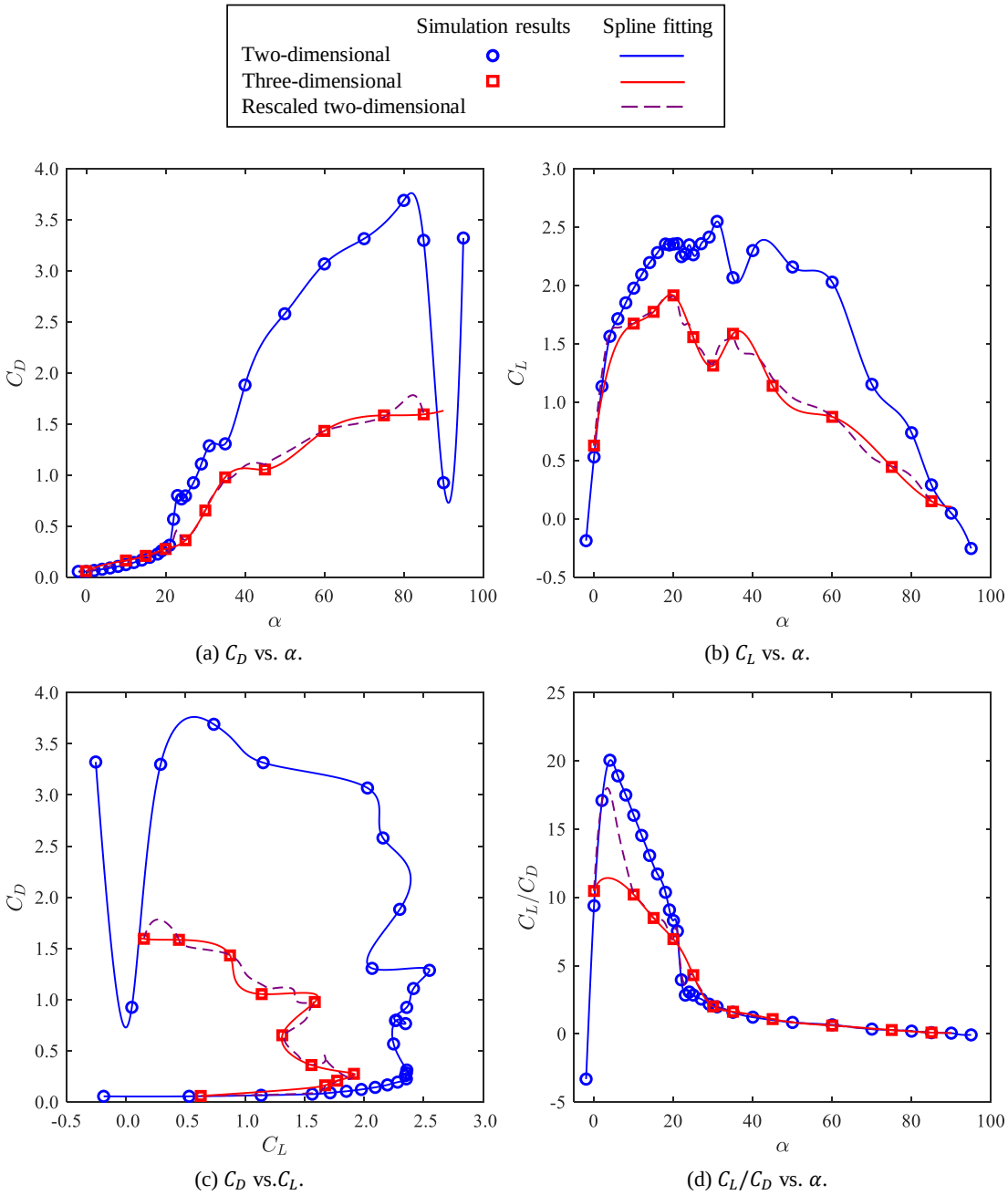

(a) C_D vs. α.

(b) C_L vs. α.

(c) C_D vs.C_L.

(d) C_L/C_D vs. α.

Figure 16. Time-averaged C_L and C_D curves.

To analyze the propulsive performance of the wingsail under various wind conditions (i.e., a large range of wind directions), for the newly introduced crescent-shaped foil, a series of two-dimensional simulations with α from $-2°$ to $95°$ are performed to determine α_c, and 12 three-dimensional simulations are performed with different α. The plots of the force coefficients are displayed in Figure 16, where blue lines and symbols represent the two-dimensional results and red lines and symbols represent the three-dimensional results.

Figure 16(a) reveals that there is no clear α_c for this kind of profile. Two peaks of C_L occur when $\alpha = 20°$ and $\alpha = 35°$. The highest C_L is approximately 2.7 when $\alpha = 35°$ based on two-dimensional simulations, and 1.9 when $\alpha = 20°$ based on three-dimensional simulations. As for C_D, both two-dimensional and three-dimensional simulations show that when $\alpha \leq 80°$, C_D increases as α increases (Figure 16(b)). Two-dimensional simulations predict much higher C_D than three-dimensional simulations, and a similar phenomenon was also detected by other researchers (Najjar & Vanka, 1995). According to the two-dimensional simulations, the highest C_D is around 3.7 when $\alpha = 80°$. For high-Re conditions, C_D for a flat plate is approximately 1.98, and for a semicircle opening upstream, it is approximately 2.30 (Hoerner, 1976). The C_D of the crescent-shaped profile should probably in between. Moreover, because of the tip vortices, C_D is expected to be even lower, so the predicted C_D is unreasonably high. In addition, C_D suddenly decreases when α increases from $80°$ to $90°$ in the two-dimensional simulations. Inferring from these

unreasonable facts, it is believed that the two-dimensional simulations cannot provide reasonable predictions of the force coefficients when $\alpha > 20°$ because of the strong flow separation, which will be explained in Sections 3.1.2 and 3.2.1.

3.1.2 Pressure distributions

Figure 17 presents the time-averaged pressure coefficient distribution along the surface of the profile. Because of the large camber of the crescent-shaped profile, the pressure difference between the pressure side and the suction side is obvious even when $\alpha = 0°$, as shown in Figure 17(a).

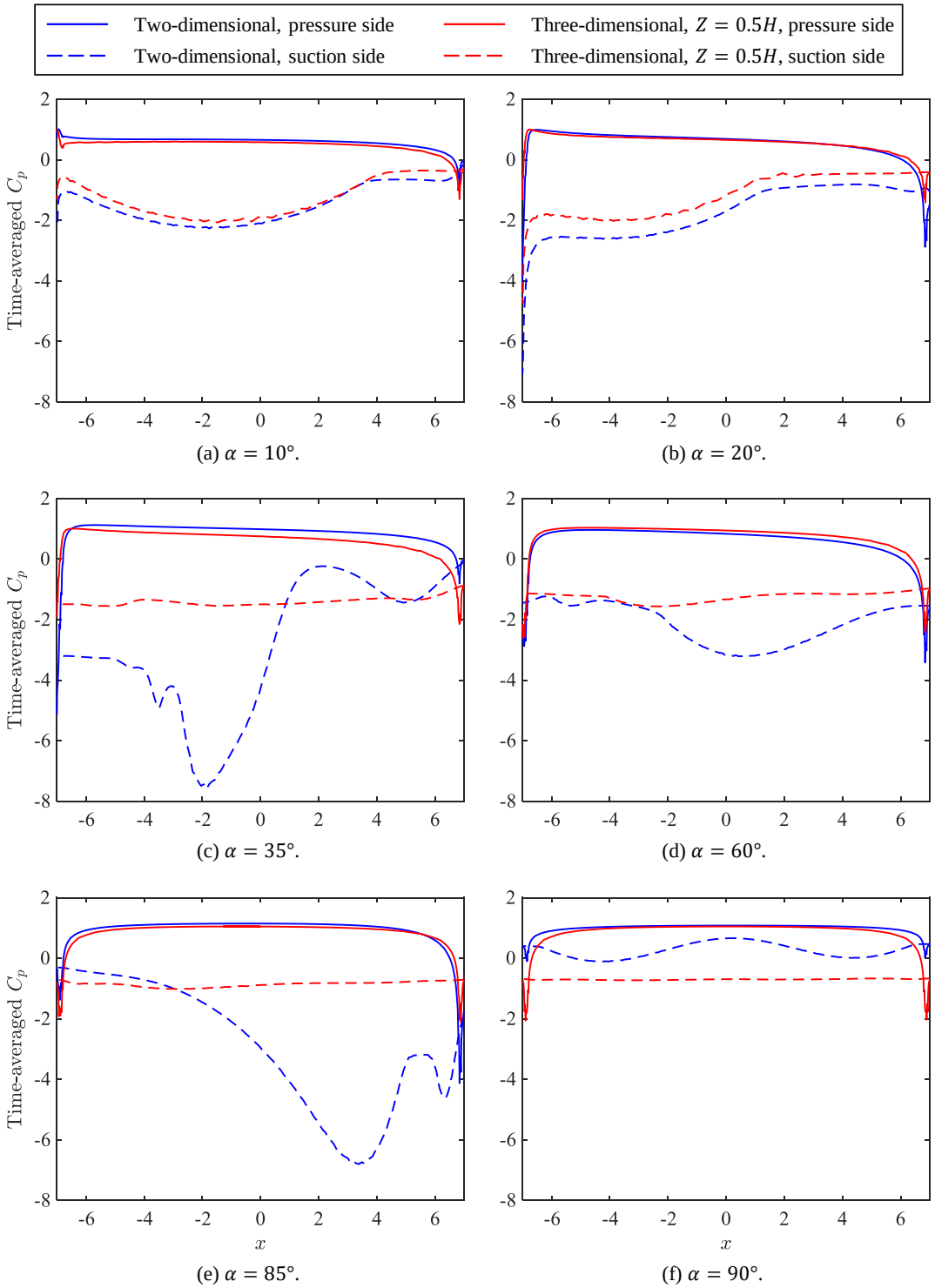

(a) $\alpha = 10°$. (b) $\alpha = 20°$.

(c) $\alpha = 35°$. (d) $\alpha = 60°$.

(e) $\alpha = 85°$. (f) $\alpha = 90°$.

Figure 17. Time-averaged C_p distribution along the wall with different α. Three-dimensional results are based on the condition with a freestream tip.

When $\alpha \leq 20°$, two-dimensional and three-dimensional simulations provide similar predictions of the pressure distribution. According to the three-dimensional simulations, the highest C_L is obtained when

$\alpha = 20°$. As Figure 17(b) shows, the leading part of the profile (i.e., the upstream half) mainly contributes to generating the lift force because C_p is quite low, which results in a large pressure difference. In addition, around the trailing edge (the chord-wise location is around 7 m), the wall pressure at the pressure side becomes lower than that at the suction side. This inversion of wall pressure probably has negative effects on the lift force coefficient, and the shape of the edges is expected to be optimized in the future.

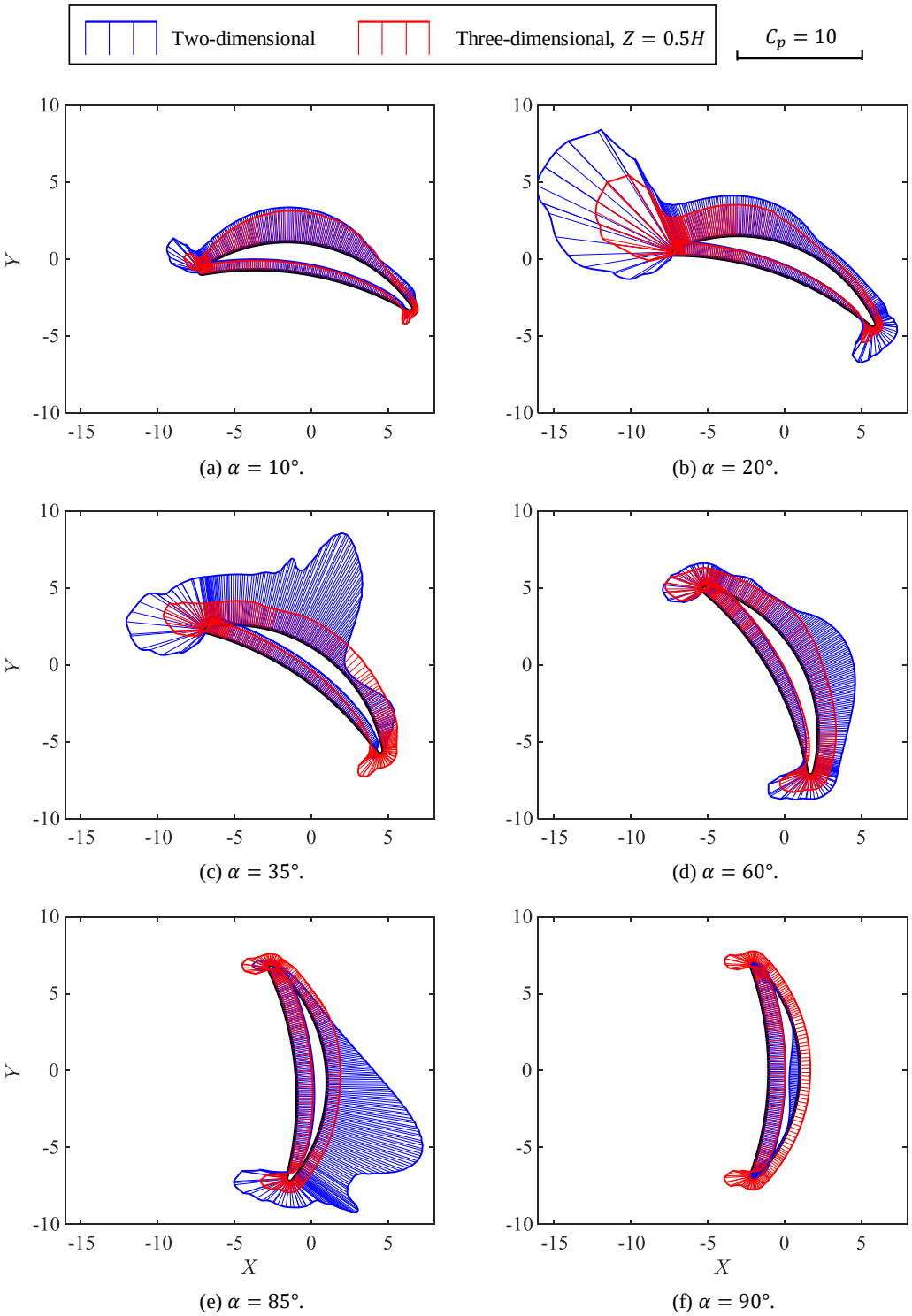

(a) $\alpha = 10°$. (b) $\alpha = 20°$.

(c) $\alpha = 35°$. (d) $\alpha = 60°$.

(e) $\alpha = 85°$. (f) $\alpha = 90°$.

Figure 18. Time-averaged pressure coefficient distribution over the crescent-shaped profile. The inlet flow velocity is in the positive X direction.

However, when α is large (e.g., $\alpha = 35°$, as shown in Figure 17(c)), the two-dimensional and three-dimensional results are quite different. Based on two-dimensional simulations, the pressure on the suction side is unreasonably low, leading to unreasonably high force coefficients. Similar phenomena can also be found when

α is 60° (Figure 17(d)) and 85° (Figure 17(e)). Nevertheless, one exception is that when $\alpha = 90°$ (i.e., the chord line is perpendicular to the inlet flow velocity), the suction-side pressure predicted by the two-dimension simulations is even higher than that based on the three-dimensional simulations. In the two-dimensional results, positive C_p is widely distributed on the suction side. This strange phenomenon is regarded as the reason for the sudden decrease in C_D in Figure 16(a).

In Figure 18, the vectors of the time-averaged wall pressure coefficient are presented. For low α conditions, for example $\alpha = 20°$ (Figure 18(b)), a quite strong suction force can be found on the suction side close to the leading edge. Since the normal direction of the wall surface in this area is close to the positive Y direction, this suction force efficiently contributes to the lift force. The crescent-shaped profile has a sharp leading edge and a blunt trailing edge compared with conventional airfoils. Thus, C_p is very high at the leading edge and negative C_p occurs at the pressure side when approaching to the trailing edge. To improve the propulsive performance of wingsails with crescent-shaped profiles, the shape of the edges should be optimized. On the other hand, the concept of this crescent-shaped profile is symmetric about the mid-chord to facilitate the operation of the wingsail, so optimization of the aerodynamic performance of the edges should be multi-objective to give consideration to both edges.

3.2 Characteristics of the flow field

3.2.1 Flow separation

Figure 19 presents the wall shear stress distribution along the wall surface of the sectional profile with different α. Figure 20 and Figure 21 show the flow field around the sectional profile with different α according to the two-dimensional and three-dimensional results, respectively. The areas in red represent the region where $V_X > V_{AW}$, which means that the streamwise velocity is higher than the inlet flow velocity, whereas those in blue represent the region with $V_X < V_{Aw}$.

One of the most important characteristics of the flow field is the remarkable flow separation. For NACA 0015, there is usually none to one flow separation point depending on α. The characteristic of flow separation does not appear if α is lower than the critical angle of attack. However, for the flow field generated by the crescent-shaped foil, flow separation always happens, even if $\alpha = 0°$ (see Figure 20(a) and Figure 21(a)). Flow separation happens on the suction side close to the trailing edge and also on the pressure side close to the leading edge. A large region with low velocity or even reversed flow appears attached to the pressure side. In Figure 19(a), where $\alpha = 10°$, the positive and negative of wall shear stress converses, which indicates that flow separation happens. When $\alpha = 20°$, a high-velocity area occurs near the suction side, causing low pressure and then leading to multiple flow separation points on the downstream half of the profile, as shown in Figure 19(b). When flow separation happens in the boundary layer, a shear layer and the presence of a separated flow region between the shear layer and surface are formed, which modifies pressure distribution. Flow separation is thought to result in an increase in pressure drag.

When $\alpha \leq 20°$, the flow field predicted by the two-dimensional and three-dimensional simulations show some similarities. However, for large α conditions, two-dimensional and three-dimensional simulations provide totally different results. Take the pair of simulation cases with $\alpha = 35°$ as an example. In the two-dimensional results, the vortices are strong, but in the three-dimensional results, vortices are hard to recognize. In Figure 20(d) and Figure 20(e), where α are separately 25° and 35° for the two-dimensional simulations, a high-velocity reversed flow region can be seen next to the suction side. This high-velocity region causes low pressure, leading to a strong lift force. It is regarded as the main mechanism for the peak of C_L in Figure 16(b). However, this phenomenon does not happen in the three-dimensional results (Figure 21(d) and Figure 21(e)), where V_X still shows positive values in the area attached to the suction side, which explains why the peak of C_L at $\alpha = 35°$ is not as notable as in the two-dimensional results.

For deep-stall conditions (i.e., $\alpha \geq 60°$), an obvious von Kármán vortex street is observed in the wake region of the two-dimensional simulations, especially when α is close to 90°. A similar phenomenon was observed in some other studies regarding deep stall foils. For example, Park et al. (Park et al. 2017) studied a three-dimensional NACA 0021 airfoil with $\alpha = 60°$ and different aspect ratios, and Zhu (Zhu 2020) performed two-dimensional and three-dimensional CFD simulations on NACA 0015 airfoil with $\alpha = 90°$. These strong vortices are considered the main reason for the extremely high C_D in Figure 16. Because of vortex shedding, high-velocity flow happens next to the suction side of the wingsail profile, which results in low pressure on the suction side. Except for the condition with $\alpha = 90°$, the vortices generated on the leading edge and the trailing edge is not equally strong. Vortices generated by the leading edge are much stronger when $\alpha = 35°$ (see Figure 20(e)), whereas vortices generated by the trailing edge are much stronger when $\alpha = 85°$ (see Figure 20(g)). These differences cause the uneven distribution of C_p on the suction side in Figure 17 and Figure 18 (the blue lines and shadows represent the two-dimensional results).

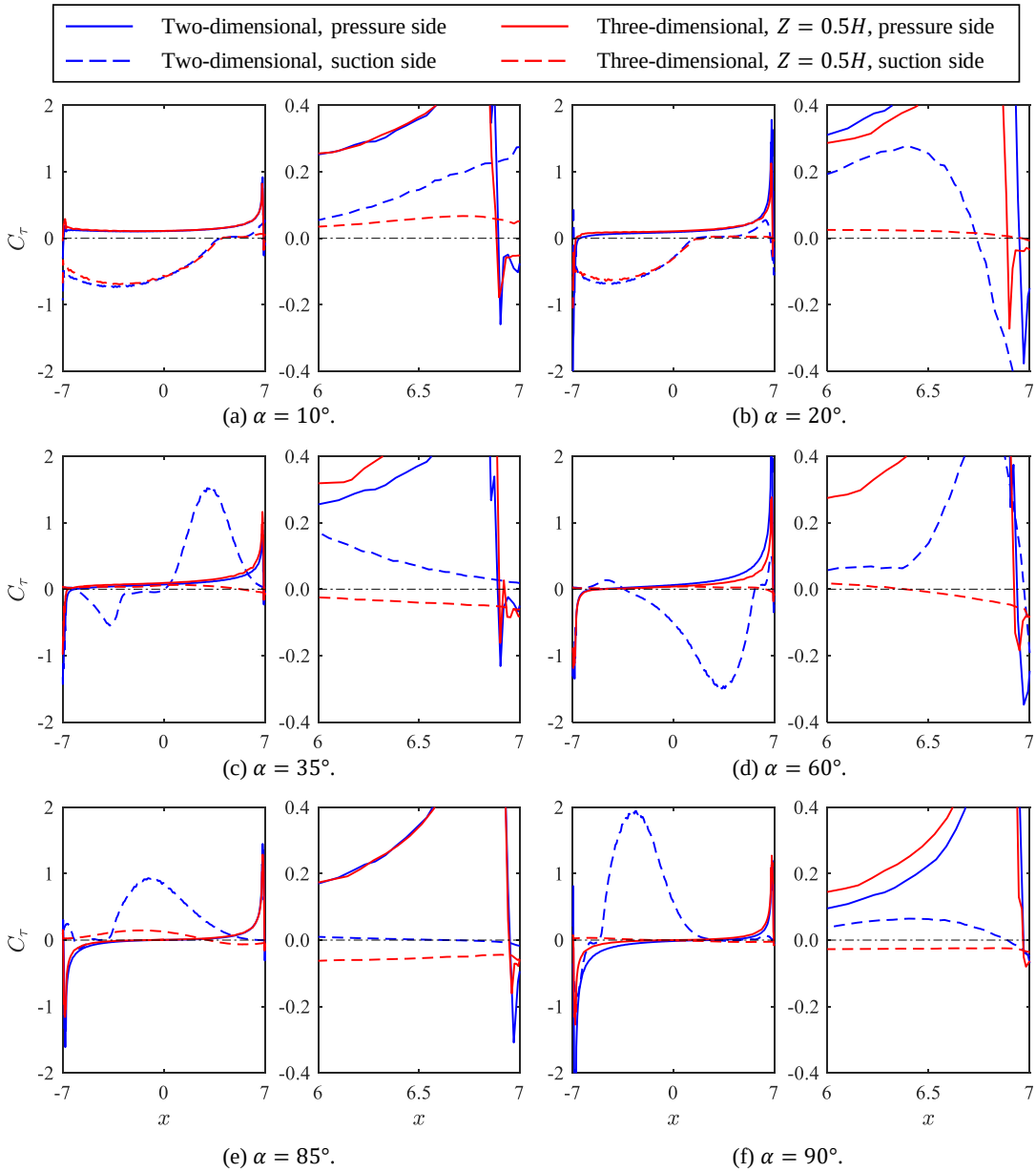

Figure 19. Wall shear stress coefficient distribution along the wall of the wingsail. For each subfigure, left: entire profile; right: near the trailing edge.

However, three-dimensional simulations provide different results. Take the condition of $\alpha = 85°$ (Figure 20(g) and Figure 21(g)) as an example. In the obtained three-dimensional results, the flow that is close to the suction side is almost quiescent with very low velocity. Similar flow characteristics were recorded by relative studies. For instance, Castelli et al. (Castelli et al. 2012) used numerical simulations to study a flat plate with $\alpha = 90°$, and also found large low-velocity areas in the wake. This finding explains why the C_p on the suction side, predicted by the three-dimensional simulations, is much higher than that based on two-dimensional simulations. In addition, in Figure 20(g) and Figure 21(h), not only the downstream field but also the upstream field is influenced by the wingsail profile. V_X is always lower than V_{AW} around the crescent-shaped profile. Hence, it can be inferred that when the wingsail is operated under $\alpha \approx 90°$ (i.e., under downwind conditions), the interaction among multiple wingsails might be considerable, which can be analyzed in future studies. From the iso-surface plot in Figure 22, where colorful contours represent the streamwise vorticity, circular patterns of rotating air left behind the tip of the foil, which are the tip vortices, can be easily recognized (see Figure 22(a) and Figure 22(c)). Tip vortices cause a reduction of C_L, which is discussed in Section 3.2.2. Wingsails with different section profiles show different wake characteristics. For the crescent-shaped profile, vortex shedding is much more substantial. Numerous vortex tubes can be seen in the wake region (Figure 22(a) and Figure 22(b)). However, for the NACA 0015 profile (see Figure 22(c) and Figure 22(d)), only limited vortex

tubes can be seen developing on the suction side. Vortex shedding is regarded as the main reason resulting in the oscillation of force coefficients. Thus, the oscillation of force coefficients of the crescent-shaped wingsail is much stronger than that of the wingsail with the NACA 0015 profile.

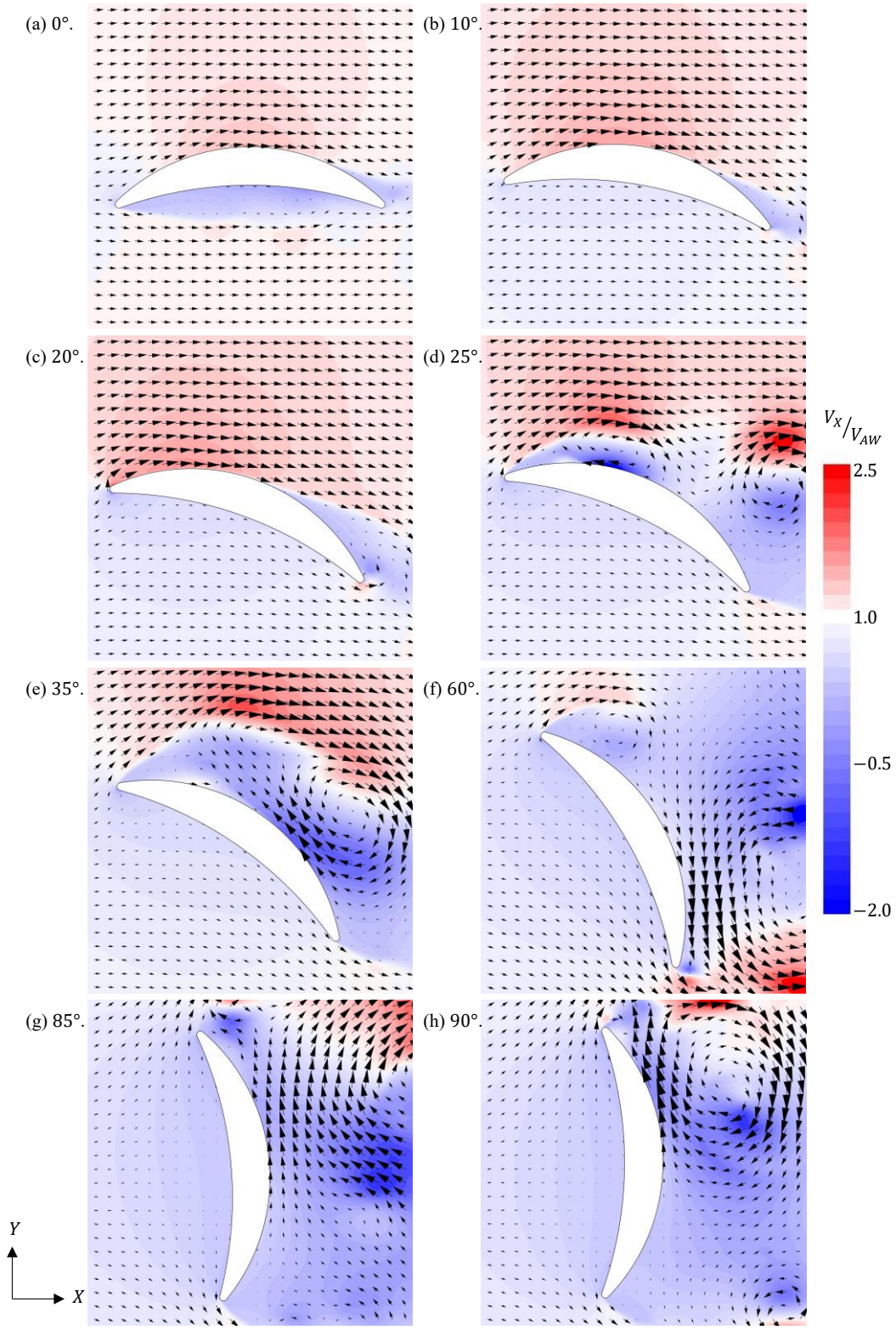

Figure 20. V_X distribution and velocity direction vectors around the foil from two-dimensional simulations with different α. The inlet flow velocity is in the positive X direction.

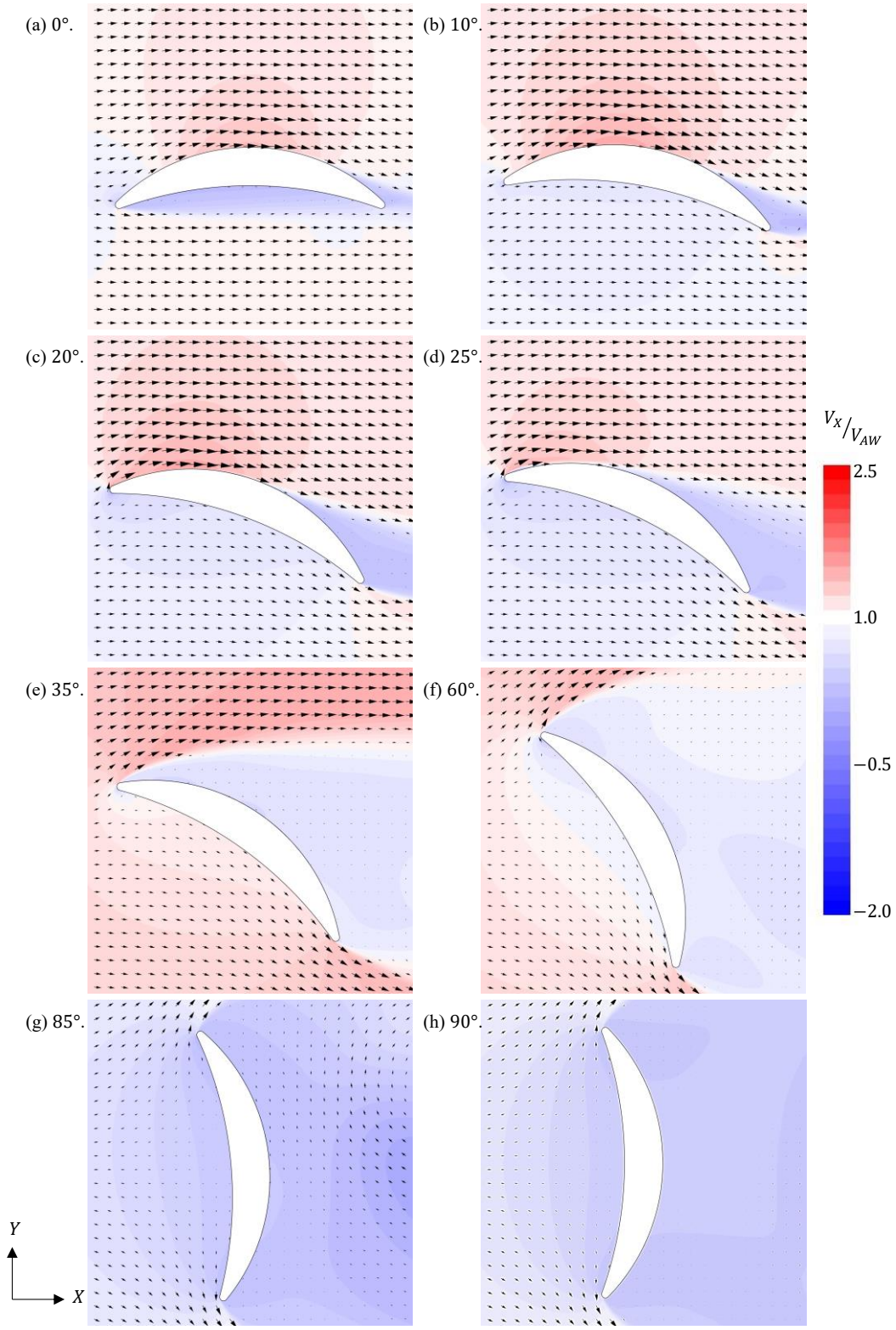

Figure 21. V_X distribution and velocity direction vectors around the foil from three-dimensional simulations with different α. $Z = 0.5H$. The inlet flow velocity is in the positive X direction.

For the crescent-shaped profile, vortex shedding is obvious in the downstream region of the suction side and the trailing edge for simulations with both kinds of boundary conditions. However, in the downstream flow field, the structure of the vortex tubes is much more complex when the top and bottom boundaries are periodic. In Figure 22(a), excluding the tip vortices, the vertical vortex tubes are uniform and can be easily recognized. Nevertheless, when the top and bottom boundaries are periodic (Figure 22(b)), because of the constrain of the top and bottom boundaries, many horizontal vortex tubes can be seen. A similar phenomenon is also found in the NACA 0015 profile. This phenomenon explains the larger oscillation amplitude of the force coefficients.

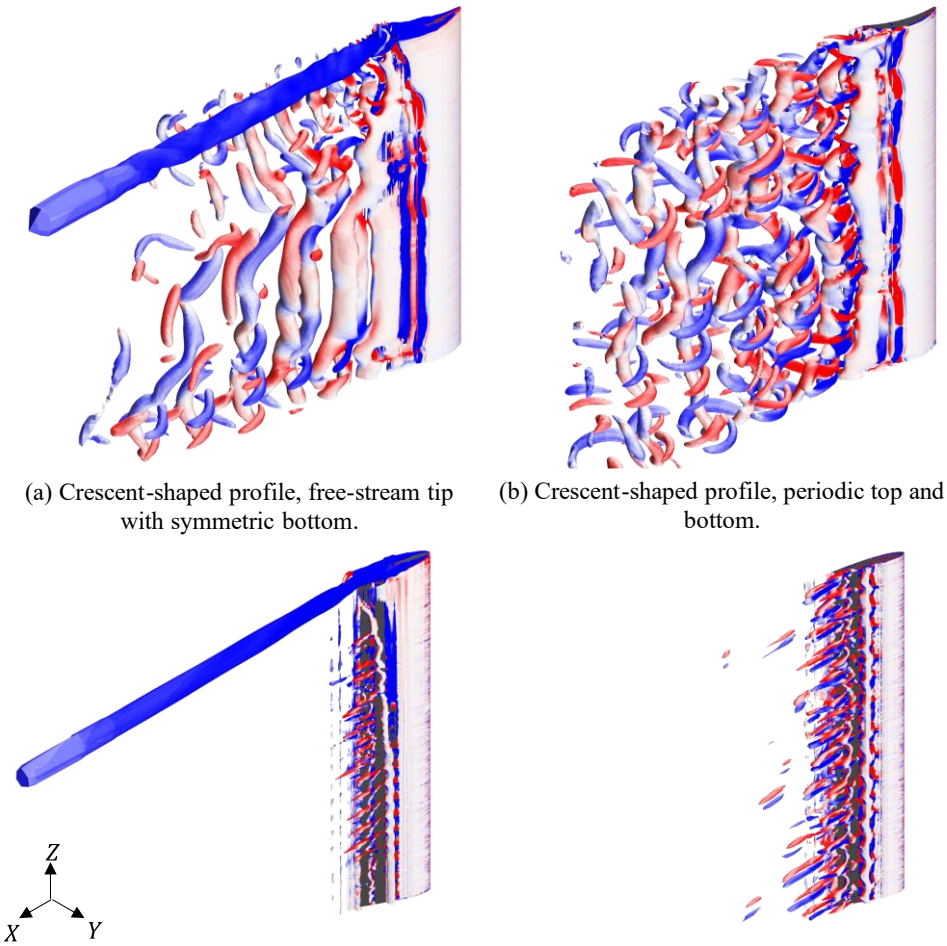

(a) Crescent-shaped profile, free-stream tip with symmetric bottom.

(b) Crescent-shaped profile, periodic top and bottom.

(c) NACA 0015, freestream tip with symmetric bottom.

(d) NACA 0015, periodic top and bottom.

Figure 22. Iso-surfaces of $Q = 5\ \mathrm{s}^{-2}$, colored with ω_X. $\alpha = 20°$ for the crescent-shaped profile and $\alpha = 16°$ for NACA 0015. The inlet flow velocity is in the positive X direction.

3.2.2 Tip vortices

Another important characteristic of the flow field is the phenomenon of tip vortices, which is believed to be the main reason for the lift reduction when the boundary conditions are changed from periodic top and bottom to free tip and symmetric bottom. Figure 23 presents the time-averaged wall pressure distribution at various section planes. When the top and bottom have periodic boundary conditions (Figure 23(b)), the pressure distribution along the foil is similar at different Z positions. For instance, the wall pressure distribution at the section planes of $Z = 0.25H$ and $Z = 0.95H$ does not show obvious differences. However, if the boundary condition is a free tip and symmetric bottom (Figure 23(a)), the pressure difference between the pressure side and the suction side becomes smaller when approaching the tip of the wingsail, leading to a lift reduction.

From the streamline plot in Figure 24, where the color represents the spanwise velocity, it can be found that there is flow going around the tip from the pressure side to the suction side. The vortices can be obviously seen over the top of the wingsail. The tip vortices affect the flow field around the tip in a very large space. The thickness of the wingsail at mid-chord is 2 m, so according to Figure 24, the spanwise flow happens within more than 10 m around the tip.

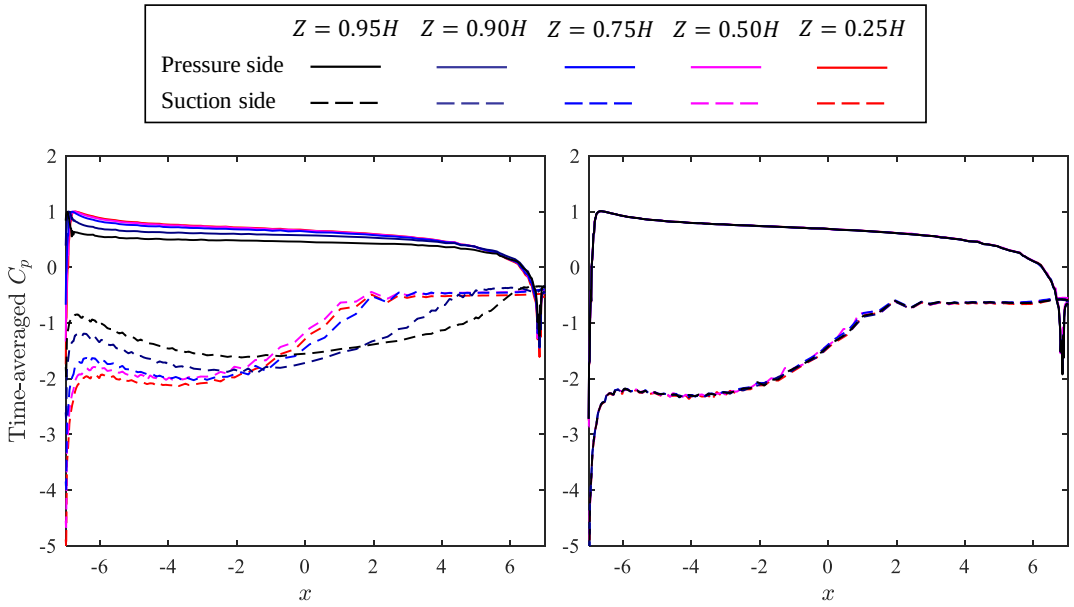

(a) Free-stream tip with symmetric bottom. (b) Periodic top and bottom.

Figure 23. Time-averaged wall pressure coefficient distribution of the crescent-shaped profile from three-dimensional simulations with different boundary conditions. $\alpha = 20°$.

For both section profiles, at the leading edge, two tip vortices develop independently at the pressure side and the suction side (Figure 25). The tip vortex that develops at the pressure side (i.e., the tip leakage vortex) is considerably stronger than the other one. Hence, at around the mid-chord, these two tip vortices begin to fuse together. The tip vortices generated by the wingsail with the crescent-shaped profile are stronger and dissipate more slowly than those induced by the NACA 0015 wingsail. For the wingsail with the crescent-shaped profile, the structure of the vortex becomes complex at the tip closer to the trailing edge, represented by the sectional plane $X = 0.41L_c$ in Figure 25(a). In the wake region of the wingsail, as the sectional plane $X = 0.63L_c$ in Figure 25(a), a main large tip vortex is finally formatted. However, for the wingsail with the NACA 0015 section, the main large vortex formats early around the sectional plane $X = 0.91L_c$ in Figure 25(b). A comparison of the rightmost sectional plane in Figure 25(a) and Figure 25(b) reveals that the tip vortices are still developing in Figure 25(a), but obviously begin to dissipate in Figure 25(b).

The tip vortices influence the flow field in a very large area, so proposing an effective solution to reduce the lift reduction caused by tip vortices is challenging. Some attempts have been made to achieve this (e.g., adding a wing flap or disc on top to prevent the round-tip flow in Figure 24) but the outcome has not been ideal. Other tip optimizations which lead the tip flow in a more proper way may be carried out in future studies to raise C_L.

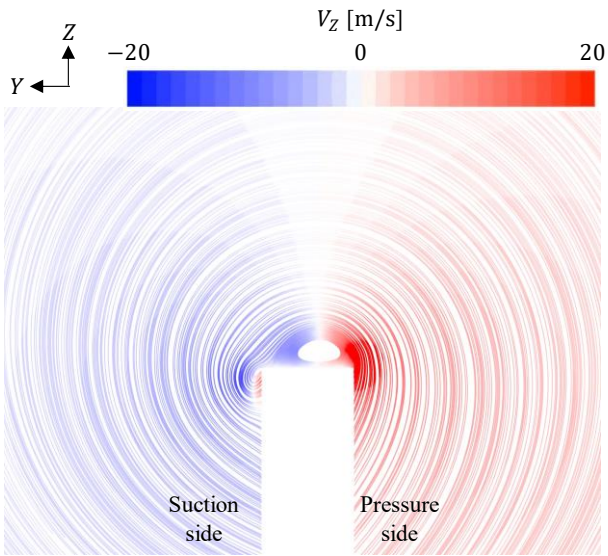

Figure 24. Flow streamlines around the tip in the streamwise sectional plan of the mid-chord ($X = 0$). Crescent-shaped profile, freestream tip boundary condition, $\alpha = 20°$.

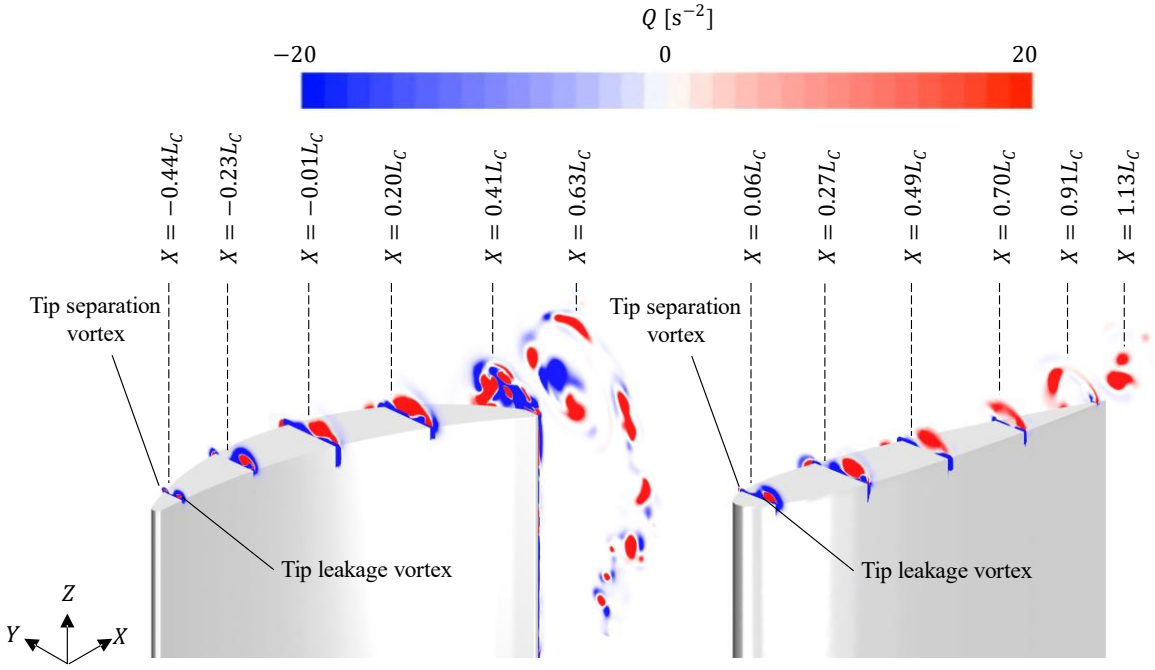

(a) Crescent-shaped profile. (b) NACA 0015.

Figure 25. The plot of Q at different streamwise positions around the tip. The boundary condition is a freestream tip and symmetric bottom. $\alpha = 20°$ for the crescent-shaped profile and $\alpha = 16°$ for NACA 0015. The inlet flow velocity is in the positive X direction.

3.2.3 Deep-stall conditions

When θ_{AW} is close to 90°, the wingsail may be operated with a large α (i.e., under deep-stall conditions). Figure 26 shows the distribution of ω_X on the iso-surface of $Q = 5\ \mathrm{s}^{-2}$. Tip vortices are still notable when $\alpha = 45°$ (Figure 26(a)) and vertical vortex tubes can still be seen developing on the suction side, but vortex tubes extending in the horizontal direction can also appear to be induced by the trailing edge. When $\alpha = 75°$ (Figure 26(b)), the tip vortices are much weaker and dissipate more quickly. Figure 26(c) shows the condition of $\alpha = 90°$, meaning that the chord line of the section profile is perpendicular to the apparent wind. Under this condition, tip vortices and vertical vortex tubes almost disappear, whereas horizontal vortex tubes induced by the edges become the main characteristic of the wake flow.

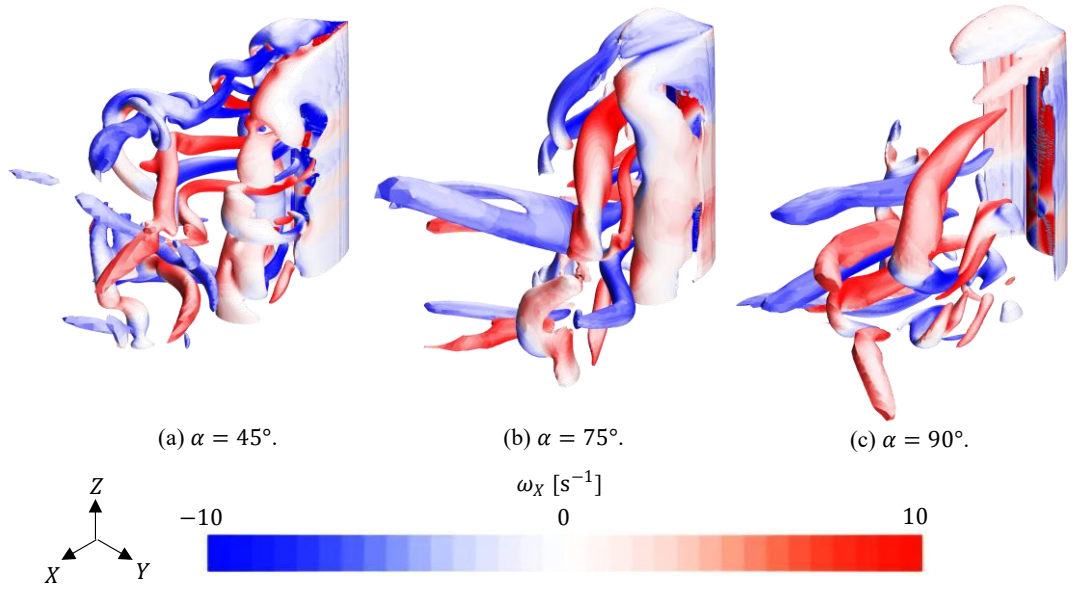

(a) $\alpha = 45°$. (b) $\alpha = 75°$. (c) $\alpha = 90°$.

Figure 26. Iso-surface of $Q = 5\ \mathrm{s}^{-2}$ under deep-stall conditions, colored with ω_X. The inlet flow velocity is in the positive X direction.

Usually, more than one wingsail is installed on a ship to capture more wind power. In related studies (Ouchi et al., 2011) (Malmek et al., 2020), the distance between the wingsails (i.e., the distance of the rotational axis) is usually less than two times the chord length. As shown in Figure 22 and Figure 26, for wingsails with the crescent-shaped profile, the influence on the wake flow spreads more than four times the chord length in the downstream region. Therefore, it can be inferred that the multiple wingsail interactions among wingsails with crescent-shaped profiles are more substantial than those based on the conventional NACA series. A numerical study on the multi-wingsail interaction may be conducted in the future.

3.3 Propulsive performance

3.3.1 Thrust at various wind directions

Based on the force coefficients from the CFD simulations with the freestream tip setup, the propulsive performance is evaluated, with the assumption that the force coefficients remained the same when the apparent wind speed changes following the direction of navigation because the force coefficients are believed not to be very sensitive to Re.

According to a previous study (Lu & Ringsberg, 2020), the best propulsive performance (i.e., the maximum C_T) of a rigid wingsail is obtained when the point of the sail is a beam reach, which means that the apparent wind angle is around 90° or 270°. At this point of sail, the wingsail is always operated with the α that provides the highest C_L. Thus, to compare the propulsive performance of a wingsail with the studied crescent-shaped profile and NACA 0015, the condition where F_L mainly contributes to the thrust is selected. Figure 27 presents the C_T vs. θ_{AW} for the crescent-shaped profile and the NACA 0015. For both profiles, α is fixed, which means $\alpha = 20°$ for the crescent-shaped profile and $\alpha = 16°$ for NACA 0015. It can be summarized that the crescent-shaped profile generates a noticeably greater thrust compared to the symmetrical NACA 0015 profile because of the higher C_L.

It should also be noticed that, usually, when the point of sail is luffing, close-hauled, or beam reach (i.e., θ_{AW} is from 30° to around 90°), F_L is the main source of thrust. However, under other conditions, the wingsail may be operated in another way to use F_D. Therefore, to predict the propulsive performance for all the apparent wind directions, an enumeration method is used to have C_T with θ_{AW} in the range from 0° to 180° and α in the range from 0° to 90°. The results of how much the propulsion is (the highest C_T at different θ_{AW}) and how the wingsail is operated (α that is applied to get the highest C_T) are plotted in Figure 28. Because a polar diagram is always symmetric, only half of the polar plot (i.e., $0° \leq \theta_{AW} \leq 180°$) is presented.

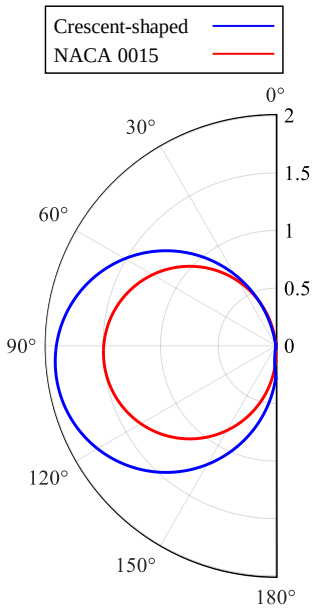

Figure 27. Polar diagram of C_T vs. θ_{AW} for the crescent-shaped profile and the NACA 0015 at $V_{AW} = 25$ m/s. For the crescent-shaped profile, $\alpha = 20°$; for NACA 0015, $\alpha = 16°$.

When the ship navigates against the wind (i.e., the luffing point of sail), C_T is low or even less than 0. During that time, the wingsail is operated with very low α to reduce the extra resistance. As θ_{AW} increases (e.g., $\theta_{AW} = 60°$), C_T increases, and the wingsail is operated with α_c having the maximum C_L. For θ_{AW} in a wide range from 60° to 180°, the wingsail can provide appreciable propulsion. However, the wingsail is not operated in the same way. For instance, when $30° < \theta_{AW} < 120°$, α should be around 20° to get the maximum C_L, and F_L is the main source of thrust. When $120° < \theta_{AW} < 150°$ (i.e., the point of sail is board reach), the optimum α is around 40° with $C_L \approx C_D$, and the wingsail uses both F_D and F_L for propulsion. When the point of sail is running (i.e., θ_{AW} is around 180°), F_D is mainly used and the wingsail is operated with $\alpha \approx 80°$.

The rescaled two-dimensional results predicted similar propulsive performance to that of the three-dimensional simulations. Therefore, the hybrid two- and three-dimensional method, which first performs two-dimensional simulations together with a limited number of three-dimensional simulations, and then rescales the force coefficients from the two-dimensional results to fit the three-simulation results, is able to provide a trustable prediction of the propulsive performance and reduce the computation capacity at the same time.

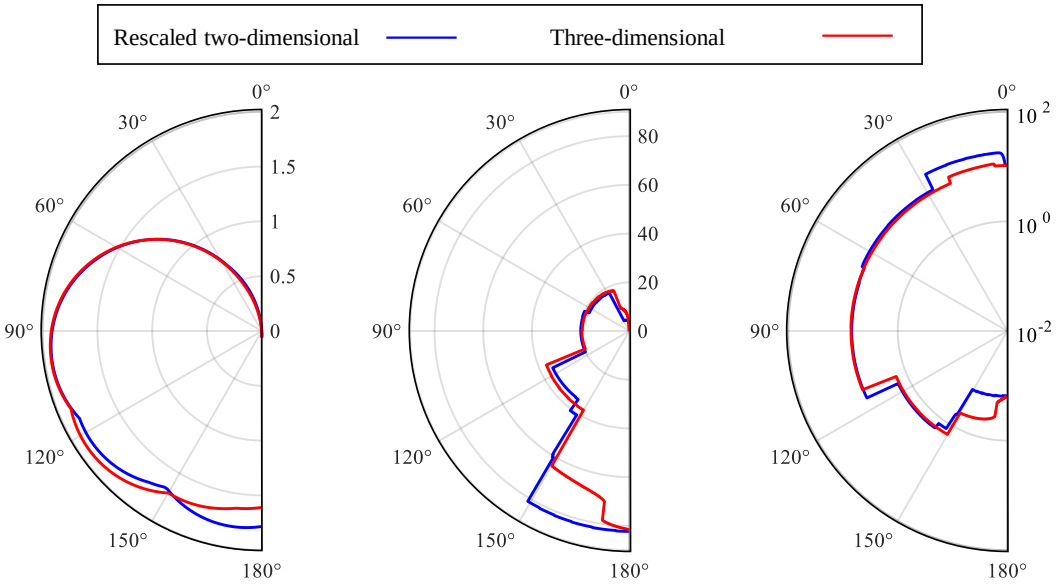

(a) C_T vs. θ_{AW}. (b) α vs. θ_{AW}. (c) L/D vs. θ_{AW}.

Figure 28. Polar diagram of C_T, α, and L/D vs. θ_{AW} for the crescent-shaped profile at $V_{AW} = 25$ m/s.

3.3.2 Expected fuel savings

To calculate the expected fuel savings, the first step is to create polar plots of the fuel savings under different wind strength conditions over several true wind angles. Figure 29 presents a polar plot of the fuel savings for the case study tanker with one crescent sail in 10 kn and 20 kn of wind. The sail is positioned 5 m behind the forward perpendicular, at the centerline of the ship.

The polar plot shows that a maximum fuel saving of about 9% at $\theta_{TW} = 90°$ in $V_{TW} = 10$ kn, and 25% in $\theta_{TW} = 90°$ in $V_{TW} = 20$ kn can be expected. However, the fuel savings vary over the true wind angle; thus, the performance must be predicted using actual routes with realistic weather, as presented in the following section.

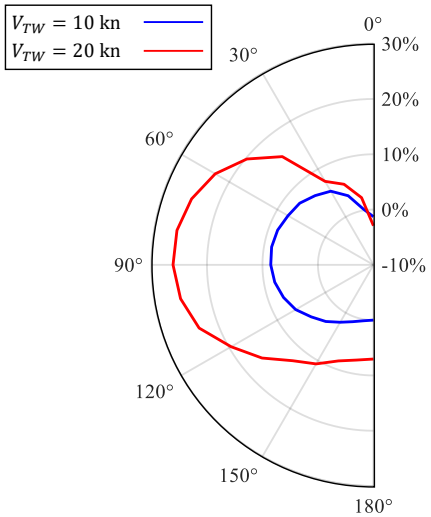

Figure 29. Polar plot of relative fuel consumption savings vs. θ_{TW} at two V_{TW}.

3.3.3 Prediction of long-term fuel savings

To predict the long-term fuel savings, the AIS data of the ship are used to derive the position and speed during the year 2018. The environmental conditions are retrieved from the Copernicus Marine Environment Monitoring Service (CMEMS) and are updated every 3 hours. The route is illustrated in Figure 11, and the wind conditions (true wind angle and true wind speed) are presented in the wind scatter plots in Figure 12. Because this case is symmetrical, all apparent wind angles are between 0 and 180 degrees.

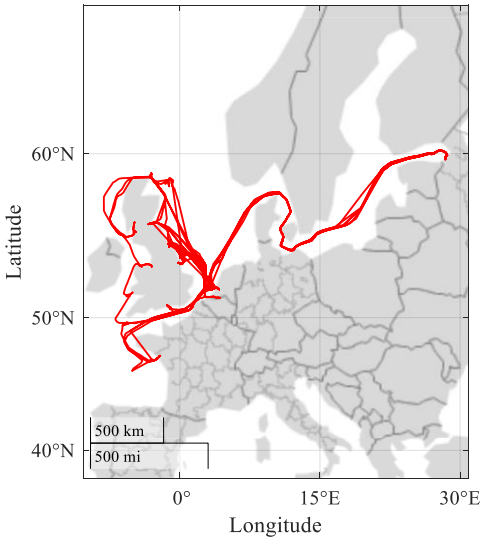

Figure 30. Route of the case study ship during 2018.

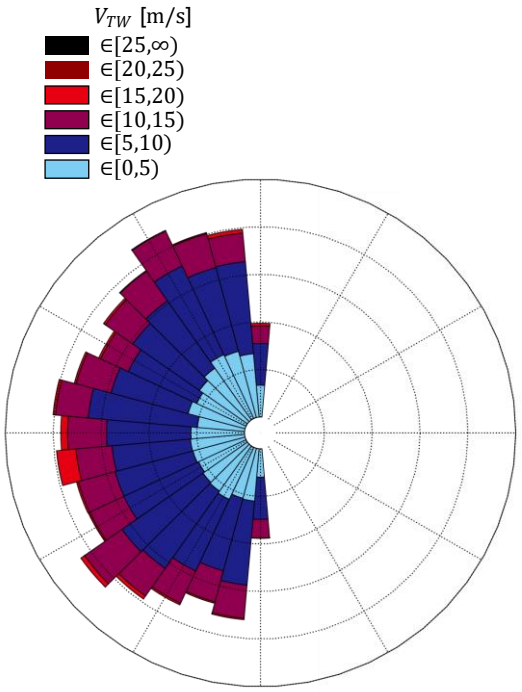

Figure 31: Scatter plot of the experiences with apparent wind angles and true wind speeds.

As a result, total savings of 9.5% were achieved with the crescent sail. For comparison purposes, the simulations were repeated with a Flettner rotor (5 m in diameter and 30 m in height) positioned similarly. The Flettner rotor would have resulted in 9.8% savings on the same route. To better understand the bandwidth of potential savings during a year of operation, Figure 32 presents a histogram of fuel savings respecting each waypoint (i.e., 1 point per 3 hours) for the full year. Additional drag was created only on very few occasions. About 34% of the time the fuel savings were larger than 5%. The maximum additional fuel consumption was less than 1%. The maximum fuel saving was 97.5%.

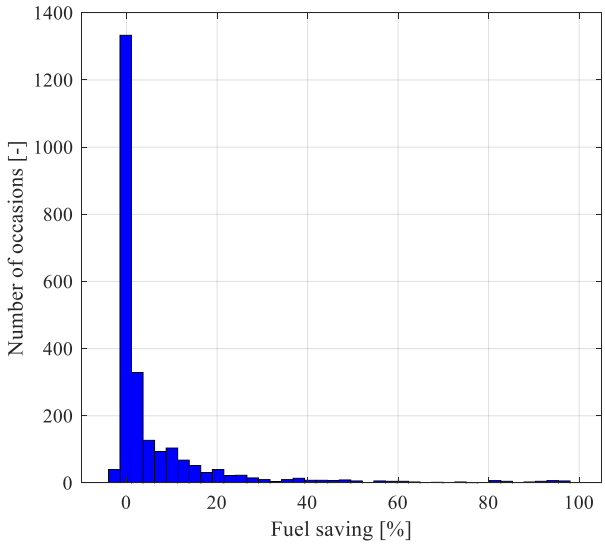

Figure 32: Histogram of the achieved fuel savings at each waypoint.

4. Conclusions

This study focused on the analysis of a new crescent-shaped sail profile based on high-fidelity numerical simulations. The computational method used was an unsteady RANS with the k - ω SST model. Moreover, the numerical settings, including the boundary conditions, were investigated to understand their effects on the prediction accuracy of the sail aerodynamics.

It was found that the two-dimensional simulations generally overestimated these force coefficients compared to the three-dimensional simulations. A reason behind this might be that vortex evolution and coherence in the spanwise direction are excluded from the two-dimensional simulations. Another reason might be that the tip vortices due to the freestream tip cause a lift reduction. However, both two- and three-dimensional simulations showed similar trends in the force changes with respect to the angles of attack, so by rescaling the two-dimensional results to a limited number of three-dimensional simulation cases, the propulsive performance can be convincingly predicted.

To understand the tip vortex effects on aerodynamics, such as F_D and F_L, the computational domain and boundary conditions were investigated using two setups. One setup used the periodic boundary conditions at the spanwise side boundaries, whereas the other adopted the symmetry boundary condition at both side boundaries. Moreover, in the second case, the top-side boundary was positioned far away from the top-side edge of the sail to eliminate the influence of the boundary on the flow. The sail configuration was attached to the bottom side boundary, which represents the water-free surface, and was thus imposed with the symmetry boundary condition. The second case reproduces the vortices induced from the tip side edges of the wingsail. Moreover, because side-edge vortices exist, this effect alleviates the breaking of the spanwise coherence in the vortex shedding that evolves downstream of the sail trailing edge.

The new crescent sail profile generated a notably higher thrust force compared to a NACA 0015 profile. Nevertheless, more flow separation points were found in this new profile. Separation aggravates flow unsteadiness and, consequently, introduces more unsteady surface loads on the sail. This effect poses a challenge to the strength and stability of the wingsail structure.

The case study indicated that fuel consumption can be substantially reduced by installing one crescent-shaped wingsail. A maximum saving of about 9% in $V_{TW} = 10$ kn and 25% in $V_{TW} = 20$ kn can be expected. The maximum full consumption saving is obtained when $\theta_{TW} = 90°$ (i.e., the sidewind condition). According to the prediction of long-term fuel savings, total savings of 9.5% are achieved with the crescent-shaped wingsail, which is similar to the savings obtained with five

Flettner rotors with a height of 30 m. A disadvantage of the new profile is that it causes extra resistance when sailing against the wind, but this happens on very few occasions. The maximum additional fuel consumption due to the extra resistance is less than 1%, whereas the maximum fuel saving is 97.5%, which means that the wingsail covered almost all of the propulsion power.

This study gives insights into the potential causes of structural instability or fatigue in relation to fluid dynamics, which is obvious in multi-wingsail interaction problems. Hence, the findings can be applied to guide the design of wingsail geometries and installation.

Acknowledgment

This work was performed as part of the WindStruc (wind-assisted propulsion for commercial vessels) project, co-funded by ScandiNAOS AB, the Swedish Energy Agency, and Stena Rederi AB. Professor Carl-Erik Janson from Chalmers University of Technology offered guidance for the CFD simulations and propulsive analysis. The computations and data handling were enabled by resources provided by the Swedish National Infrastructure for Computing (SNIC), which is partially funded by the Swedish Research Council through grant agreement No. 2018-05973.

Disclosure statement

The authors report there are no competing interests to declare.

References

Atkinson, G. M. (2019). Analysis of lift, drag and CX polar graph for a 3D segment rigid sail using CFD analysis. *Journal of Marine Engineering and Technology*, *18*(1), 36–45. https://doi.org/10.1080/20464177.2018.1494953

Bialystocki, N., & Konovessis, D. (2016). On the estimation of ship's fuel consumption and speed curve: A statistical approach. *Journal of Ocean Engineering and Science*, *1*(2), 157–166.

Blount, H., & Portell, J. M. (2021). *CFD investigation of wind powered ships under extreme conditions* [Chalmers University of Technology]. https://odr.chalmers.se/handle/20.500.12380/304254

Cairns, J., Vezza, M., Green, R., & MacVicar, D. (2021). Numerical optimisation of a ship wind-assisted propulsion system using blowing and suction over a range of wind conditions. *Ocean Engineering*, *240*, 109903. https://doi.org/10.1016/J.OCEANENG.2021.109903

Castelli, M. R., Cioppa, P., & Benini, E. (2012). Numerical Simulation of the Flow Field around a Vertical Flat Plate of Infinite Extent. *International Journal of Aerospace and Mechanical Engineering*, *6*(1), 47–52.

Chen, Z., Cai, W., & Zeng, Q. (2022). A numerical study on the thrust and interaction of a three-sail wind-assisted propulsion system. *Proceedings of the ASME 2022, 41st International Conference on Ocean, Offshore and Arctic*.

Gadonneix, P., Sambo, A., Tie'nan, L., Choudhury, A. R., Teyssen, J., Lleras, J. A. V., Naqi, A. A., Meyers, K., Shin, H. C., & Nadeau, M.-J. (2011). Global transport scenarios 2050. *World Energy Council*, *456*.

Hilsenrath, J. (1955). *Tables of thermal properties of gases: comprising tables of thermodynamic and transport properties of air, argon, carbon dioxide, carbon monoxide, hydrogen, nitrogen, oxygen, and steam* (Vol. 564). US Department of Commerce, National Bureau of Standards.

Hoerner, S. F. (1976). Fluid-Dynamic Drag: Practical Information on Aerodynamic Drag and Hydrodynamic Resistance. In *The Aeronautical Journal* (Vol. 80, Issue 788). Cambridge University Press. https://doi.org/10.1017/s0001924000034187

Houghton, E. L., & Carruthers, N. B. (1982). *Aerodynamics for engineering students. Third edition.* Elsevier.

IMO. (2018). *Interpretation of Initial IMO Strategy on Reduction of GHG Emissions from Ships* (Vol. 60, Issue 1, pp. 195–201).

International Chamber of Shipping. (2014). *Shipping, world trade and the reduction of CO2 emissions*. London: International Chamber of Shipping.

Khan, L., Macklin, J., Peck, B., Morton, O., & Souppez, J.-B. R. G. (2021, September 15). A review of wind-assisted ship propulsion for sustainable commercial shipping: Latest developments and future stakes. *Proceedings of the Wind Propulsion Conference 2021*.

Lu, R., & Ringsberg, J. W. (2020). Ship energy performance study of three wind-assisted ship propulsion technologies including a parametric study of the Flettner rotor technology. *Ships and Offshore Structures*, *15*(3), 249–258. https://doi.org/10.1080/17445302.2019.1612544

Malmek, K., Dhomé, U., Larsson, L., Werner, S., Ringsberg, J. W., & Finnsgård, C. (2020). Comparison of two rapid numerical methods for predicting the performance of multiple rigid wing-sails. *The 5th International Conference on Innovation in High Performance Sailing Yachts and Sail-Assisted Ship Propulsion (INNOV'SAIL 2020)*.

Menter, F. R. (1993). Zonal two equation κ-ω turbulence models for aerodynamic flows. *AIAA 23rd Fluid Dynamics, Plasmadynamics, and Lasers Conference, 1993*. https://doi.org/10.2514/6.1993-2906

Menter, F. R., Smirnov, P. E., Liu, T., & Avancha, R. (2015). A One-Equation Local Correlation-Based Transition Model. *Flow, Turbulence and Combustion 2015 95:4*, *95*(4), 583–619. https://doi.org/10.1007/S10494-015-9622-4

Najjar, F. M., & Vanka, S. P. (1995). Effects of intrinsic three-dimensionality on the drag characteristics of a normal flat plate. *Physics of Fluids*, *7*(10), 2516–2518.

Nikmanesh, M. (2021). *Sailing performance analysis using CFD simulations: A study on crescent shaped wing profiles* [Chalmers University of Technology]. https://odr.chalmers.se/handle/20.500.12380/304303

Ouchi, K., Uzawa, K., & Kanai, A. (2011). Huge Hard Wing Sails for the Propulsor of Next Generation Sailing Vessel. *Second International Symposium on Marine Propulsors*, *June*, 1–5.

Park, J. S., Witherden, F. D., & Vincent, P. E. (2017). High-order implicit large-eddy simulations of flow over a NACA0021 aerofoil. *AIAA Journal*, *55*(7), 2186–2197. https://doi.org/10.2514/1.J055304

Patankar, S. V. (1980). *Numerical heat transfer and fluid flow*. CRC Press. https://doi.org/10.13182/nse81-a20112

Persson, A., Li, D.-Q., Olsson, F., Werner, S., & Dhomé, U. (2019). Performance prediction of wind propulsion systems using 3D CFD and route simulation. *RINA, Royal Institution of Naval Architects-International Conference on Wind Propulsion, WP 2019, 15-16 October 2019, London, United Kingdom*, 19–30.

Reichardt, H. (1951). Vollständige Darstellung der turbulenten Geschwindigkeitsverteilung in glatten Leitungen. *ZAMM - Journal of Applied Mathematics and Mechanics / Zeitschrift Für Angewandte Mathematik Und Mechanik*, *31*(7), 208–219. https://doi.org/10.1002/ZAMM.19510310704

Ritchie, H., Roser, M., & Rosado, P. (2020). CO_2 and Greenhouse Gas Emissions. *Our World in Data*.

Sheldahl, R. E., & Klimas, P. C. (1981). *Aerodynamic characteristics of seven symmetrical airfoil sections through 180-degree angle of attack for use in aerodynamic analysis of vertical axis wind turbines*. https://doi.org/10.2172/6548367

Siemens PLM Software. (2021). *STAR-CCM+ user guide (version 16.02)*. Siemens PLM Software Inc: Munich, Germany.

Smith, T. W. P., Jalkanen, J. P., Anderson, B. A., Corbett, J. J., Faber, J., Hanayama, S., O'keeffe, E., Parker, S., Johansson, L., & Aldous, L. (2015). *Third IMO greenhouse gas study 2014*.

Thies, F., & Ringsberg, J. W. (2022). Analysis of uncertainties in the prediction of fuel savings from WASP installations. *Proceedings of The 14th Symposium on High-Performance Marine Vehicles (HIPER 2022)*, 262–270.

Tillig, F., & Ringsberg, J. W. (2019). A 4 DOF simulation model developed for fuel consumption prediction of ships at sea. *Ships and Offshore Structures*, *14*(sup1), 112–120.

Tillig, F., & Ringsberg, J. W. (2020). Design, operation and analysis of wind-assisted cargo ships. *Ocean Engineering*, *211*, 107603. https://doi.org/10.1016/j.oceaneng.2020.107603

Tillig, F., Ringsberg, J. W., Mao, W., & Ramne, B. (2018). Analysis of uncertainties in the prediction of ships' fuel consumption–from early design to operation conditions. *Ships and Offshore Structures*, *13*(sup1), 13–24.

Tillig, F., Ringsberg, J. W., Psaraftis, H. N., & Zis, T. (2019). ShipCLEAN–an integrated model for transport efficiency, economics and CO2 emissions in shipping. *Proceedings of the 2nd International Conference on Modelling and Optimization of Ship Energy Systems (MOSES 2019)*, 8–10.

Viola, I. M., Biancolini, M. E., Sacher, M., & Cella, U. (2015). A CFD-based wing sail optimisation method coupled to a vpp. *5th High Performance Yacht Design Conference, HPYD 2015*, 1–7.

Wilcox, D. C. (1989). *Turbulence Modeling for CFD* (Vol. 27, Issue 10).

Workinn, D. (2021). *A high-level interface for a sailing vessel* [KTH Royal Institute of Technology]. http://urn.kb.se/resolve?urn=urn:nbn:se:kth:diva-299430

Zhu, H. (2020). *CFD Investigation of Wind-powered Ships under Extreme Condition* [Chalmers University of Technology]. https://odr.chalmers.se/handle/20.500.12380/301919

Paper II

Unsteady RANS and IDDES Studies on a Telescopic Crescent-Shaped Wingsail

Unsteady RANS and IDDES Studies on a Telescopic Crescent-Shaped Wingsail

Heng Zhu[1,*], Hua-Dong Yao[1], Jonas W. Ringsberg[1]

[1] Chalmers University of Technology, Department of Mechanics and Maritime Sciences, Division of Marine Technology, SE-412 96 Gothenburg, Sweden

[*] Corresponding author: heng.zhu@chalmers.se

Abstract

Over the years, several research projects have developed to evaluate different concepts for wind-assisted propulsion, generally concluding that it can lead to significant fuel savings. The time-averaged propulsive performance of a single rigid wingsail has been analyzed in previous studies. However, the unsteady characteristics of the external loads which may induce structural vibration is also important to be considered. In this study, full-scale simulations, with both unsteady RANS and IDDES methods, are performed to analyze the flow field around a wingsail. The paper's analysis includes flow separation and vortex shedding, the development and dissipation of wake vortices, and the lift reduction due to tip vortices. It also studies the telescopic function of the wingsail by analyzing sails with different heights and wind conditions. The paper concludes that the unsteady RANS and IDDES simulations make similar predictions for time-averaged loads but disagree on the unsteady characteristics of the flow field. The IDDES simulations indicate more complex vortex-shedding phenomena.

Keywords: *flow separation; IDDES; unsteady RANS; wake analysis; wind-assisted ship propulsion*

Nomenclature

C_D	Drag force coefficient [-]
C_L	Lift force coefficient [-]
C_M	Moment coefficient [-]
C_p	Pressure coefficient [-]
C_T	Thrust force coefficient [-]
$C_{T,max}$	Maximum thrust force coefficient [-]
H	Sail height (spanwise length) [m]
L_c	Chord length [m]
P	Pressure [Pa]
Q	Q-criterion [s^{-2}]
Re	Reynolds number [-]
V_{AW}	Apparent wind speed (inlet velocity) [m/s]
V_S	Ship speed [m/s]
V_{TW}	True wind speed [m/s]
V_X	Streamwise velocity [m/s]
y^+	Dimensionless wall-normal distance [-]
α	Angle of attack [°]
α_c	Critical angle of attack [°]
θ_{AW}	Apparent wind angle [°]
θ_{TW}	True wind angle [°]
μ	Dynamic viscosity [Pa · s]
ρ	Air density [kg/m^3]
ω_X	Streamwise vorticity [s^{-1}]
ω_X^*	Non-dimensional streamwise vorticity [-]
ω_Z	Spanwise vorticity [s^{-1}]
ω_Z^*	Non-dimensional spanwise vorticity [-]

1. Introduction

Transportation accounts for a large proportion of greenhouse gas emissions. According to the data of 2017, transportation shared 24% of the EU greenhouse gas emission (EUROSTAT, 2019). On the basis of the statistical data in 2014, approximately 90% of world trade volume is transported by shipping fleets (International Chamber of Shipping, 2014). The International Maritime Organization (IMO) has agreed on a target to reduce greenhouse gas emissions from shipping by 50%, relative to 2018 levels, by 2050 (IMO, 2018). The use of wind-assisted ship propulsion is regarded as a promising means to help achieve this goal. Over the years, several projects have been carried out to develop and evaluate different concepts for wind-assisted propulsion systems using rigid wingsails and have found that they can reduce fuel consumption by over 30% (Hamada, 1985). Unlike kite sails, rigid wingsails can not only propel ships by the drag force but also the lift force, enabling ships to navigate against the wind (Kimball, 2009). An ongoing project, Oceanbird (Workinn, 2021), even aims to achieve a 90% fuel reduction, which is much higher than the typical savings from Flettner rotors, which are 8% on average (International Transport Forum, 2020), 30% for tankers (Tillig & Ringsberg, 2020), and around 50% at maximum (Traut et al., 2014). Due to the bluff body, Flettner rotors suffer from high drag, resulting in extra resistance when the rotors are not operating (Khan et al., 2021). In addition, rigid wingsails show better propulsive performance than

Flettner rotors under downwind conditions, in which the drag force contributes to the propulsion (Lu & Ringsberg, 2020). Compared with traditional soft sails, the main advantages of rigid wingsails are that they maintain their shape in light winds and are more robust to control since there is no rope that could become entangled (Sauzé & Neal, 2008). They also have simpler structures and are easier to design and manufacture (Silva et al., 2019).

The key characteristic of a propulsion system is its propulsive performance. In addition to empirical studies or experimental tests, such as wind tunnel tests, numerical simulations are seen as an efficient way to predict propulsive performance. In recent years, several researchers have developed numerical methods to study rigid wingsails based on airfoil profiles. Lee et al. (Lee et al. 2016) studied a series of rigid wingsails based on the NACA 0012 profile, carried out numerical aerodynamic analysis using a viscous Navier–Stokes flow solver, and established a design optimization framework to maximize the thrust coefficient, C_T. Ma et al. (Ma et al., 2018) studied three typical airfoil-based sails by computational fluid dynamics (CFD) simulations, using the $k-\omega$ shear stress transport (SST) turbulence model. Blount and Portell (Blount & Portell, 2021) studied a concept based on the NACA 0015 profile using the improved delayed detached eddy simulation (IDDES) method and discussed the vortex shedding under downwind conditions. These conventional sectional profiles provide effective propulsion, but an even higher C_T needs to be obtained to achieve the IMO target. It has been found that aerodynamically asymmetric profiles, such as segment-shaped (Atkinson, 2019) or crescent-shaped (Nikmanesh, 2021) profiles, show better propulsive performance than conventional designs.

However, as predicted by unsteady Reynolds-averaged Navier–Stokes equations (uRANS) CFD simulations (Zhu et al., 2022), the notable camber of these profiles leads to significant flow separation and an unsteady flow field, which are challenging to capture using numerical models. Moreover, when considering the structural response, it is important to consider not only the time-averaged loading conditions but also oscillations in the loads, which can induce a global flutter or local vibrations. To analyze vortex-induced vibrations (VIV), it is necessary to accurately predict the frequency of the oscillations in the external loads. In addition, there is usually more than one sail installed on a ship, and the wake flow of the upstream sail will likely have an influence on the downstream sails. Therefore, an improved CFD model needs to be established to understand the unsteady properties and the wake flow.

This study, which is a continuation of previous work (Zhu et al., 2022), investigates a concept design of a telescopic rigid wingsail with a crescent-shaped profile using CFD. It performs and compares numerical simulations based on the IDDES method with uRANS simulations to provide a more accurate numerical model for predicting propulsive performance. It is found that by applying the IDDES method, more detailed information about the flow field can be obtained, especially the flow separation and the vortex shedding. In addition, due to the vortex shedding, studies on the structural response are necessary to avoid structural failures such as plastic deformation, buckling, and fatigue.

2. Methodology

2.1 Concept design

2.1.1 Crescent-shaped section

In this study, the horizontal section profile of the wingsail, illustrated in Figure 1, is a simple crescent shape, made up of arcs and circles. There are four main design parameters: the chord length, the edge radius, the suction-side arc radius, and the mast diameter. The shape of the profile, including the pressure-side arc radius, is determined by these four parameters. The arcs of the pressure side and suction side are symmetric about the symmetric axis (the dashed blue line in Figure 1). The radius of the edges is chosen to make the profile structurally sound.

A parametric sensitivity analysis is carried out. The mast diameter and the suction-side arc radius are adjusted. The chord length is always set at 14 m, and the edge radius is always 0.2 m. A series of profiles (shown in Figure 2) are generated by varying the remaining two parameters and are labeled in the form “DxRy,” where “x” represents the mast diameter and “y” represents the suction-side arc radius. For example, for the profile named “D2R8,” the mast diameter is 2 m and the suction-side arc radius is 8 m, which results in an arc radius of 10.67 m on the pressure side.

Figure 3 shows the results of two-dimensional simulations for several different profiles. The error bars represent the oscillation amplitudes. Clearly, as the camber increases, the drag coefficient C_D increases while the lift coefficient C_L initially increases and then decreases. For profiles with extreme camber, such as D1R7.5, the oscillation of the force coefficients becomes very strong. The profiles D2R8 and D1R8 show the highest time-averaged lift force coefficient but the loads on D1R8 show much larger oscillations. By considering the structural arrangements, a mast with a larger diameter is expected to provide better strength, so the D2R8 profile is selected for this study.

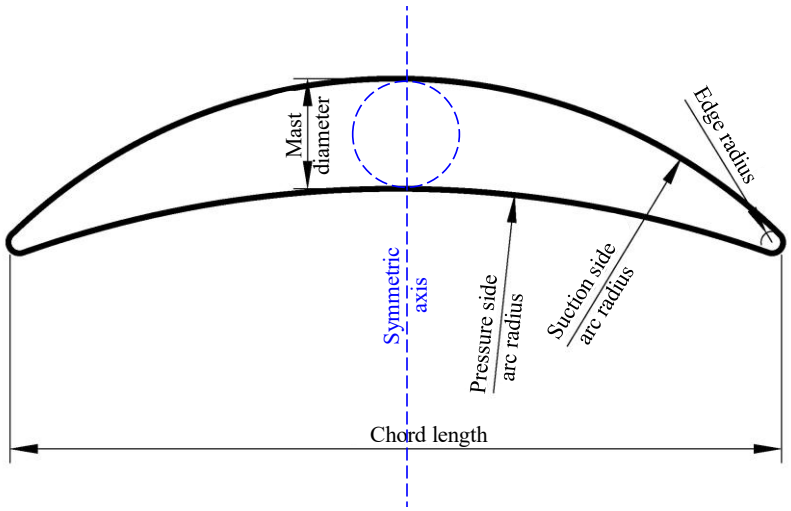

Figure 1. Design parameters of the crescent-shaped profile.

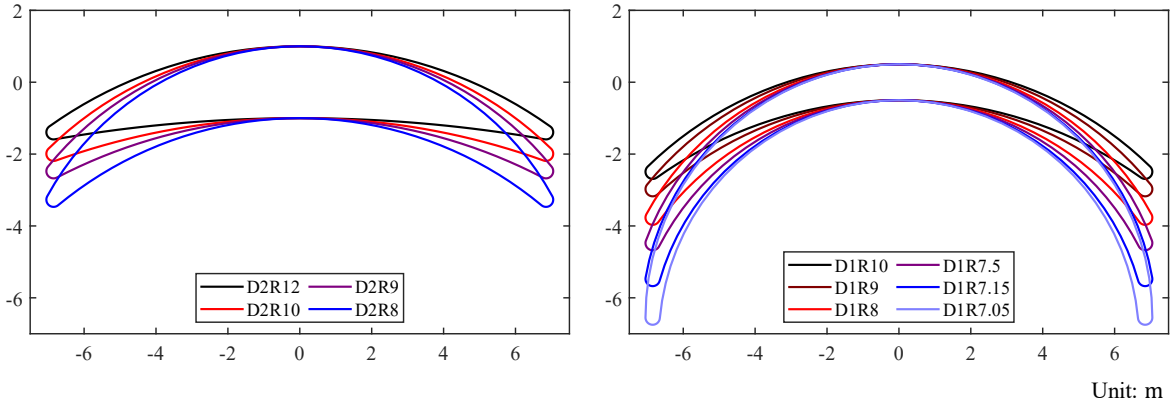

Figure 2. Crescent-shaped profiles based on different design parameters.

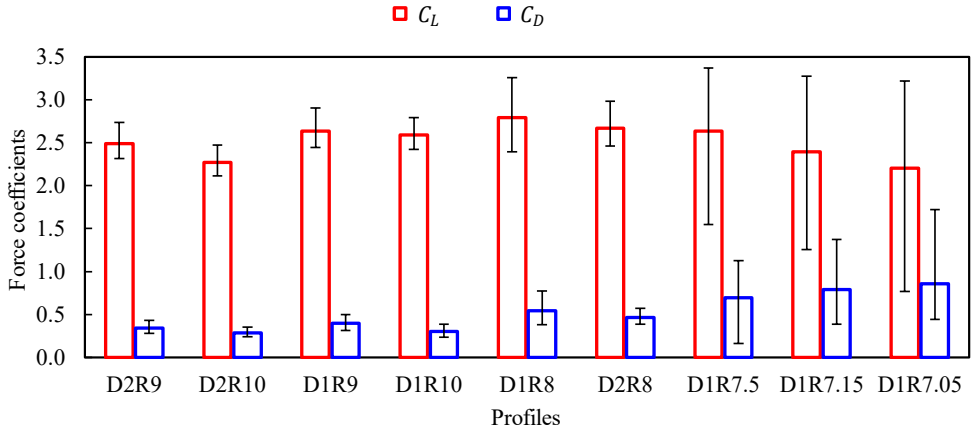

Figure 3. Force coefficients of different profiles.

2.1.2 Telescopic function

The rig is designed to have a telescopic function to enable reefing of the wingsails depending on the wind conditions, as shown in Figure 4. The wingsail is divided into four sections, which can be retracted or expanded. For example, at low wind speeds, such as 8 m/s, the wingsail would be expanded to generate maximum propulsion, while for conditions with higher wind speeds, such as 32 m/s, it would be retracted to prevent structural failures. The fully expanded height of the wingsail is 74 m, while the fully retracted height is 26 m. The wingsail is supported by a mast that is fixed to the deck. In the preliminary design, the total height of the mast is 6 m, with 2 m inside the sail.

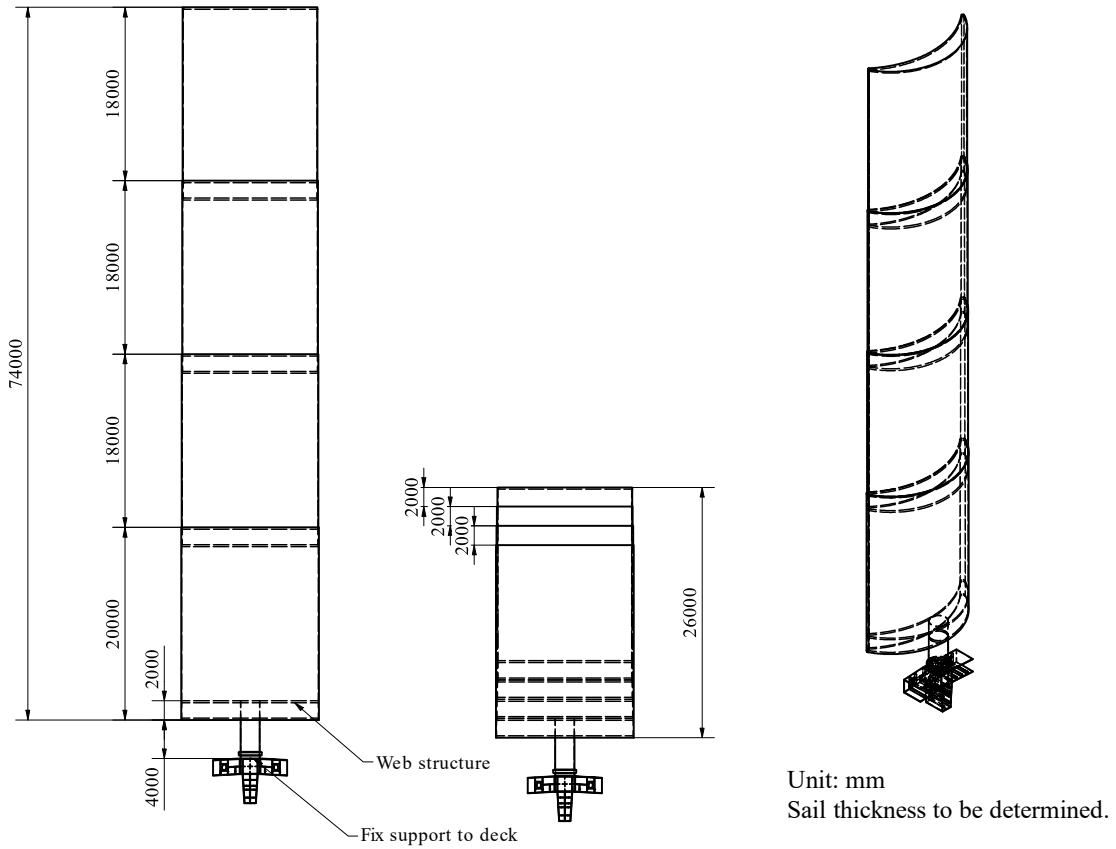

Figure 4. Concept design of the telescopic rigid wingsail.

2.2 Physical conditions

In the CFD simulations, the wingsail is modeled as a uniformly extruded rigid body. As mentioned in Section 2.1.1, the height of the wingsail can be adjusted according to the apparent wind speed. Two conditions are simulated, the fully expanded condition and the fully retracted condition, with the parameters listed in Table 1.

Table 2 shows the properties of the fluid (air at 25℃). Since the chord length of the section is $14\,\mathrm{m}$, Re is 6.78×10^6 for the fully expanded condition and 2.71×10^7 for the fully retracted condition.

The global coordinate system is defined such that the origin is located at the bottom surface at the center of the mean camber line (i.e., the half-thickness point at the mid-chord). The X-axis is parallel to the streamwise direction and has the same direction as the inlet flow. The Y-axis represents the crossflow direction, pointing from the pressure side to the suction side. The Z-axis points vertically from the bottom to the top, representing the spanwise direction.

The calculation domains for the two conditions have the same size, as shown in Figure 5. The top and bottom of the domain have symmetric boundary conditions. The upstream panel is treated as a velocity inlet with uniformly distributed inlet flow, representing the apparent wind. The direction of the inlet flow can also be seen in Figure 5. The downstream panel and the crossflow sides are treated as pressure outlets. To avoid the influence of the reversed flow at pressure outlet boundaries, the direction of the backflow is set to be extrapolated. The pressure loss at the pressure outlets is assumed to be 0, and the pressure jump under-relaxation factor is set as 0.5.

Table 1. Height and apparent wind speed of the two simulated conditions.

Condition	V_{AW}	H
Fully expanded	$8\,\mathrm{m/s}$	$74\,\mathrm{m}$
Fully retracted	$32\,\mathrm{m/s}$	$32\,\mathrm{m}$

Table 2. Properties of the fluid (air at 25℃).

Property	Value	Unit
μ	1.85508×10^{-5}	$\mathrm{Pa \cdot s}$
ρ	1.18415	$\mathrm{kg/m^3}$

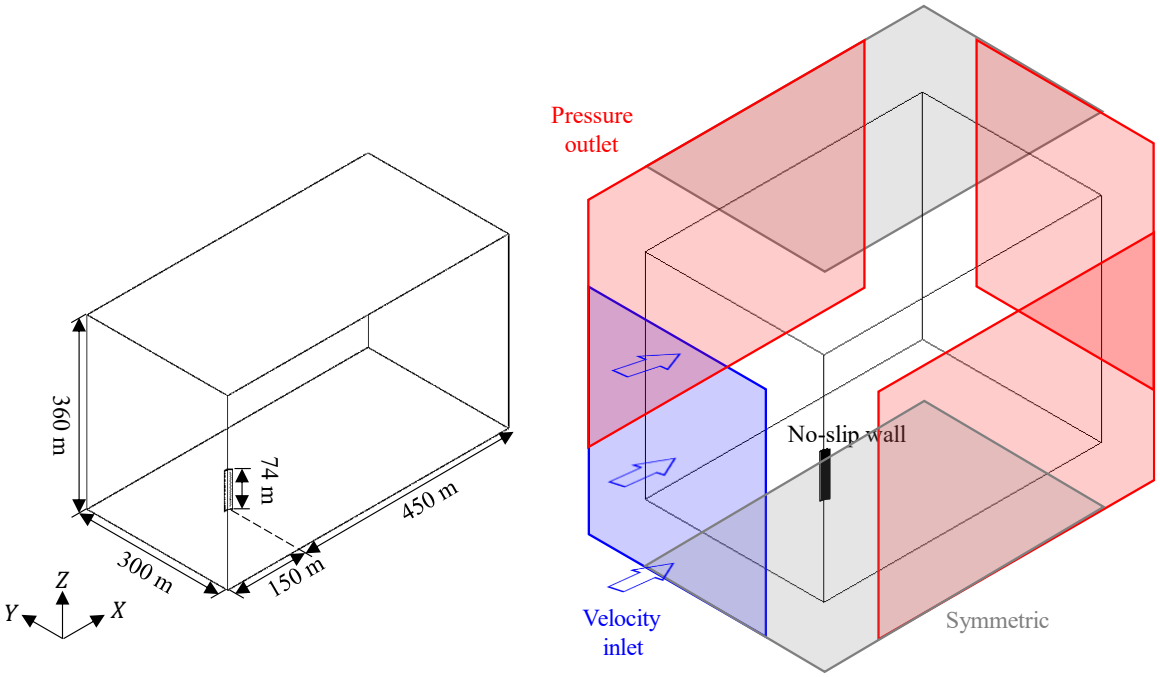

(a) Size of the computational domain. (b) Boundary conditions.

Figure 5. Computational domain and boundary conditions, fully expanded condition.

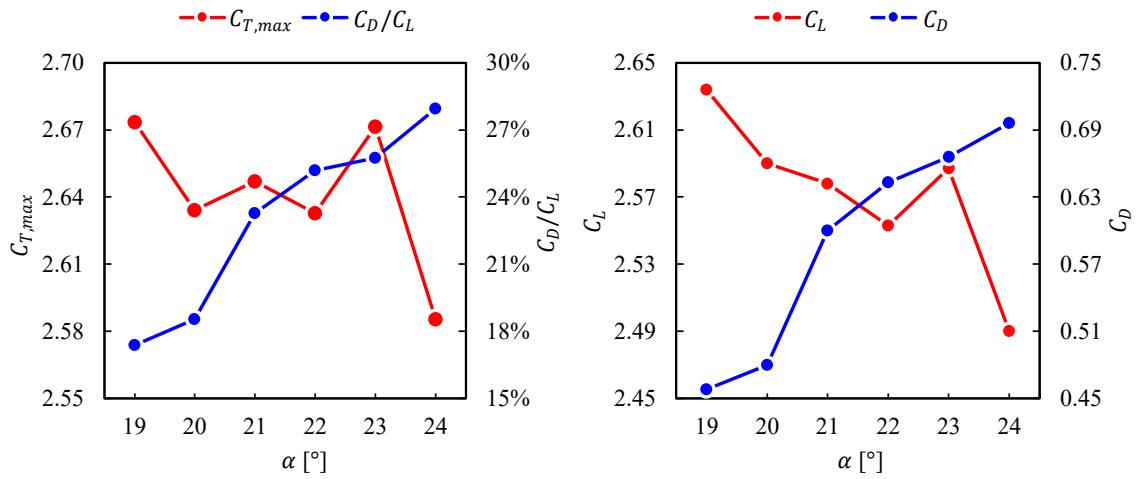

(a) $C_{T,max}$ and C_D/C_L. (b) C_L and C_D.

Figure 6. Time-averaged force coefficients vs. α, based on two-dimensional CFD simulations.

Unlike conventional airfoils, flow separation phenomena can be found even when the angle of attack $\alpha = 0°$, so there is no specific stall angle. Instead, the C_L is damped across a range of α values. Initial two-dimensional CFD simulations are performed to find the critical angle of attack α_c (results shown in Figure 6), based on which three-dimensional CFD simulations are performed. In the two-dimensional CFD simulations, the maximum C_L is obtained when $\alpha = 19°$. There is also a lower peak in C_L when $\alpha = 23°$. Within the range studied, C_D shows a positive correlation with α. If only the lift force is considered, 19° should be the optimum angle of attack. However, for this sectional profile, the contribution of the drag force to the thrust cannot be ignored since the ratio between drag and lift is around 17–29%. By considering the maximum C_T value $C_{T,max} = \sqrt{C_L^2 + C_D^2}$, two peaks are found at $\alpha = 19°$ and $\alpha = 23°$. Therefore, in this study, three-dimensional CFD simulations are performed based on three values of α, namely, 19°, 21°, and 23°.

2.3 Mesh

An unstructured mesh with a trimmed cell topology (Siemens PLM Software, 2021) is applied for the uRANS and IDDES numerical simulations. Prism layers are generated near the walls to resolve the flow in the boundary layers. Figure 7 shows the trimmed mesh in the sectional planes of $Z = 0.5H$ and $Y = 0$ (the half chord). The mesh is refined with eight levels in addition to the

prism layers. According to previous studies (Zhu et al., 2022), the flow field around the crescent-shaped foil displays significant flow separation phenomena. Flow separation is induced by both the trailing edge and the leading edge. Therefore, local refinement is applied to the wake region, the region close to the tip, and the region around the foil, especially in areas close to the two edges. The angle between the direction of the wake refinement and the streamwise direction is 0.5α (see Figure 7(a)). The length of the wake refinement is 60 m, and the separating angle is 0.25 rad, as shown in Figure 7(b). For the cells in the wake region, the size is around 0.32 m. As shown in Figure 7(c), the size of cells is 0.08 m for those close to the edges, and the thickness of the prism layer is 0.5 m with 65 layers inside. To study the characteristics of the tip vortices, the mesh around the free-stream tip is also refined, as shown in Figure 7(d).

The total number of cells for the fully expanded condition is about 23 million, while for the fully retracted condition it is around 8 million. The global mesh refinement is based on a prior mesh independence study (Zhu et al., 2022).

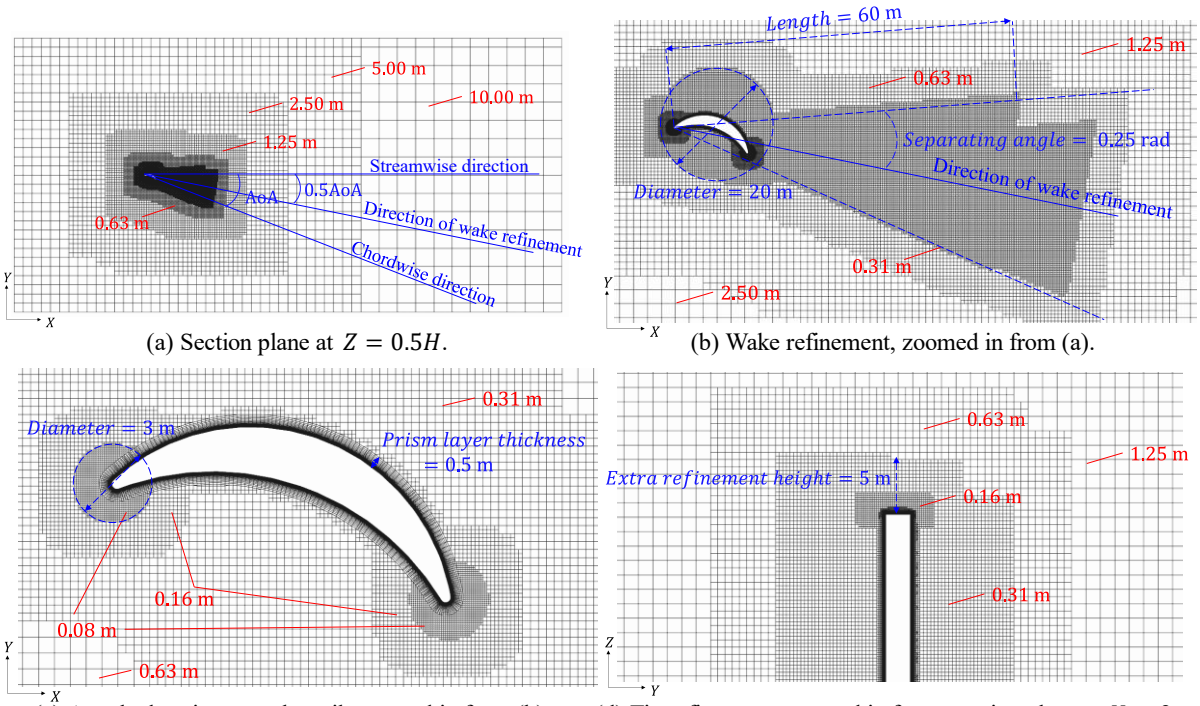

(a) Section plane at $Z = 0.5H$.

(b) Wake refinement, zoomed in from (a).

(c) Attached region near the sail, zoomed in from (b).

(d) Tip refinement, zoomed in from section plane at $Y = 0$.

Figure 7. Numerical mesh with typical cell sizes. Fully expanded condition with $\alpha = 19°$.

2.4 Numerical model

2.4.1 Viscous regimes

To solve this high-Re problem, turbulence models need to be incorporated. In the previous study (Zhu et al., 2022), a CFD model based on the uRANS method was developed, and the time-averaged loading conditions were well solved since the boundary-layer flow was resolved with a finely layered mesh. However, significant flow separation was found, which leads to significant unsteady characteristics of the flow field. When studying the propulsive performance of a single sail, it is enough to only consider the time-averaged loads. However, the unsteady characteristics should be considered when analyzing the structural response. For example, a low-frequency oscillation of the external loads may cause vortex-induced vibration of the whole sail, while a high-frequency oscillation may cause local vibrations on the shell panels, resulting in buckling. To simulate the separating flow more accurately, the large eddy simulation (LES) method (Smagorinsky, 1963) needs to be introduced, since all turbulent scales are modeled in uRANS, while only small, isotropic turbulent scales are modeled in LES (Davidson, 2019). By applying the LES method, both the time-averaged properties and the unsteady characteristics can be determined. On the other hand, the LES method imposes costly near-wall meshing requirements. To avoid that and keep the boundary-layer flow well-resolved, the detached eddy simulation (DES) method, which combines uRANS and LES, is selected in this study.

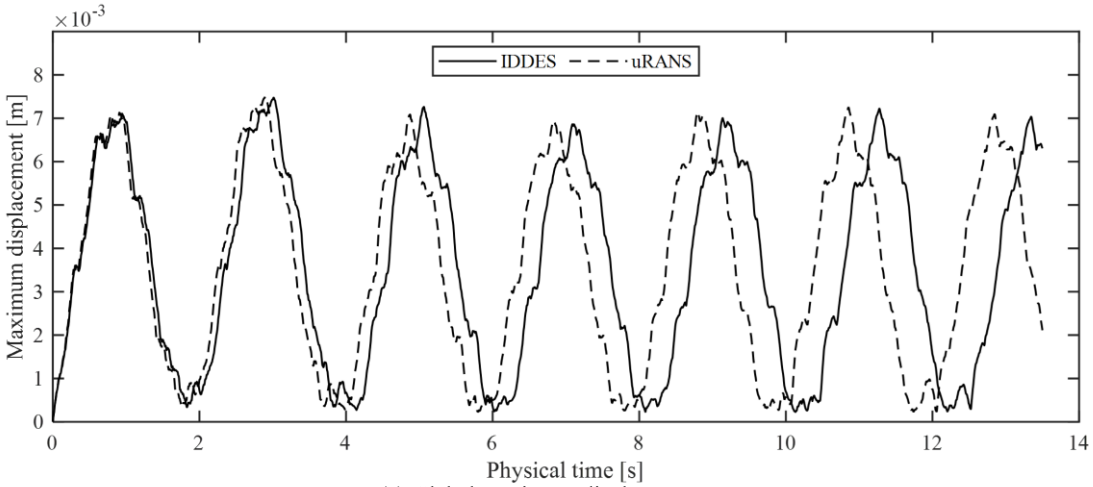

(a) Global maximum displacement.

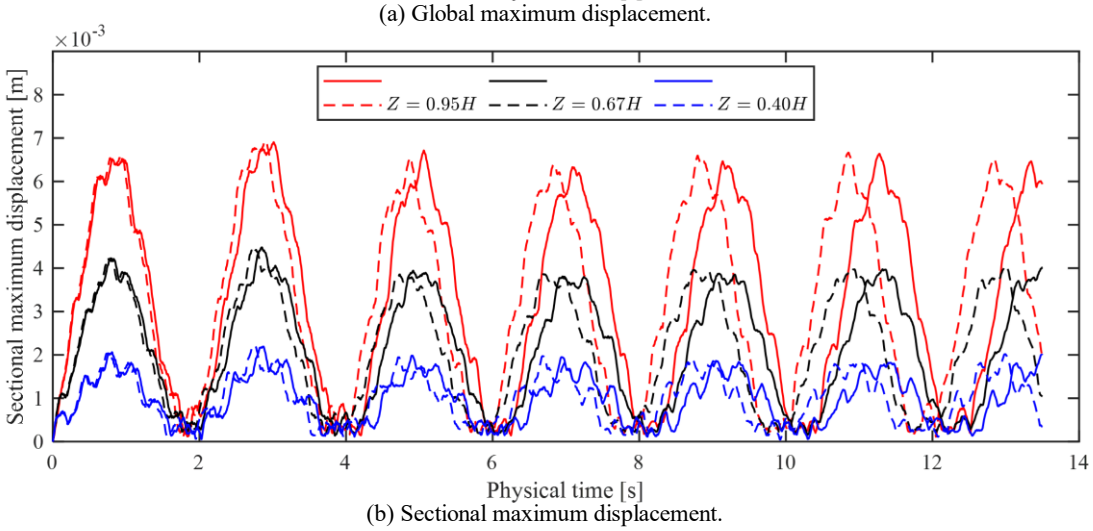

(b) Sectional maximum displacement.

Figure 8. FSI deformation displacement.

The k–ω SST model (Menter, 1993) is applied for both the uRANS and IDDES (Shur et al., 2008) simulations. The turbulence eddy viscosity is computed based on the turbulence kinetic energy and the specific turbulence dissipation rate. The convection term of the model is discretized with a second-order upwind scheme. The k–ω SST model interprets the standard k–ω model within the inner layer of the boundary condition. When reaching the free shear layers, it switches to the k–ϵ model to reduce the sensitivity for the inlet free-stream properties.

With the goal of precisely predicting the flow separation, the IDDES method relating to a hybrid RANS–LES approach, is also used in the simulation compared with uRANS results. With the aim to alleviate the costly near-wall meshing requirements imposed by LES, the boundary-layer flow is treated with RANS and the outer detached eddies are captured by LES.

To clarify the importance of introducing DES-type methods, a pair of fluid–structure interaction (FSI) simulations are performed using uRANS and IDDES, assuming that the sail is a solid aluminum body. In these cases, α is set as 23°. Figure 8 presents the global and sectional maximum displacement of the structure. At the very beginning, since very few cells are calculated by LES, the two methods show very similar results. As physical time goes on, more discretized cells are assigned in the LES region and the differences between the two methods become significant. The uRANS results show a larger damping amplitude: there is a difference in the peak value of around 15% between the two methods. The IDDES results show more high-frequency damping, especially at the lower part of the sail (see the black and blue lines in Figure 8(b)). Shell structures, such as the concept design in Figure 4, are expected to be more sensitive to high-frequency oscillations, so LES or DES-type simulations are necessary.

Take the fully expanded condition with $\alpha = 23°$ as an example. Figure 9 shows the distribution of regions calculated by uRANS and LES. Most areas, especially the boundary flow regions, are calculated by uRANS. The LES regions are mainly distributed in the downstream field. Due to the impact of the tip vortices, fewer areas are calculated by LES when approaching the tip (see Figure 9(a)). This explains why the lower part of the sail shows a more high-frequency structural response in Figure 8.

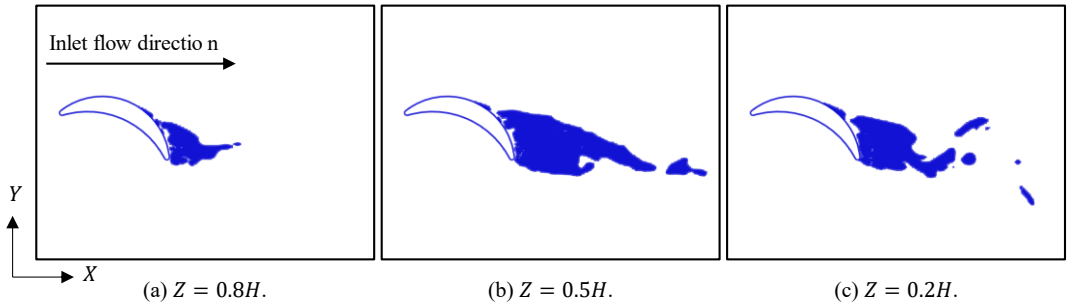

(a) $Z = 0.8H$. (b) $Z = 0.5H$. (c) $Z = 0.2H$.

Figure 9. Distribution of DES upwind blending factor at different spanwise positions, fully expanded condition, $\alpha = 23°$. Blue marks out the regions calculated with LES, while the rest of the computation domain is calculated with uRANS.

The approach of blended wall treatment, which is useful in treating complex geometries with local flow characteristics, is applied to the RANS equations. The traditional low-Re approach is applied, in which the boundary layer is resolved with a finely layered mesh. In the simulations, the order of magnitude of y^+ on most areas of the wall is around 10^{-1}, with the purpose of having a more detailed and accurate representation of the boundary-layer flow.

2.4.2 Solvers and discretization schemes

A finite volume method (FVM) is used to discretize the governing equations by employing a segregated flow solver. The numerical solver uses the Semi-Implicit Method for Pressure-Linked Equations (SIMPLE) algorithm. In STAR-CCM+, this is called the "implicit unsteady solver." The freestream Mach number is less than 0.1, so the flow is regarded as incompressible flow with constant density. A second-order implicit method is used to discretize the time derivative. The scale of the time step is 2×10^{-4} s to keep the Courant number under 10, since an implicit solver is applied. A hybrid second-order upwind scheme and the bounded-central scheme are used to discretize the convection fluxes. The diffusion fluxes are discretized with a second-order scheme. The gradient computation uses the second-order hybrid Gauss-LSQ method.

3. Results and discussion

3.1 Propulsive performance

The force coefficients, representing the external loads on the sail, are analyzed to study the propulsive performance of the rigid wingsail. As can be seen in Figure 10, which presents the boxplots of the force coefficients under the fully expanded condition, the uRANS and IDDES methods provide similar results for the time-averaged force coefficients. The difference between these two methods is usually less than 10% for C_L (Figure 10(a)) and C_D (Figure 10(b)), and 15% for C_M (Figure 10(c)). On the other hand, as mentioned in Section 2.4.1, it is believed that IDDES simulations predict the unsteady characteristics, especially high-frequency properties of the external loads, more accurately due to the strong flow separation phenomena. Based on the IDDES results, it can be concluded that in the studied range of α, the highest C_L is around 2.102 at $\alpha = 23°$. Simulations of the fully retracted condition suggest the same optimal α. The value of C_D, which also contributes to the thrust at board reach, is also higher when $\alpha = 23°$. However, the force coefficients from the uRANS simulations show significantly larger oscillation amplitudes, especially for C_L. The reason for this is explained in Section 3.2.

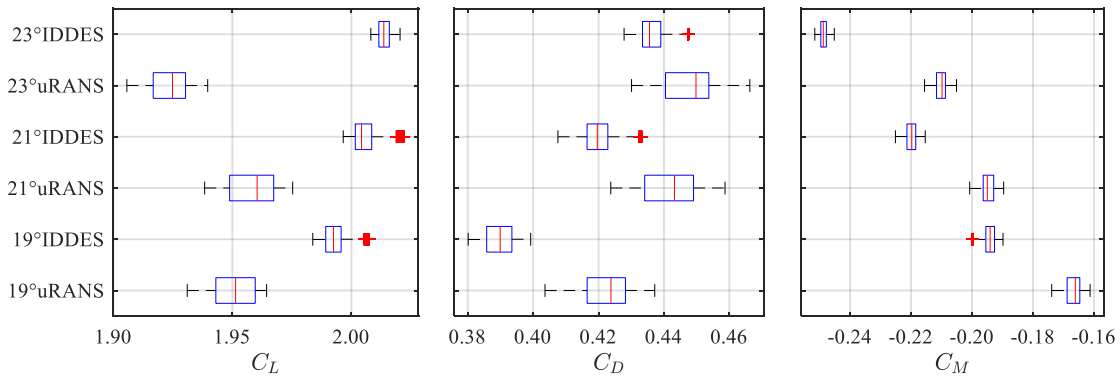

Figure 10. Boxplots of time-averaged force coefficients, fully expanded condition.

Table 3 presents the time-averaged value of the force coefficients based on the IDDES simulations. C_L is around 10% higher under the fully expanded condition, while the C_D values are approximately 17–27% lower. The reason is that when the rigid wingsail is fully retracted, the impact from the tip vortices is much stronger, leading to reduced lift. Section 3.4 discusses the characteristics of the tip vortices and presents some solutions to reduce the negative impacts.

Table 3. Time-averaged force coefficients based on IDDES simulations.

Condition	α [°]	C_L	C_D	C_M
Fully expanded condition	19	2.072	0.385	-0.194
	21	2.069	0.409	-0.217
	23	2.102	0.456	-0.244
Fully retracted condition	19	1.889	0.488	-0.106
	21	1.879	0.510	-0.131
	23	1.914	0.534	-0.161

Based on the time-averaged values of force coefficients from the IDDES simulations, the propulsive performance can be predicted. A single rigid wingsail can provide up to 86 kN of thrust force under the fully expanded condition, and 444 kN under the fully retracted condition. Figure 11 presents C_T at different apparent wind and true wind directions. The value of V_S is 12 kn (around 6.2 m/s). V_{TW} is fixed separately at 8 m/s and 32 m/s for the fully expanded condition and fully retracted conditions, respectively. Although Re varies with the true wind direction, the force coefficients are assumed to remain the same since they are not sensitive to Re. The trend of C_T with different apparent wind directions is similar between the fully expanded condition and the fully retracted condition, as Figure 11(a) shows. It can be seen that the wingsail does not work when $\theta_{AW} < 30°$, which is the luffing point of sail (Rousmaniere, 1999). As shown in Figure 11(b), for the fully retracted condition, the rigid wingsail attains its best propulsive performance when θ_{TW} is 90–120°, that is, when the point of sail is a beam reach. However, for the fully expanded condition, the maximum C_T is obtained when θ_{TW} is around 160°, which is close to the downwind condition.

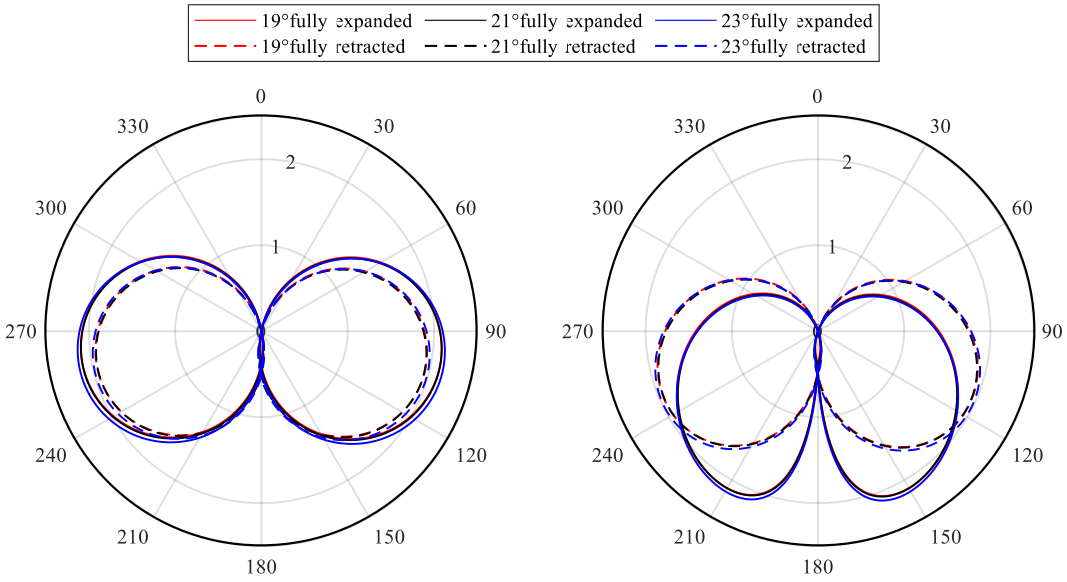

(a) C_T vs. θ_{AW}. (b) C_T vs. θ_{TW}.

Figure 11. Polar diagram of C_T vs. wind directions.

3.2 Flow separation

The flow field induced by the crescent-shaped profile has a remarkable flow separation phenomenon at the suction side close to the trailing edge, which is the reason for the unsteady characteristics. To reduce the influence of the tip vortices (discussed in Section 3.4), the analysis of the flow separation and vortex shedding is based on the fully expanded condition. For clearer presenting and discussing the flow separation phenomenon, the simulation case with the largest α, i.e., $\alpha = 23°$, is taken as the example.

Figure 12, which presents the streamwise velocity distribution and the streamline at the sectional plane with different spanwise positions, shows that the results from uRANS and IDDES share some similarities. For upstream areas of the half chord, that is, on the left of the half chord in the subfigures of Figure 12, the flow is resolved by applying the k–ω SST turbulence model when using both the uRANS and IDDES methods. Therefore, the characteristics of the flow field predicted by the two methods are almost the same. There is a high-velocity region where the streamwise velocity is approximately twice the inlet flow velocity, on the suction side upward of

the half chord, which causes a reduction of pressure and finally leads to the lift force. There is a pronounced low-velocity region on the suction side of the profile, extending to the downstream areas. The observed phenomena support the hypothesis that the IDDES method provides more detailed information on the separating flow since the large eddies are directly resolved instead of being modeled.

As shown in Figure 9, the low-velocity region is mainly calculated by LES when applying the IDDES method. Therefore, the flow field in this area shows some differences between the two methods. The results based on the uRANS method show two main vortices (see Figure 12(a)). At the lower part of the sail, for instance $Z = 0.25H$, the IDDES results also show the main vortices, because the bottom panel with the symmetric boundary condition constrains vortex development in the spanwise direction. However, at the higher part of the sail, such as $Z = 0.50H$ and $Z = 0.75H$, the flow shows more complex characteristics in the IDDES results (see Figure 12(b)).

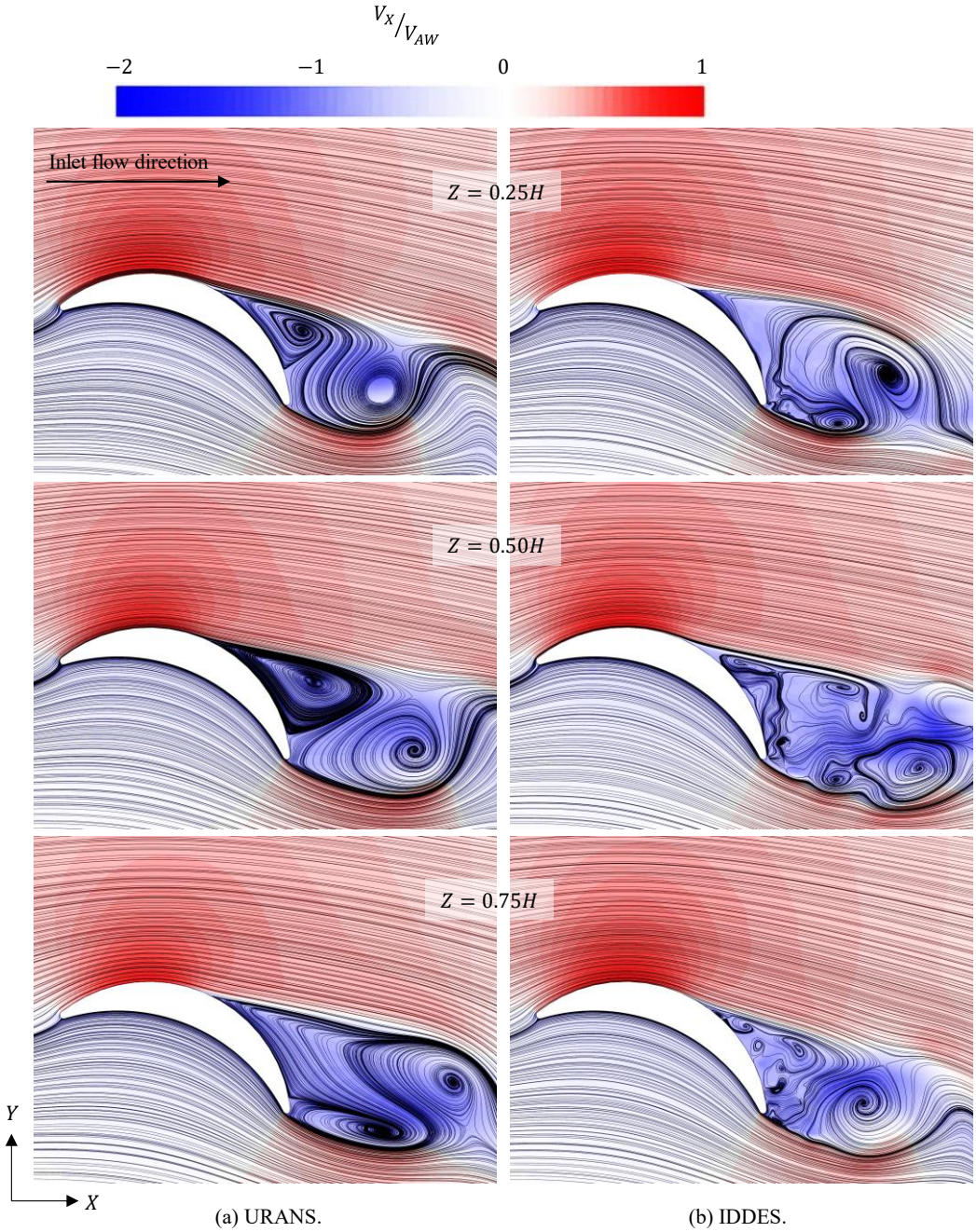

(a) URANS. (b) IDDES.

Figure 12. V_X distribution and streamlines at different spanwise sections, fully expanded condition, $V_{AW} = 8$ m/s, $\alpha = 23°$.

The pressure distributions on the surface of the rigid wingsail are shown in Figure 13 alongside the flow separation/attachment lines. There are multiple flow separation points on the suction side close to the trailing edge. For the IDDES results, the distribution of the flow separation lines shows random properties in the spanwise direction, which further explain the complex separating flow in Figure 12(b). The flow separation areas narrow in

the crossflow direction when the position is near the tip because of the phenomenon of tip vortices. There are also some flow separation/attachment lines on the pressure side near the edges.

Although the flow separation lines are not uniformly developed, the pressure coefficient is evenly distributed along the spanwise direction, except in the region near the tip. The low-pressure areas located at the suction side approaching the leading edge coincide with the high-velocity areas in Figure 12, which mainly contribute to the lift force. It can be inferred that the loads on the surface of the rigid wingsail will make the structure suffer from deformation, especially bending. Meanwhile, the multiple flow separation points cause oscillations of the external loads, which may lead to vortex-induced vibrations.

Periodic oscillations are evident from the time history of the C_L values in the uRANS simulations, presented in Figure 14(a). In contrast, the oscillations are quite random, without a clear period, in the IDDES simulations. Referring to the FSI simulations in Section 2.4.1, these irregular oscillations explain the high-frequency damping found in the IDDES results.

Therefore, to study the unsteady properties of the force coefficients, FFT analysis is conducted. Figure 15 presents the FFT analysis results for C_L under the fully expanded condition. The length of physical time of the selected data is 10 s, so the first peak with the frequency of 0.1 Hz is spurious and can be ignored. When looking at the dashed lines, a second set of peaks is evident with frequencies around 0.4 Hz, so the uRANS simulations indicate that C_L has a clear oscillating period of 2.5 s and an amplitude of approximately 0.02. The C_L values predicted by the IDDES simulations do not show periodic oscillations. In Figure 15(b), in which the FFT plot is zoomed in at the low-frequency region, the second set of peaks is unclear for the solid lines. Some small oscillations can also be found on the solid lines in the high-frequency region of the FFT results, shown in Figure 15(c). The time history and FFT results of C_D and C_M, as well as those under the fully retracted condition, show similar characteristics.

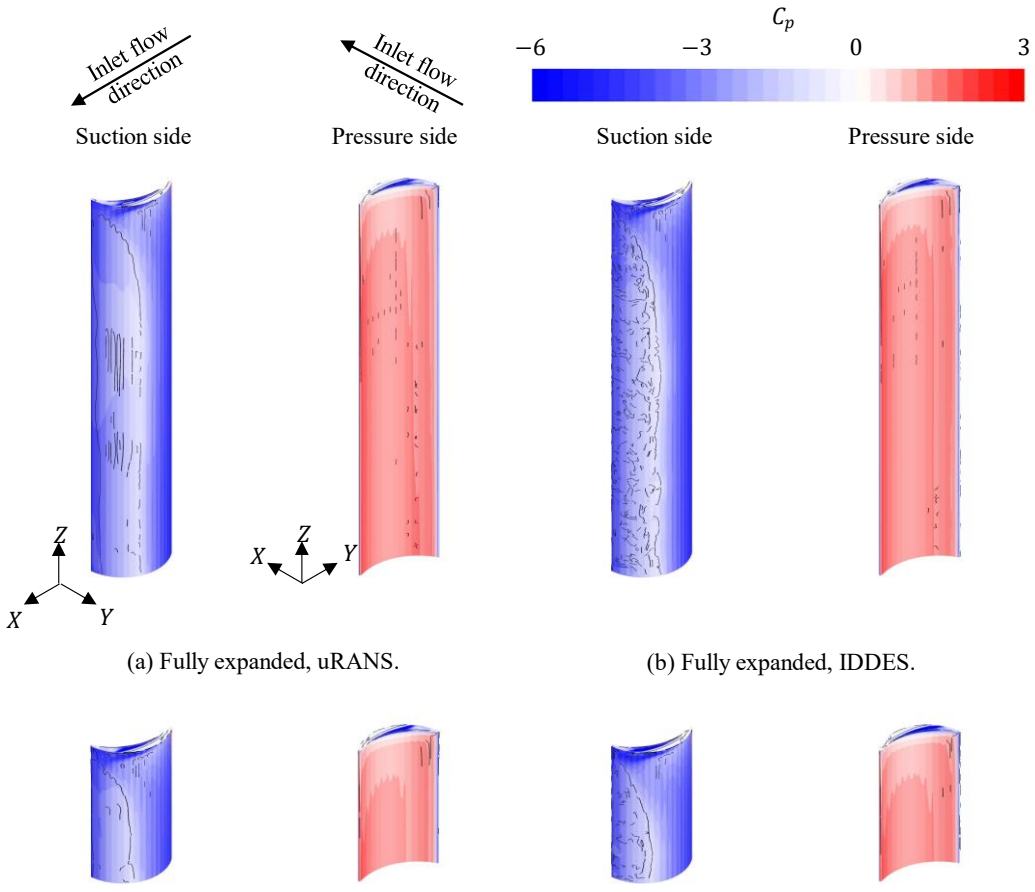

(a) Fully expanded, uRANS. (b) Fully expanded, IDDES.

(c) Fully retracted, uRANS. (d) Fully retracted, IDDES.

Figure 13. C_p distributions and the flow separation/attachment lines, $\alpha = 23°$. For the fully expanded condition, $V_{AW} = 8$ m/s, while for the fully retracted condition, $V_{AW} = 32$ m/s.

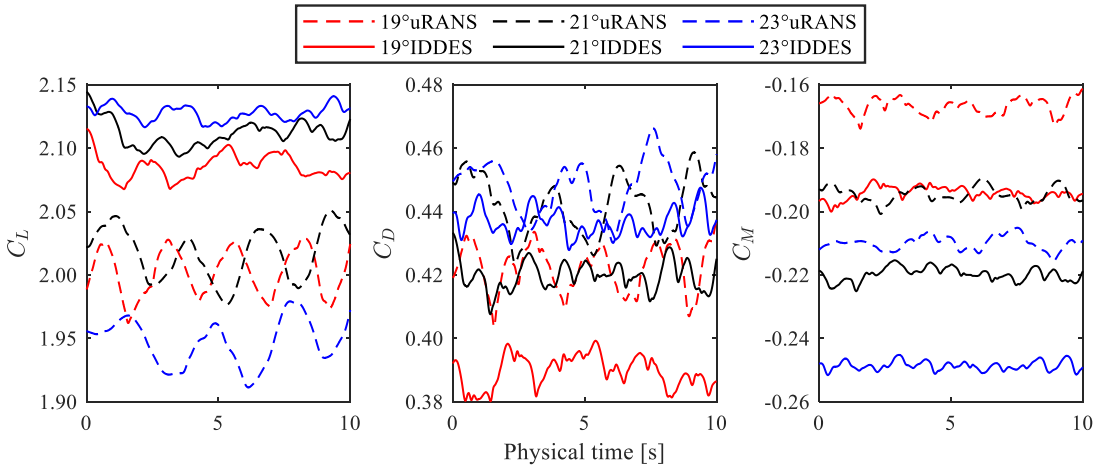

(a) (b) (c)

Figure 14. Simulation time history of the force coefficients, fully expanded condition.

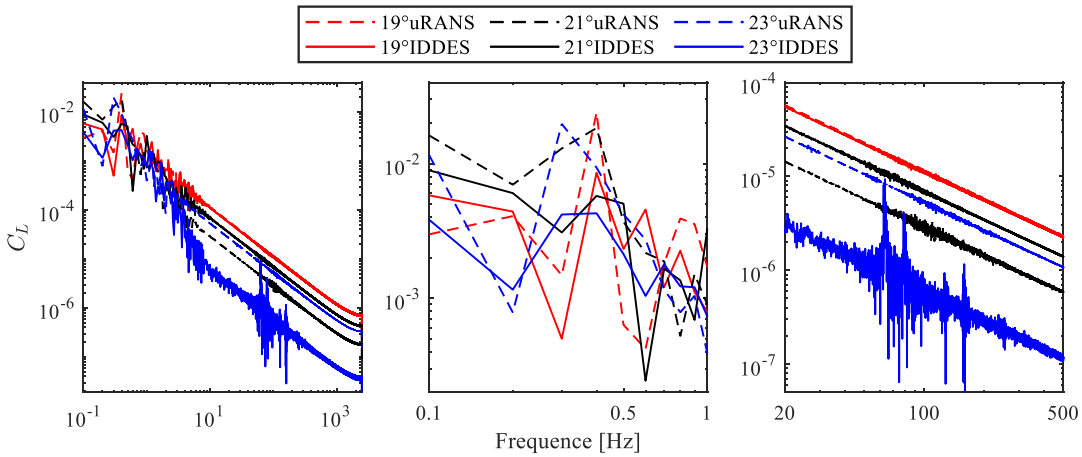

(a) All frequency range. (b) Low frequency range. (c) High frequency range.

Figure 15. FFT results of C_L, fully expanded condition.

3.3 Wake flow

Normally, more than one wingsail is installed and operated on a ship. The analysis of the wake flow is expected to provide some guidance in future studies on ships with multiple sails. The wake flow resolved by the two methods shows many differences. In this Section, results under fully expanded condition are selected as samples. The IDDES simulations predict a flow field with much more complex vortex structures, as shown in Figure 16, which shows the distribution of ω_X^* on the iso-surfaces of $Q = 5\ \mathrm{s}^{-2}$. From the uRANS simulations, as Figure 16(a) shows, the spanwise vortex tubes can be easily observed, which means that the vortex shedding phenomena do not show significant spanwise characteristics, except for the tip vortices. However, the vortices have numerous streamwise and crossflow structures when applying the IDDES method, as shown in Figure 16(b). These complex vortex structures lead to the unclear oscillating period described in Section 3.2.

When looking at the ω_Z distribution at section planes with different streamwise positions, shown in Figure 17, the differences between the results simulated by the two methods are more readily apparent. The uRANS results show some vertical vortex tubes: for example, in Figure 17(a), when $X/L_C = 0.5$, that is, just behind the trailing edge, a strong vortex tube can be found. However, when using the IDDES method (see Figure 17(b)), there are small vortices on the decimeter scale at the section plane of $X/L_C = 0.5$. When looking at the position $X/L_C = 1.0$, the distribution of ω_Z is preserved in Figure 17(a), while for the IDDES results, it can only be found in the lower part close to the bottom panel. Moreover, the vortices dissipate quickly in the wake region when applying the uRANS method, which indicates that there is more energy loss. The turbulent kinematic energy in the wake region is much lower when applying the IDDES method. When looking at the streamwise position of $X/L_C = 2.0$, the vortices predicted by the IDDES method are still noticeable, while those predicted by uRANS are almost dissipated.

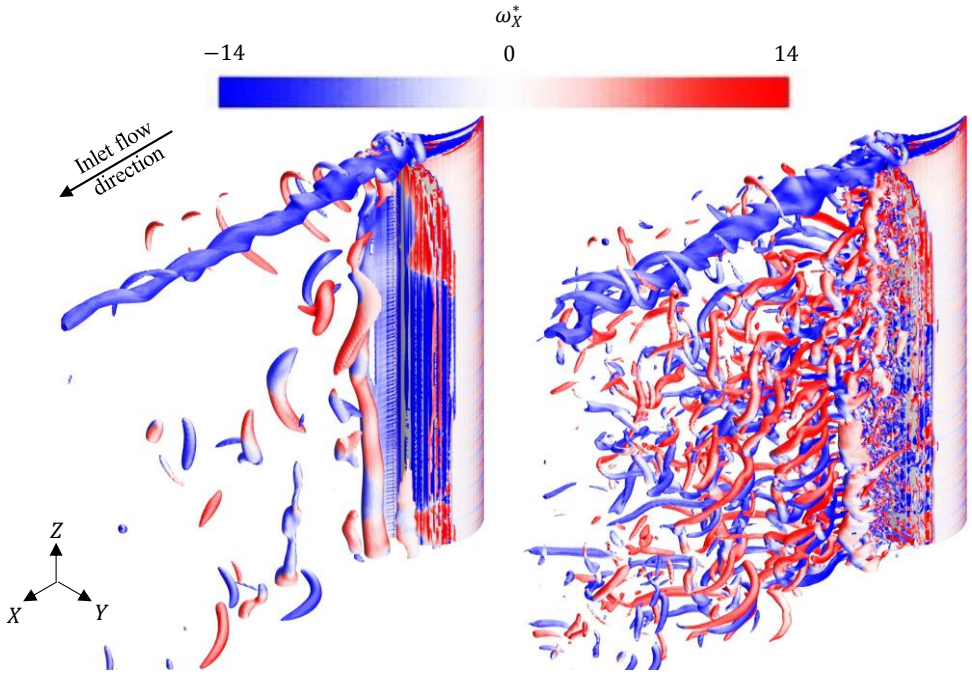

(a) URANS. (b) IDDES.

Figure 16. Non-dimensional ω_X distribution on iso-surfaces of the Q-criterion $Q = 5\ \mathrm{s}^{-2}$, fully expanded condition, $V_{AW} = 8\ \mathrm{m/s}$, $\alpha = 23°$.

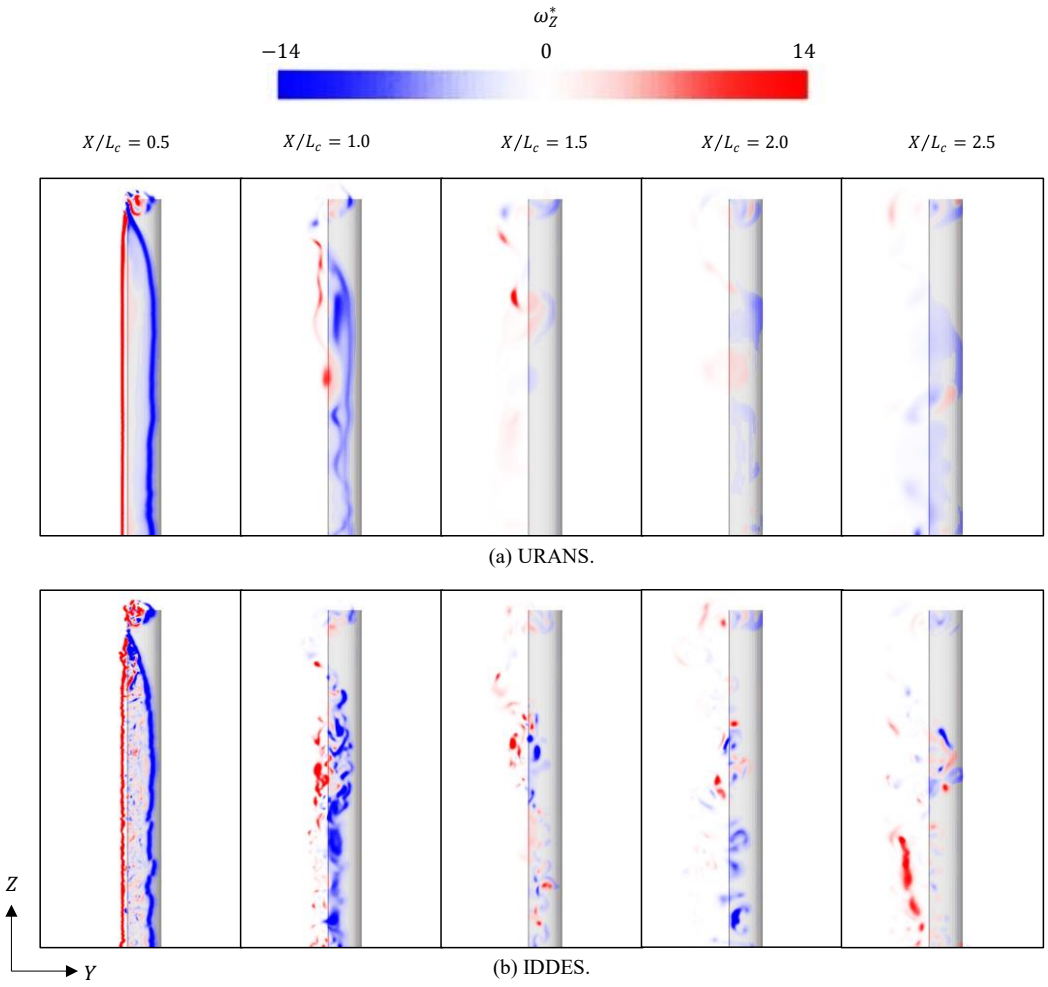

(a) URANS.

(b) IDDES.

Figure 17. Non-dimensional ω_Z distribution at different streamwise positions in the wake field, fully expanded condition, $V_{AW} = 8\ \mathrm{m/s}$, $\alpha = 23°$. The inlet flow orients in the direction perpendicular to the paper/screen pointing outwards.

Vortex shedding can bring advantages and disadvantages. Usually, for airplane wings or propeller blades, only the lift force is desired, so it would be preferable to avoid the vortex shedding and the associated drag force. However, for the rigid wingsails installed and operated on ships, both the lift and drag forces can contribute to the thrust, especially when the point of sail is a broad reach, that is, when θ_{TW} is around 135°. Compared with rigid wingsails based on conventional airfoil profiles, whose C_T is around 1.5 – 2.0, a substantially higher C_T is attained by applying this crescent-shaped profile with significant camber. On the other hand, vortex shedding brings challenges to the structure of the wingsail. To capture more propulsive force, the external loads, including the vertical moment, are much stronger. Meanwhile, the loads are not steady but always oscillate through time.

3.4 Tip vortices

It is believed that tip vortices have notable negative effects on propulsive performance. From Figure 13, it can be found that the pressure on the pressure side is lower when it is close to the tip, leading to a reduction in the lift force. Therefore, some actions are suggested to release the phenomenon of tip vortices. For example, a top-mounted disc installed on the tip would likely improve the propulsive performance.

As can be seen in Figure 16, there are significant vortices induced by the tip of the rigid wingsail. By plotting ω_X^* at several different streamwise positions around the tip (Figure 18), two tip vortices, the tip separation vortex and the tip leakage vortex, can be found developing at the suction side and the pressure side, respectively. According to the uRANS simulations as well as previous studies (Zhu et al., 2022), the two vortices combine at around the half chord into a single vortex with a more complex internal flow structure. Nevertheless, in the IDDES results, the two vortices do not combine. The tip leakage vortex is much stronger than the tip separation vortex, which dissipates quickly at around the half chord. Due to the higher apparent wind speed, the tip vortices are stronger under the fully retracted condition. However, when comparing the dimensionless value of ω_X, the distribution is quite similar between the two conditions.

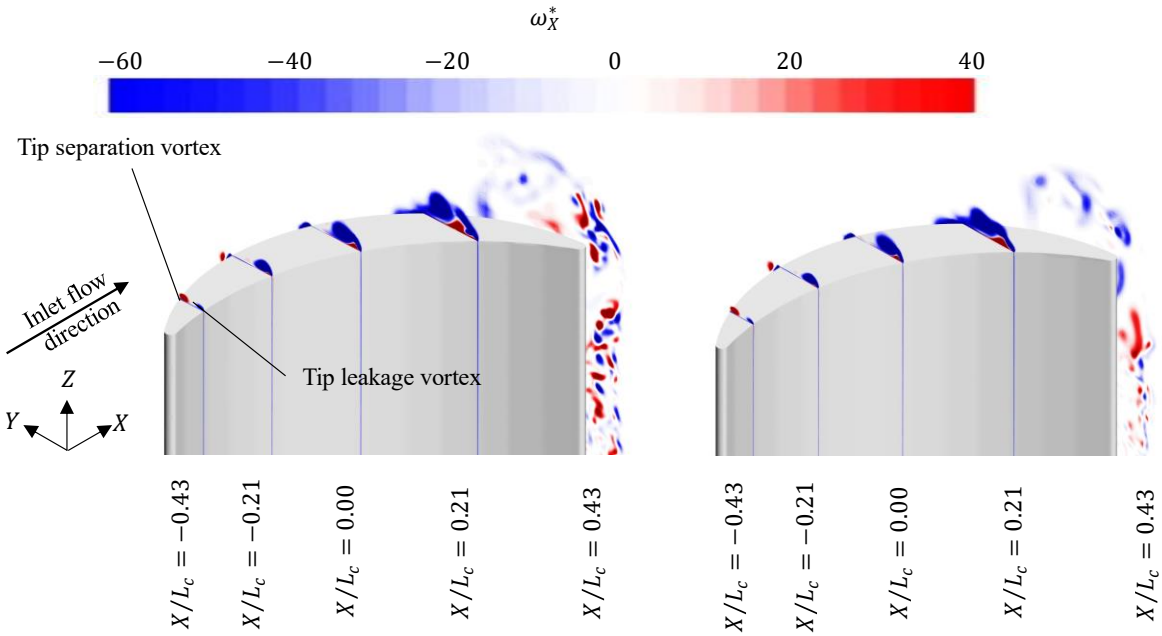

(a) Fully expanded condition. (b) Fully retracted condition.

Figure 18. Non-dimensional ω_X distribution at different streamwise positions around the tip, based on the IDDES simulations, $\alpha = 23°$. For the fully expanded condition, $V_{AW} = 8$ m/s, while for the fully retracted condition, $V_{AW} = 32$ m/s.

A disc plate, which extends 1 m from the boundary of the top section and is 0.1 m in thickness, is installed upon the top of the sail, as Figure 19(a) shows. An extra CFD simulation based on IDDES method is performed to study the effect of this disc plate. In this case, α is 23°, and the physical condition is the fully expanded condition. By having this disc plate, C_L increases around 1%. When looking at the ω_X distribution in Figure 19(b), the tip separation vortex developing on the suction side almost disappears; however, the tip leakage vortex developing on the pressure side is still quite strong. This could be because the scale of the tip leakage vortex is around 1.5 m, which is larger than the extension of the disc plate from the sail. A previous study compared the CFD results of a crescent-shaped wingsail with and without a freestream tip (Zhu et al., 2022), indicating that the loss of C_L due to the freestream tip is about 6%. Therefore, the shape of the tip can still be further optimized to obtain a higher C_L.

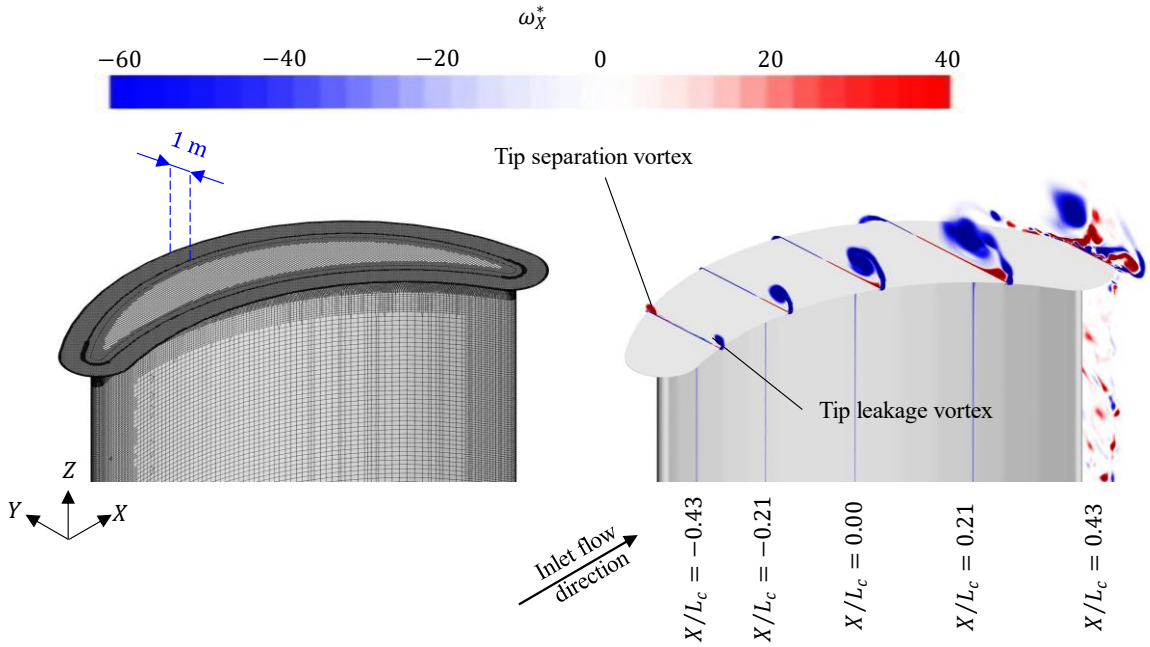

(a) Geometry and mesh. (b) Distribution of non -dimensional ω_X.

Figure 19. Geometry, mesh, and effects of the disc on top based on IDDES simulations, fully expanded condition, $V_{AW} = 8$ m/s, $\alpha = 23°$.

4. Conclusions

This study aimed to develop an improved high-fidelity CFD model for rigid wingsails with crescent-shaped sectional profiles. The improved model not only predicts the propulsive performance, but also unveils the high-frequency and wake characteristics of the flow field, which could be important for further FSI and multiple-sail studies. The telescopic function of the wingsails was also studied, for a range of different angles of attack, by comparing the propulsive performance under the fully expanded and the fully retracted conditions. The computational methods used were uRANS and IDDES with the $k-\omega$ SST turbulence model. The flow separation, vortex shedding in the wake region, and tip vortices were analyzed. The outcome of this study provides guidance for further studies on structural analysis, FSI analysis, multi-sail interaction analysis, and profile optimization of telescopic wingsails.

For the time-averaged force coefficients, which are the main determinant of propulsive performance, uRANS and IDDES had a similar prediction. The maximum C_L was obtained when α was $23°$. For the fully expanded condition, the lift and drag coefficients based on the IDDES results were 2.102 and 0.456, respectively, while when the sail was fully retracted, C_L and C_D changed by -8.9% and 17.1%. Therefore, wingsails with a crescent-shaped profile can achieve significant propulsive performance.

However, the external loads predicted by the two methods show different unsteady characteristics, which are believed to have a non-negligible influence on the structural response. From the FFT analysis, the results based on uRANS showed clearer low-frequency oscillations than those based on IDDES, while the IDDES results showed some high-frequency characteristics of the external loads. The high-frequency oscillations may lead to local vibration or buckling of the structures, which could be studied in a future FSI analysis. This difference is likely because the IDDES method can provide more detailed information about the flow field, especially the vortex shedding in the wake region, because large-scale eddies are solved without modeling.

Vortex tubes extending in the spanwise direction could be detected in the uRANS results, but the structure of the vortex is quite complex in the IDDES results. The IDDES method also indicated less dissipation and energy loss in the wake region, due to which vortex structures could be clearly seen 42 m (3 times the chord length) downstream of the sail. It can be inferred that the wake flow can cause interactions among sails on a ship with multiple sails.

Meanwhile, the negative effects on the propulsive performance due to tip vortices are significant, especially when the sail is retracted. Having a disc plate on the top of the sail can increase C_L by 1%, but further optimization of the tip geometry should be studied in the future.

Acknowledgments

This work was performed within the project WindStruc (Wind-assisted propulsion for commercial vessels) funded by the Swedish Energy Agency through

contract agreement no. 51552-1, co-funded by ScandiNAOS AB and Stena Rederi AB. During the process of this study, Bengt Ramne from ScandiNAOS AB put forward the concept design of the sail, and Carl-Erik Janson from Chalmers University of Technology also offered guidance supporting the CFD simulations and propulsive analysis. The computations and data handling were enabled by resources provided by the Swedish National Infrastructure for Computing (SNIC), partially funded by the Swedish Research Council through grant agreement no. 2018-05973.

Disclosure statement

The authors report there are no competing interests to declare.

References

Atkinson, G. M. (2019). Analysis of lift, drag and CX polar graph for a 3D segment rigid sail using CFD analysis. *Journal of Marine Engineering and Technology*, *18*(1), 36–45. https://doi.org/10.1080/20464177.2018.1494953

Blount, H., & Portell, J. M. (2021). *CFD investigation of wind powered ships under extreme conditions* [Chalmers University of Technology]. https://odr.chalmers.se/handle/20.500.12380/304254

Davidson, L. (2019). *Fluid mechanics, turbulent flow and turbulence modeling*. Division of Fluid Dynamics, Department of Mechanics and Maritime Sciences, Chalmers University of Technology.

EUROSTAT. (2019). *Greenhouse gas emissions by source sector*. EUROSTAT.

Hamada, N. (1985, November). The development in Japan of modern sail-assisted ships for energy conservation. *Regional Conference on Sail-Motor Propulsion*. https://trid.trb.org/view/400086

IMO. (2018). *Interpretation of Initial IMO Strategy on Reduction of GHG Emissions from Ships* (Vol. 60, Issue 1, pp. 195–201).

International Chamber of Shipping. (2014). *Shipping, world trade and the reduction of CO2 emissions*. London: International Chamber of Shipping.

International Transport Forum. (2020). *Navigating towards cleaner maritime shipping*. OECD Publishing. www.itf-oecd.org

Khan, L., Macklin, J., Peck, B., Morton, O., & Souppez, J.-B. R. G. (2021, September 15). A review of wind-assisted ship propulsion for sustainable commercial shipping: Latest developments and future stakes. *Proceedings of the Wind Propulsion Conference 2021*.

Kimball, J. (2009). *Physics of Sailing*. CRC Press. https://doi.org/10.1201/9781420073775

Lee, H., Jo, Y., Lee, D. J., & Choi, S. (2016). Surrogate model based design optimization of multiple wing sails considering flow interaction effect. *Ocean Engineering*, *121*, 422–436. https://doi.org/10.1016/j.oceaneng.2016.05.051

Lu, R., & Ringsberg, J. W. (2020). Ship energy performance study of three wind-assisted ship propulsion technologies including a parametric study of the Flettner rotor technology. *Ships and Offshore Structures*, *15*(3), 249–258. https://doi.org/10.1080/17445302.2019.1612544

Ma, Y., Bi, H., Gan, R., Li, X., & Yan, X. (2018). New insights into airfoil sail selection for sail-assisted vessel with computational fluid dynamics simulation. *Advances in Mechanical Engineering*, *10*(4), 1–12. https://doi.org/10.1177/1687814018771254

Menter, F. R. (1993). Zonal two equation κ-ω turbulence models for aerodynamic flows. *AIAA 23rd Fluid Dynamics, Plasmadynamics, and Lasers Conference, 1993*. https://doi.org/10.2514/6.1993-2906

Nikmanesh, M. (2021). *Sailing performance analysis using CFD simulations: A study on crescent shaped wing profiles* [Chalmers University of Technology]. https://odr.chalmers.se/handle/20.500.12380/304303

Rousmaniere, J. (1999). *The Annapolis Book of Seamanship:: Completely Revised, Expanded and Updated*. Simon and Schuster.

Sauzé, C., & Neal, M. (2008). Design considerations for sailing robots performing long term autonomous oceanography. *Proceedings of the International Robotic Sailing Conference*, *27*(2), 21–29. www.roboticsailing.org

Shur, M. L., Spalart, P. R., Strelets, M. K., & Travin, A. K. (2008). A hybrid RANS-LES approach with delayed-DES and wall-modelled LES capabilities. *International Journal of Heat and Fluid Flow*, *29*(6), 1638–1649. https://doi.org/10.1016/j.ijheatfluidflow.2008.07.001

Siemens PLM Software. (2021). *STAR-CCM+ user guide (version 16.02)*. Siemens PLM Software Inc: Munich, Germany.

Silva, M. F., Friebe, A., Malheiro, B., Guedes, P., Ferreira, P., & Waller, M. (2019). Rigid wing sailboats: A state of the art survey. *Ocean Engineering*, *187*, 106150. https://doi.org/10.1016/j.oceaneng.2019.106150

Smagorinsky, J. (1963). General circulation experiments with the primitive equations. *Monthly Weather Review*, *91*(3), 99–164. https://doi.org/10.1175/1520-0493(1963)091<0099:gcewtp>2.3.co;2

Tillig, F., & Ringsberg, J. W. (2020). Design, operation and analysis of wind-assisted cargo ships. *Ocean*

Engineering, *211*, 107603. https://doi.org/10.1016/j.oceaneng.2020.107603

Traut, M., Gilbert, P., Walsh, C., Bows, A., Filippone, A., Stansby, P., & Wood, R. (2014). Propulsive power contribution of a kite and a Flettner rotor on selected shipping routes. *Applied Energy*, *113*, 362–372. https://doi.org/10.1016/j.apenergy.2013.07.026

Workinn, D. (2021). *A high-level interface for a sailing vessel* [KTH Royal Institute of Technology]. http://urn.kb.se/resolve?urn=urn:nbn:se:kth:diva-299430

Zhu, H., Nikmanesh, M. B., Yao, H. D., Ramne, B., & Ringsberg, J. W. (2022). Propulsive Performance of a Novel Crescent-Shaped Wind Sail Analyzed With Unsteady Rans. *Proceedings of the International Conference on Offshore Mechanics and Arctic Engineering - OMAE*, *7*. https://doi.org/10.1115/OMAE2022-79867

Paper III

Structure Analysis of Lightweight Sail Structures for Wind-Assisted Ship Propulsion

Advances in the Analysis and Design of Marine Structures – Ringsberg & Guedes Soares (Eds)

Structure analysis of lightweight sail structures for wind-assisted ship propulsion

H. Zhu, S. Bikkireddy, J.W. Ringsberg & H.-D. Yao
Division of Marine Technology, Department of Mechanics and Maritime Sciences, Chalmers University of Technology, Gothenburg, Sweden

B. Ramne
ScandiNAOS AB, Gothenburg, Sweden

ABSTRACT: Wind-assisted ship propulsion systems, such as rigid wingsails, are a promising means to reduce greenhouse gas emissions from shipping. This study uses quasistatic finite element analysis to simulate the structural responses of a crescent-shaped wingsail rig. A few conceptual designs for telescopic rigs are compared, ranging from a rig with a central mast to a mastless rig. The rigs are assessed against three criteria regarding their displacement, strength, and weight. External wind loads are applied to the sails based on the results of aerodynamic simulations in prior studies. The advantages and disadvantages of each concept are discussed, with the aim of providing a strategy for the structural design and arrangement of wind-assisted ship propulsion systems. The results of the study could be used in future work as a basis for structural optimization and fluid–structure interaction analysis.

1 INTRODUCTION

Wind-assisted propulsion for commercial shipping, for example using rigid wingsails (Lu & Ringsberg, 2020), converts the kinetic energy of wind into thrust (Shukla & Ghosh, 2009). It is regarded as one of the most promising ways to reduce greenhouse gas emissions from shipping, with the purpose of achieving the International Maritime Organization (IMO) target of reducing greenhouse gas emissions from shipping by 50% by 2050, relative to 2018 levels (IMO, 2018). The wingsail and its rig must have a lightweight design to reduce the influence on the ship's cargo capacity and to fulfill stability requirements. One challenge is that the wind loads acting on such a sail cause bending and torsion of its structure, which raises the required strength-to-weight ratio of the sail rig. Section profiles with large camber, like crescent-shaped profiles, have been introduced to generate high lift force coefficients compared to other wingsail profiles (Nikmanesh, 2020). However, the crescent-shaped profile can cause significant flow separation, leading to periodic oscillations of the external loads acting on the sail.

The wingsail is usually supported by a mast installed on the deck of the ship, so its structural response is similar to a cantilever which is subjected to a flow of air. In recent years, some researchers have performed structure analysis on wind-assisted ship propulsion systems, though most of the studies that evaluated wing-assisted ship propulsion systems focused on the fluid aspect. Ouchi et al. (2011, 2013) proposed a conceptual design for a telescopic rigid wingsail and used finite element analysis (FEA) to analyze the deflection and stress distribution throughout the wingsail. He et al. (2015) investigated the structure design, dynamic performance, and control strategy of wingsails for large, oceangoing, sail-assisted ships.

Due to the strong flow separation (Zhu et al., 2022a), the structure of the wingsail will have deformation, which can in turn affect the flow field. Therefore, it is necessary to analyze the fluid–structure interaction (FSI) of the wingsail. In practice, the structure of the wingsail is usually complex and includes panels, stiffeners, and horizontal section plates. To carry out FSI analysis, the structural model should be simplified: otherwise, the fluid mesh of the prism layers may need to be regenerated at every timestep to resolve the boundary layer flow and prevent the coupled simulation from diverging, which is computationally expensive. Therefore, the structural response of the full structure should be analyzed first to guide how the geometry of the structure can be simplified when performing FSI analysis. Moreover, since the wingsail is installed on the deck and is of a considerable size, its weight must be kept as low as possible, otherwise the cargo capacity and the stability of the hull may be affected.

DOI: 10.1201/9781003399759-36

In this study, quasistatic FEA is performed to study the structural responses of a crescent-shaped wingsail rig. A few conceptual designs of telescopic rigs, including different structural designs and material arrangements, are analyzed and compared by considering three criteria: rigidity, strength, and weight. The external wind loads applied to the sails in the structure analysis are obtained from aerodynamic simulations performed in a previous study (Zhu et al., 2022b). The advantages and disadvantages of each concept are discussed, aiming to provide a good strategy for the structural design and arrangement of wind-assisted ship propulsion systems. The results of the study could be used in future work as a basis for structural optimization and FSI analysis.

2 METHODOLOGY

2.1 *Concept design*

The rigid wingsail is designed to have a telescopic function, which means that the wingsail can be expanded or retracted according to the wind conditions. For example, when the wind speed is low, the wingsail can be fully expanded to capture as much wind power as possible, while it can be retracted when the wind speed is high to protect the wingsail structure from damage. The wingsail is divided into four sections, as shown in Figure 1. In this study, the lowest section is named "section 1," and the highest one is named "section 4." The horizontal sectional profile is crescent-shaped, which can generate a higher lift force coefficient than the traditional NACA airfoil series. The chord length of the sectional profile (L_c) is 14m, and the fully expanded height of the wingsail (H) is 75m, excluding the mast which extends 4m outside the wingsail.

Throughout this paper, a global Cartesian coordinate system is used, in which the origin is at the center of the bottom of the mast, the X axis points in the chordwise direction, the Y axis points from the pressure side to the suction side, and the Z axis is in the vertical direction, pointing from bottom to top.

For the shell structures, a series of local coordinate systems are defined (Dassault Systemes Simulia, 2020), as shown in Figure 2. The X axis is projected on to the surface in question. This line represents the local x direction. If the global X axis is within 0.1° of the normal to the surface, the local x direction is the projection of the global Z axis onto the surface. The local y direction is the at right angles to the local x direction, so that the local x direction, local y direction and the positive normal to the surface form a right-handed set.

In Figure 1, two concept designs are presented. One of the concepts aims to use the global shell structure to bear the global bending; a number of vertical stiffeners are used to increase the strength and rigidity of the wingsail structure. To release the stress concentration at the mast as well as the lower part of section 1, some web structures are introduced.

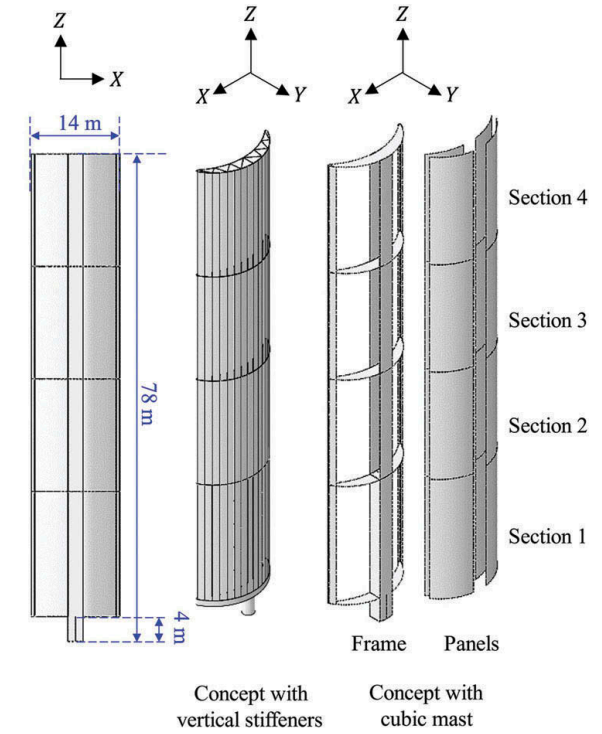

Figure 1. Size and structural arrangements.

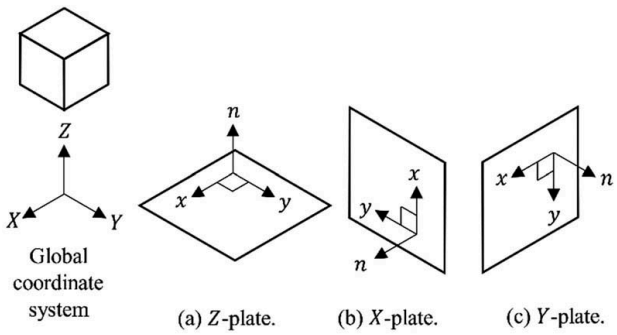

Figure 2. Local coordinate systems for shell structures.

Aiming to avoid the stress concentration in the mast and reduce the weight of the wingsail rig, another concept with a cubic mast is considered, as shown in Figure 1. The entire structure can be divided into two parts, the frame, which is expected to bear the global bending and torsion, and the panels, which are assumed only to suffer from the local wind pressure. The mast only extends to the lowest section.

Figure 3 presents some terminology used in this study. The vertical structures include the edges, the center plates, and the mast. The vertical structures are believed to play the most important role in bearing the global bending. The horizontal structures, which are expected to cut the axial length and thus avoid buckling, include the top, the section plates, and the bottom. The horizontal structures also help protect the shape of horizontal sections which generate the thrust force.

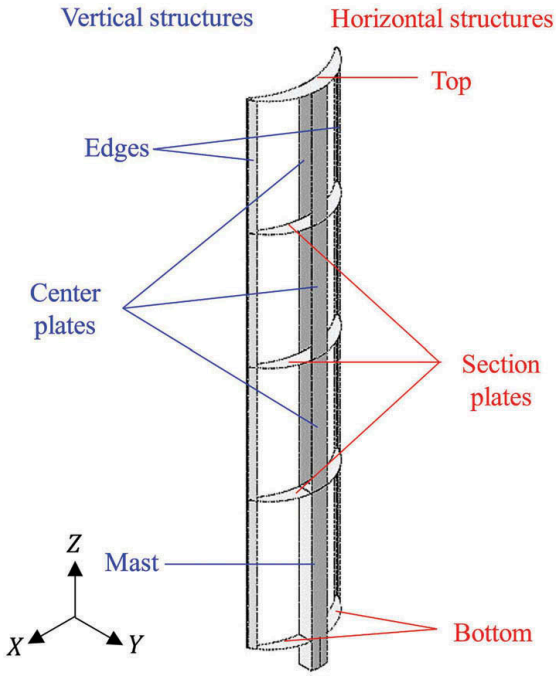

Figure 3. Terminology.

2.2 *Evaluation criteria*

In this study, three properties of each structure are evaluated: its weight, strength, and rigidity.

The total weight of the wingsail must be as low as possible.

The maximum von Mises stress (σ_{Mises}) should not exceed the yield stress. Including a factor of safety of 2, the allowable von Mises stress for steel (S275 (BS EN, 2004)) is 140 MPa, while the allowable stress for aluminum (6061-T4 (ASTM, 2004)) is 105 MPa. The maximum normal stress should not exceed the buckling stress. The maximum shear stress should be less than 50% of the allowable von Mises stress, that is, the allowable shear stress is 70 MPa for steel and 53 MPa for aluminum.

Rigidity or flexibility is also relevant because if the structure is not rigid enough, the telescope function will not work. The maximum deflection, which usually occurs at the tip, should not be larger than 5% of the height. In the fully expanded state, the maximum allowable tip deflection is 3.7 m. The relative displacement of the panels should not exceed half of the mast diameter (i.e., 1 m).

2.3 *Physical conditions*

2.3.1 *External loads*

For the fully expanded wingsail, the structure analysis is based on the wind conditions presented in Table 1, where V_{AW} represents the apparent wind speed, μ represents the dynamic viscosity of air, and ρ_{air} represents air density. According to computational fluid dynamics (CFD) results in a previous study (Zhu et al., 2022b), the lift force coefficient (C_L) is 2.10. The external load applied on the wingsail is divided into two parts: the pressure force on the pressure side and the suction force on the suction side, both of which are assumed to be uniformly distributed across the surface of the wingsail. Based on the CFD results, the magnitude of the total force on the suction side is approximately twice that on the pressure side.

Table 1. Wind conditions.

Property	Value	Unit
V_{AW}	16	[m/s]
μ	$1.85508 \times 10^{-5}1$	[Pa · s]
ρ_{air}	1.184151.18415	[kg/m^3]

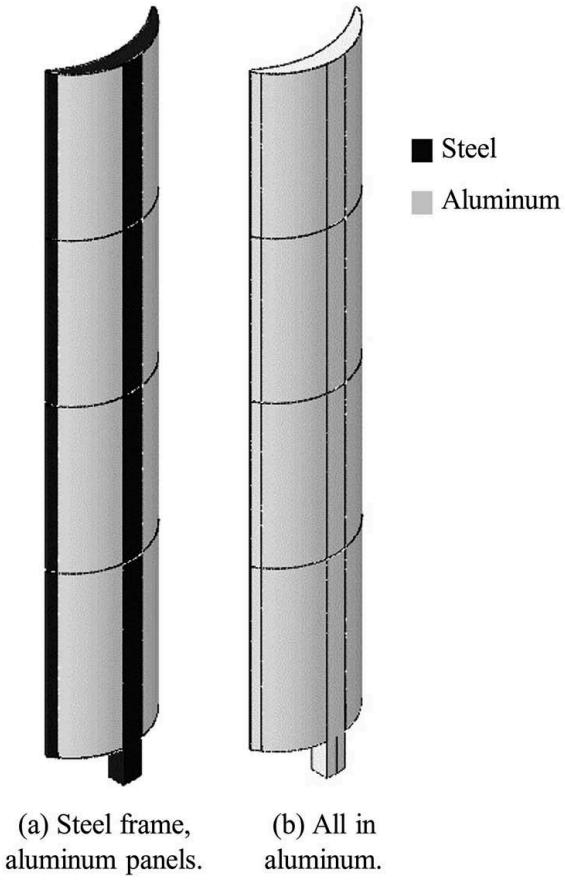

Figure 4. Material arrangement of the concept with a cubic mast.

Table 2. Material properties.

	ρ	E	υ	σ_{yield}
Material	[kg/m^3]	[GPa]	[-]	[Mpa]
Steel (S275) (BS EN, 2004)	7850	210	0.30	275
Al (6061-T4) (ASTM, 2004)	2700	69	0.33	210

For the concept with vertical stiffeners, since the whole surface needs to be strong enough to withstand the global bending, all parts of the wingsail are made of steel. However, aluminum is introduced for the concept with a cubic mast in order to reduce the total weight of the structure. The properties of the materials considered in this study are listed in Table 2, where ρ is the density of the material, E is the Young's modulus, υ is Poisson's ratio, and is the yield stress. For the concept with a cubic mast, two material arrangements are studied. One is "steel frame, aluminum panels," and the other is "all in aluminum," shown in Figure 4.

2.3.2 *Boundary conditions*

The bottom of the mast, where it is fixed to the deck of the ship, is a fixed boundary, that is, no translation or rotation is allowed.

For the concept with a cubic mast, each pair of sub-parts that contact each other are tied together at the contact surface, so there is no relative motion between them. The panels can have small relative tangential displacement in the vertical direction, because the panels do not need to bear the global bending.

2.4 *Finite element analysis*

Quasistatic FEA is used to predict and evaluate the structural response. The commercial ABAQUS software (Dassault Systemes Simulia, 2020) is used to perform the FEA simulations. The geometrical nonlinearities are taken into account in ABAQUS using the NLGEOM option, which considers large deformations and displacements but not large rotations.

A set of quadrilateral mesh is applied as shown in Figure 5. The typical element size is 0.2 m, selected based on mesh independence studies. Since the section profile of the wingsail has some arcs and circles, curvature control is applied to the mesh generator. The maximum deviation factor is set to be 0.1, so that the approximate number of elements per circle at the edges of the crescent-shaped profile is 8.

The gravity of the wingsail structure is ignored since it does not have a noticeable influence on the stress distribution. For example, in the all-aluminum case with a cubic mast, to fit the strength requirements, the panels need to be slightly thicker. This increases the total weight by around 3% and decreases the tip displacement by around 4%, which can be neglected.

3 RESULTS AND DISCUSSION

3.1 *Weight*

A series of FEA simulations were performed to determine the thickness. The thicknesses of the different parts have been adjusted several times to satisfy the strength requirement (i.e., the maximum stress must be less than the yield stress) and to minimize the weight. Table 3 shows the thickness of each part of the cubic mast concept after the thickness adjustments.

By comparing the two concepts, it can be found that by dividing the wingsail structure into a strong frame and light panels, the total weight can be reduced by approximately 11% (see Table 4). For the all-aluminum concept with a cubic mast, the weight can be significantly reduced, but this results in a much larger tip displacement. It can be summarized that the "steel frame and aluminum panels" design shows better rigidity, while the "all in aluminum" design is lighter.

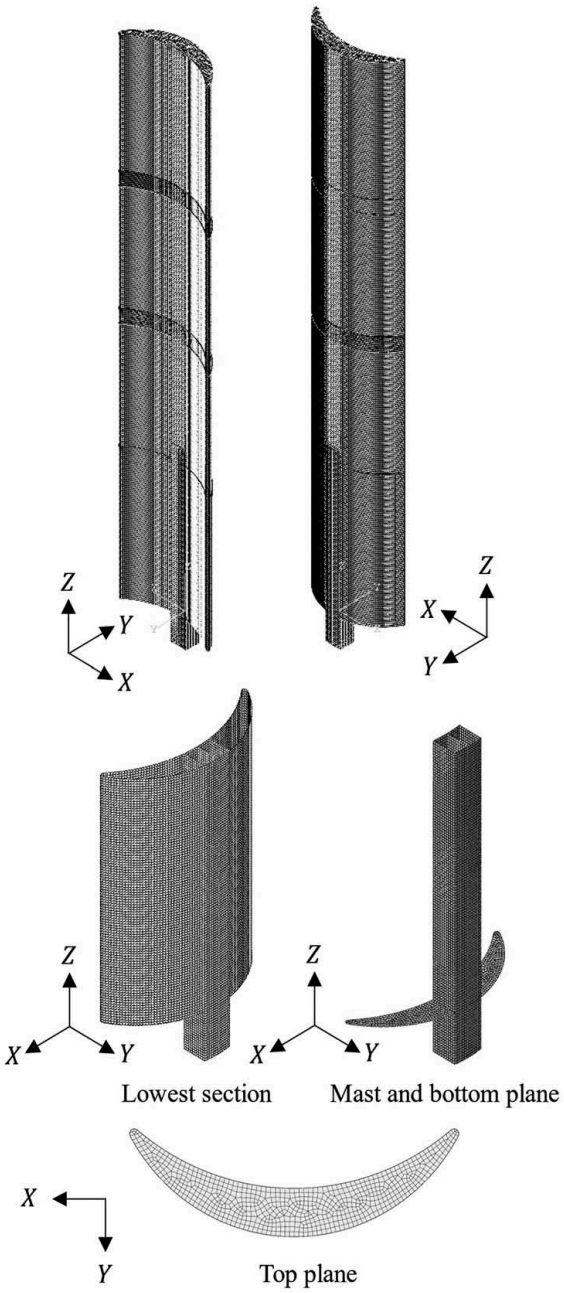

Figure 5. Numerical mesh of the concept with a cubic mast.

Table 3. Thickness after adjustment, for the concept with vertical stiffeners (unit: mm).

	Steel frame, aluminum panels	All in aluminum
Panels, section 1	10	10
Panels, section 2	7	7
Panels, section 3	5	5
Panels, section 4	5	5
Top	10	15
Bottom	20	20
Section plates	20	20
Edges, section 4	5	5
Edges, section 3	5	5
Edges, section 2	10	10
Edges, section 1	10	10
Center plates, section 4	5	5
Center plates, section 3	5	5
Center plates, section 2	10	10
Mast	20	30

3.2 *Strength*

In the concept with vertical stiffeners, at the section plate of section 2, approaching the edges, stress concentration can be obviously seen, although web structures have been added to avoid stress concentration at the bottom. However, for the remaining parts of the wingsail, the von Mises stress (σ_{Mises}) is much lower than the threshold value, as shown in Figure 6, so there is no need to continue adjusting the thickness.

In Figure 6 –

Figure 11, the counter plots follow the visualization rule that if the values for elements are within 75% of each other they will be averaged and then displayed.

Figure 7 shows the von Mises stress distributions for the two material arrangements. When the wingsail has a steel frame, as shown in Figure 7(a), the maximum von Mises stress occurs at the bottom of the mast. The stress distributed throughout the panels is much lower than in the frame, so the frame bears the global bending. On the other hand, for the "all in aluminum" concept, shown in Figure 7(b), the stress in the panels is comparatively larger, though the distribution of von Mises stress throughout the frame shows similar characteristics. The maximum von Mises stress

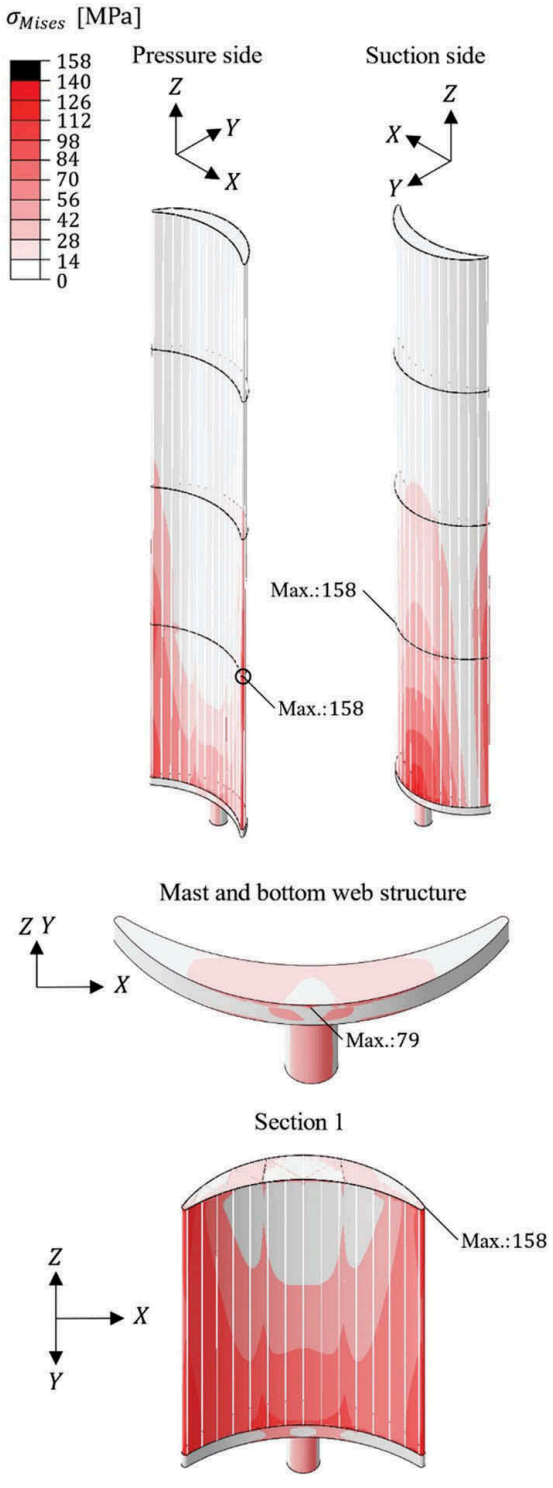

Figure 6. von Mises stress distribution for the concept with vertical stiffeners.

Table 4. Weight, maximum von Mises stress, and maximum deflection.

			Concept with a cubic mast	
		Concept with vertical stiffeners	Steel frame, aluminum panels	All in aluminum
Total weight	[t]	130	116	74
Weight, excluding the panels	[t]		75	33
Max. von Mises stress	[MPa]	158	141	103
Max. deflection	[m]	0.32	0.59	1.14

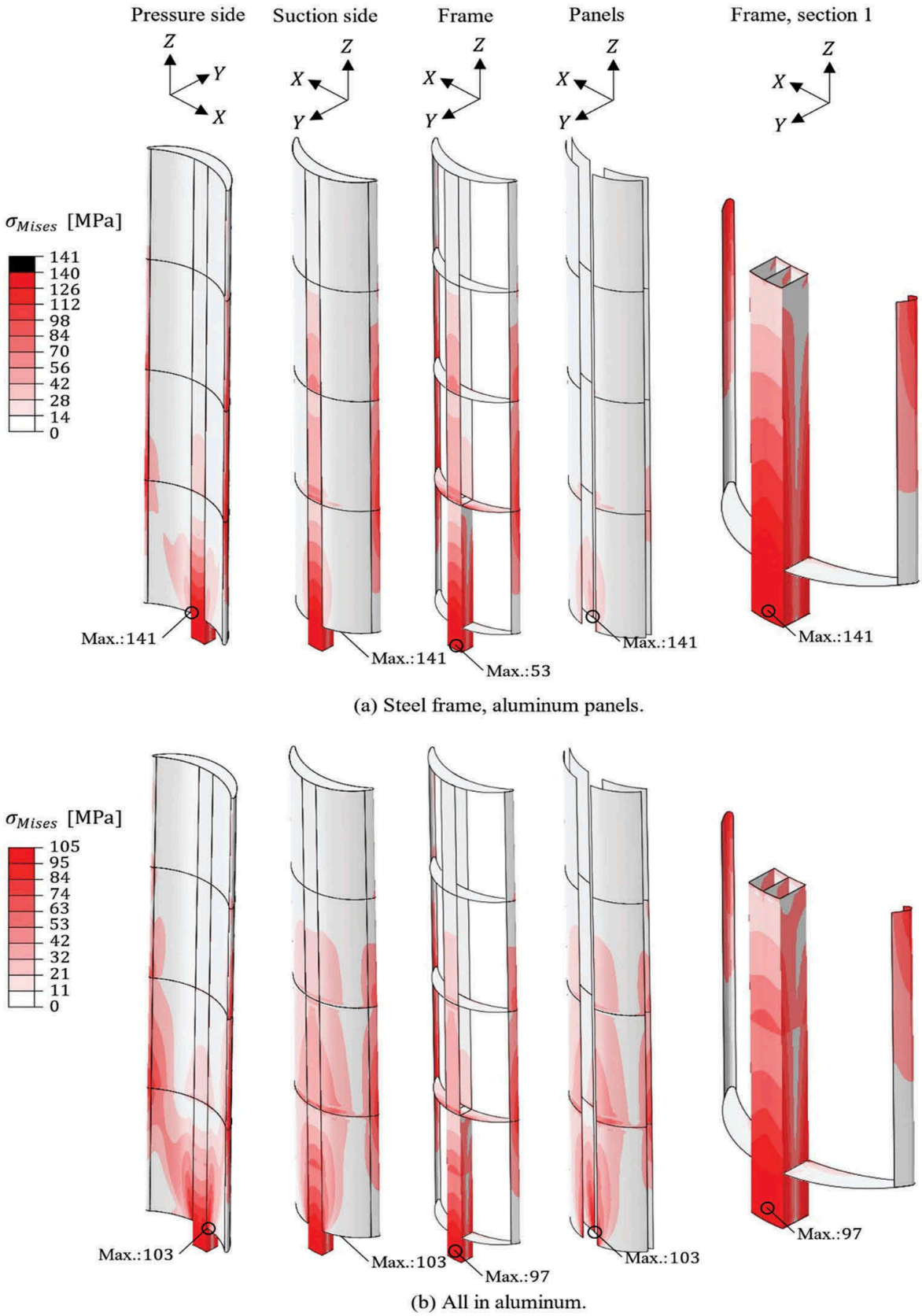

Figure 7. Von Mises stress distribution for the concept with a cubic mast.

is found at the contact area of the mast and the bottom. The stress concentration is reduced by introducing the cubic mast, but it still occurs. The maximum von Mises stress happens at the contact area of the mast and the bottom for both of the material arrangements.

The risk of normal buckling is assessed in this study by calculating the buckling stress of the mast according to Euler's formula for buckling and comparing it with the maximum compressive normal stress from the FEA results. Shear buckling is not

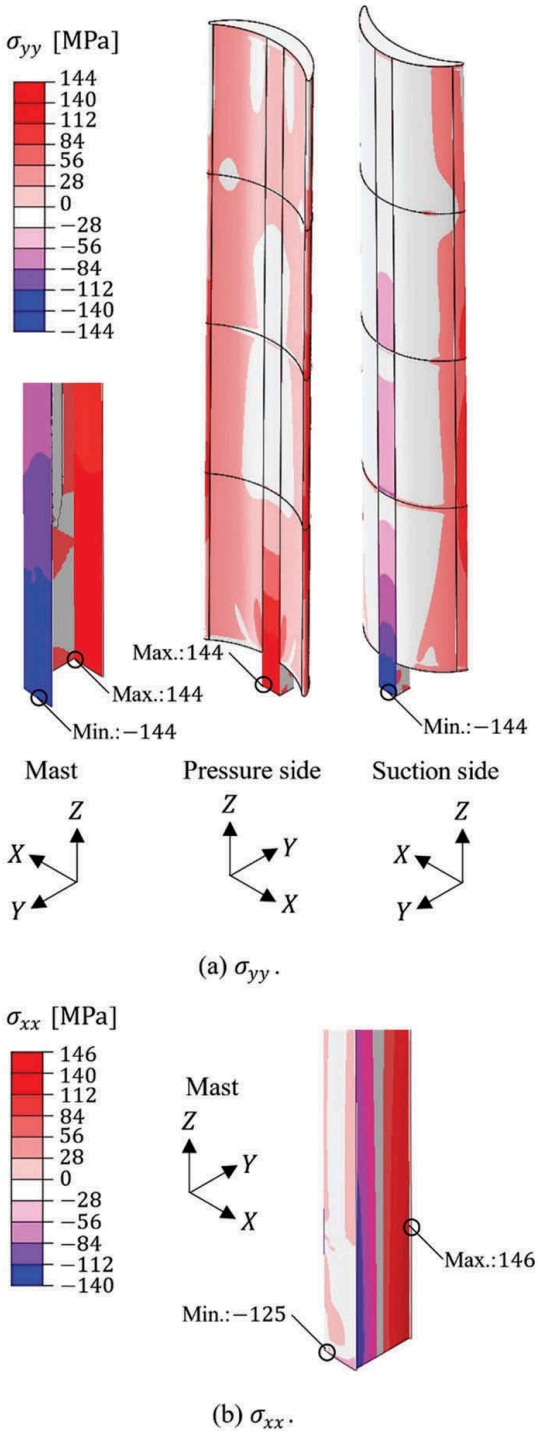

Figure 8. Normal stress distribution for the concept with a cubic mast, steel frame and aluminum panels.

studied since the shear stress throughout the wingsail structure is lower than the normal stress. Additionally, shear stress mainly occurs at the horizontal section plates, which are unaffected by the global bending and are much thicker and stronger than the other parts of the structure.

Figure 8 shows the normal stress distribution throughout the wingsail, especially the mast, for the concept with a steel frame. σ_{xx} is the normal stress in local x direction, and $\sigma_{yy}$is the normal stress in local y direction. Compressive normal stress mainly occurs in the mast and the central plates. As can be seen in Figure 8(a), σ_{yy} is mainly concentrated in the mast. The riskiest part, with the highest compressive normal stress, is the bottom of the mast on the suction side of the wingsail, which is the compressed side in the view of structural response.

In Figure 8(b), the distribution of σ_{xx} shows similar properties. For the all-aluminum arrangement, the normal stress distribution shows similar characteristics. The high compressive normal stress brings the risk of buckling at the mast. To reduce the compressive normal stress at the bottom of the mast, several solutions could be considered, for example, the lower part of the mast could be made thicker, or some stiffeners could be added inside the mast.

From the thickness values in Table 3, the moment of inertia can be calculated. Then, the buckling stress of the mast can be calculated using Euler's formula for buckling. The buckling stress values for the steel and aluminum masts are 252 MPa and 126 MPa, respectively, which are both higher than the allowable von Mises stress, so the mast does not buckle.

For the material arrangement with a steel frame, the shear stress (σ_{xy}) mainly occurs at the section plates of section 2, especially the area attached to the mast, as shown in Figure 9(a). However, for the all-aluminum arrangement, significant shear stress can also be found at the bottom, as shown in Figure 9(b). The magnitude of the maximum shear stress is approximately 20% of the maximum normal stress, so the normal stress is the main constraint on the strength.

3.3 *Rigidity*

The characteristics of the distribution of the deformation displacement in the Y direction (γ_y) are similar for the two material arrangements, as shown in Figure 10.

In the all-aluminum structure, the displacement is around twice as large as in the structure with a steel frame and aluminum panels. For the steel frame structure, the maximum displacement happens at the edges of the top plate, while for the all-aluminum structure, it is at the middle of the top plate. It can be inferred that the rigidity of the center plates is higher than that of the edges when applying a steel frame, but for the all-aluminum arrangement, the edges show higher rigidity. In addition, the deformation of section 1 is small due to the strong mast, especially for the steel frame arrangement. A possible solution to increase the rigidity of the higher sections would be to add a vertical plate expanding in the Y direction between the center plates for each section.

Figure 11 shows the distribution of the rotation in the chordwise direction (θ_x). It can be seen that the center plates of section 2 experience significant rotation at their bottom, which makes the displacement of the upper sections (i.e., sections 2, 3, and 4) increase. As in Figure 8, it is clear that compressive normal stress also happens there. Thus, the lower part of each center plate could be optimized to be thicker, or some extra stiffeners could be added for reinforcement.

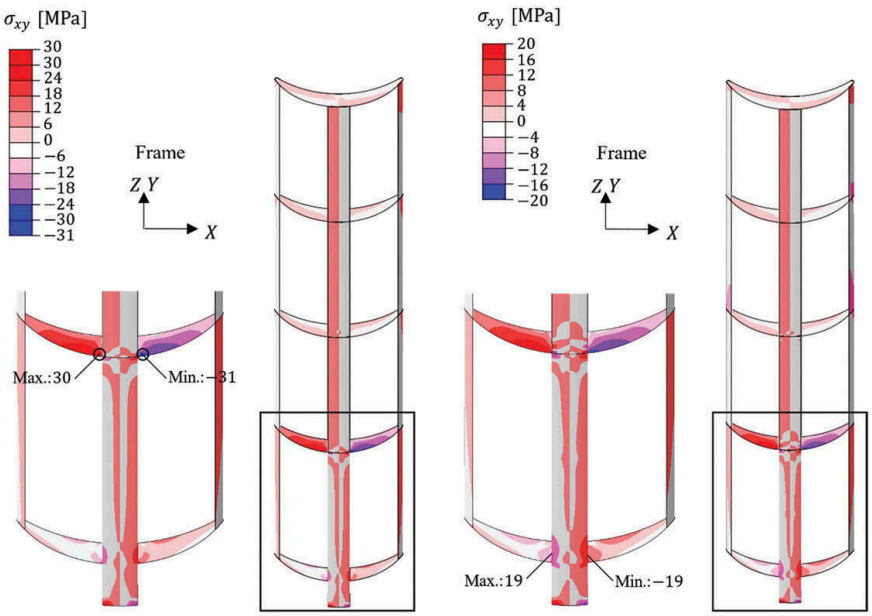

(a) Steel frame, aluminum panels. (b) All in aluminum.

Figure 9. Shear stress distribution for the concept with a cubic mast.

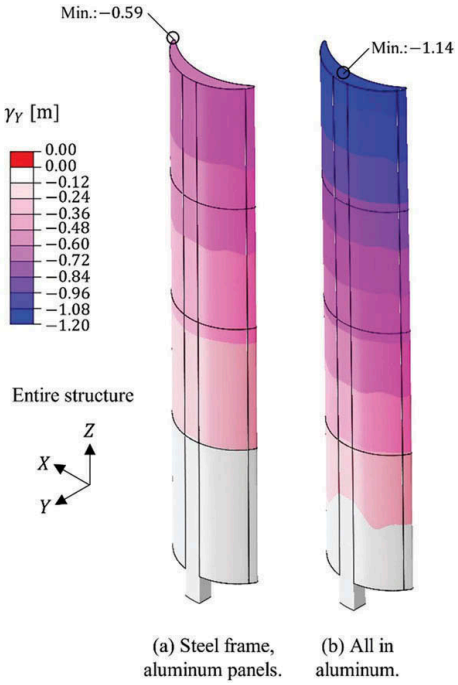

(a) Steel frame, aluminum panels. (b) All in aluminum.

Figure 10. Deflection magnitude distribution for the concept with a cubic mast.

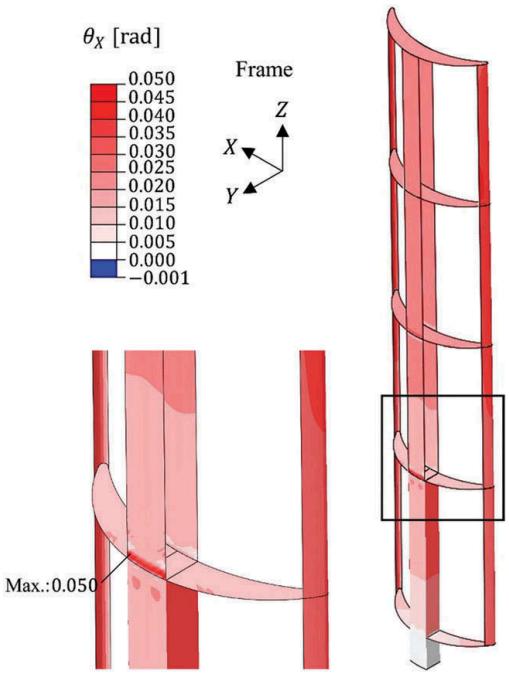

Figure 11. Distribution of rotation in the chordwise direction for the concept with a cubic mast, all-aluminum.

The initial design is that almost all the global bending is borne by the frame. To check that the panels do not bear the global bending, validation cases were carried out. In the validation cases, the panels are removed, and shell edge loads are directly applied on the frame instead of having pressure and suction loads on the panels. The magnitude of the shell edge loads is calculated according to the balance of the panels. For the FEA cases with and without panels, the total force and moment on the whole structure are kept the same. The results show nearly the same reaction force at the bottom of the mast, but the tip displacement doubled when removing the panels, so the frame is still not strong enough and the panels also contribute to the global strength. Further structural optimization could be carried out to make the frame stronger.

4 CONCLUSIONS

This study proposed and compared two different concept designs for the structure of a lightweight

telescopic wingsail with a crescent-shaped sectional profile. The concept that has a strong frame with a cubic mast and lightweight panels shows better performance in terms of weight, strength, and rigidity. The structural response of this concept was analyzed by applying quasistatic FEA.

Among the three assessment criteria that were considered, the strength, especially the von Mises yield and compressive normal stress, is the most critical criterion when evaluating the wingsail structure.

The cuboid mast, compared with the other concept, has the advantage that it can avoid stress concentration in the lower sections, especially the contact part between the mast and the bottom plate. Having the mast extending through the whole of section 1 also releases stress concentration on the horizontal plate of section 2. Using the frame to bear the global bending and torsion is a promising approach. Compared with the previous concept with vertical stiffeners, the "frame and panels" concept can achieve the required strength with a significantly lower weight. By replacing steel with aluminum, the weight of the frame can be reduced by around 50%; however, the flexibility, measured by the tip displacement, is increased.

Further work could focus on the dynamic structural response, for example, vortex-induced vibration and fatigue, which may lead to increased strength requirements (Storhaug et al., 2022). The results of the structure analysis could be used in future work as a basis for structural optimization and FSI analysis.

ACKNOWLEDGEMENTS

This work was performed within the project WindStruc (wind-assisted propulsion for commercial vessels) funded by the Swedish Energy Agency through contract agreement no. 51552-1, co-funded by ScandiNAOS AB, and Stena Rederi AB. The computations and data handling were enabled by resources provided by the Swedish National Infrastructure for Computing (SNIC), partially funded by the Swedish Research Council through grant agreement no. 2018-05973.

REFERENCES

ASTM. 2004. Standards specification for aluminum and aluminum-alloy sheet and plate. American Society for Testing and Materials.

BS EN. 2004. 10025-2: 2004: Hot rolled products of structural steels. Part 2-Technical delivery conditions for non-alloy structural steels. *British Standards Institution, London*.

Dassault Systemes. 2020. Abaqus 2020. *Abaqus Analysis User's Guide*.

Hu, Y., He, J., Tang, J., Xue, S., Liu, S., & Wu, Y. 2015. Sail Structure Design and Stability Calculation for Sail-assisted Ships. In *Marine Engineering Frontiers*, 3:1. World Scientific.

IMO. 2018. Interpretation of Initial IMO Strategy on Reduction of GHG Emissions from Ships. http://www.imo.org.

Lu, R., & Ringsberg, J.W. 2020. Ship energy performance study of three wind-assisted ship propulsion technologies including a parametric study of the Flettner rotor technology. *Ships and Offshore Structures* 15, no. 3 (March 15): 249–258. https://www.tandfonline.com/doi/abs/10.1080/17445302.2019.1612544.

Nikmanesh, M. 2020. Sailing performance analysis using CFD simulations: A study on crescent shaped wing profiles. Chalmers University of Technology. https://odr.chalmers.se/handle/20.500.12380/304303.

Ouchi, K., Uzawa, K., & Kanai, A. 2011. Huge Hard Wing Sails for the Propulsor of Next Generation Sailing Vessel. In *Second International Symposium on Marine Propulsors*, 1–5.

Ouchi, K., Uzawa, K., Kanai, A., & Katori, M. 2013. Wind challenger" the next generation hybrid sailing vessel. In *The Third International Symposium on Marine Propulsors, Launceston, Tasmania*, *Australia*, 562–567. Launceston, Tasmania, Australia.

Shukla, P.C., & Ghosh, K. 2009. Revival of the modern wing sails for the propulsion of commercial ships. *International Journal of Physical and Mathematical Sciences* 3, no. 3: 207–212.

Storhaug, G., Borzacchiello, G.R., & Hoffmeister, H. 2022. Fatigue assessment of wind assisted propulsion systems. In *Proceedings of the ASME 2022 41st Internal Conference on Ocean, Offshore and Arctic Engineering*.

Zhu, H., Nikmanesh, M.B., Yao, H.D., Ramne, B., & Ringsberg, J.W. 2022. Propulsive Performance of a Novel Crescent-Shaped Wind Sail Analyzed With Unsteady Rans. In *Proceedings of the International Conference on Offshore Mechanics and Arctic Engineering - OMAE*. Vol. 7. Hamburg, German.

Zhu, H., Yao, H.-D., & Ringsberg, J.W. 2022. Unsteady RANS and IDDES study on a telescopic crescent-shaped windsail. In *International Conference on Ships and Offshore Structures, ICSOS 2022*. Ålesund, Norway.

Taylor & Francis
Taylor & Francis Group
http://taylorandfrancis.com